UNIVERSITY OF OULU

MASTER'S THESIS

Measurements of physical parameters of accreting white dwarfs and characterization of accretion discs around them using optical spectroscopy

Author:
Jussi HEDEMÄKI

Supervisor:
Dr. Vitaly NEUSTROEV

A thesis submitted in fulfillment of the requirements for the degree of Master of Science

in

Astronomy

July 14, 2021

Declaration of Authorship

I, Jussi HEDEMÄKI, declare that this thesis titled, "Measurements of physical parameters of accreting white dwarfs and characterization of accretion discs around them using optical spectroscopy" and the work presented in it are my own. I confirm that:

- This work was done wholly or mainly while in candidature for a research degree at this University.
- Where any part of this thesis has previously been submitted for a degree or any other qualification at this University or any other institution, this has been clearly stated.
- Where I have consulted the published work of others, this is always clearly attributed.
- Where I have quoted from the work of others, the source is always given. With the exception of such quotations, this thesis is entirely my own work.
- I have acknowledged all main sources of help.
- Where the thesis is based on work done by myself jointly with others, I have made clear exactly what was done by others and what I have contributed myself.

Signed:

Date:

"For my part I know nothing with any certainty, but the sight of the stars makes me dream."

Vincent Van Gogh

UNIVERSITY OF OULU

Abstract

Faculty of Science
Space Physics and Astronomy

Master of Science

Measurements of physical parameters of accreting white dwarfs and characterization of accretion discs around them using optical spectroscopy

by Jussi HEDEMÄKI

Cataclysmic variables (CV) are compact binaries, where a white dwarf (WD) accretes mass from a low-mass companion. For a non-magnetic (or weakly magnetic) WD this accretion of mass creates an accretion disc around it. UV spectroscopy of CV systems allows the easiest way to measure the spectrum of a WD, thus it is widely used. The downside of UV spectroscopy is the limited sample of objects. Using optical spectroscopy, a greater amount of CVs can be studied.

To this end, we set out to study CVs by modelling observed optical spectra, in order to assess two stellar parameters: effective temperature $T_{\rm eff}$ and surface gravity $\log g$ of the WD. We first show that we were able with sufficient accuracy to model single WD spectra. We then show that we were able to recover the parameters of modified theoretical single WD spectra, where the modification can be e.g. the addition of noise or the cutting of absorption linecores. We also show that rotational broadening and zeeman-splitting had a negligible effect on our modelling procedure.

Lastly, we show the modelling results of 11 CVs in total, for which the stellar parameters are obtained and accretion disc spectra are extracted. For four objects we compare our obtained parameter values to those obtained by UV spectroscopy. Finally, the contribution of the accretion disc luminosity to the total luminosity of the system is shown.

Acknowledgements

I want to express my deepest gratitude to the University of Oulu, where I have spent my recent years to study physics under the guidance of Faculty of Science. There I have had the pleasure to meet great and knowledgeable people. I especially want to thank the Space Physics and Astronomy unit, where I have spent my recent couple of years to learn and grow as an individual.

I humbly thank my thesis supervisor, Dr. Vitaly Neustroev, for his guidance with my thesis and other studies. Many hours have been spent in discussion regarding all things physics, from which I would like to think I have learned something.

I also want to acknowledge Pekka, Veera, all my other friends and fellow students, with which I have had the pleasure to enjoy life as a student of physics. This would not have been the same without you all.

Last but not least, my deepest thanks go to my sister Jaanamaria and my partner Selina, who have given me their enduring support during the writing of this thesis. I would not be here without you.

Contents

List of Figures

List of Tables

List of Abbreviations

CV	**C**ataclysmic **V**ariable
WD	**W**hite **D**warf
DN	**D**warf **N**ovae
AML	**A**ngular **M**omentum **L**oss
GR	**G**ravitational (wave) **R**adiation
MB	**M**agnetic **B**raking
LTE	**L**ocal **T**hermodynamic **E**quilibrium

Dedicated to all those who ponder the wonders of the universe, seeking answers to questions they have not yet asked

Chapter 1

Introduction

1.1 The purpose of our study of cataclysmic variables

The subject of my thesis is centered on cataclysmic variables (CVs), which are close interacting binary systems. These systems comprise of a donor star and a mass accreting star. The donor star is a low-mass star and it can be in different evolutionary stages, but the mass accreting star is a white dwarf (WD). If the stars orbit close enough to each other, there will be mass transfer between the stars. When the more compact WD accretes mass, a disc of material will form around it. The accretion disc can be seen in the spectrum of a CV.

In this study we are interested to see if we can model accurately optical spectra of CVs, and obtain stellar parameters $T_{\rm eff}$ and $\log g$ with values that are similar to values obtained from modelling UV spectra. If we are successful, we can use the obtained parameters to extract the accretion disc spectrum. This would allow us to analyze e.g. the luminosity of the accretion disc.

1.2 Background

There is a great amount of literature on binary systems in general, accretion discs, cataclysmic variables and the phenomena involved, for example the books by Prialnik [1], Frank et al. [2], Warner [3] and Pringle and Wade [4]. Refer to these for more in-depth look, as I will only briefly touch upon them in the following sections.

1.2.1 Stars in an interacting binary system

As the name implies, a binary system has two stars that orbit around a common center of mass. The distance between the stars determines the intensity of their interaction, and for the stars to have have mass transfer between them, the distance must be just few times the radius of the donor star. The orbit of the stars can be approximated to be a circle; binary systems with circle orbits allow the easiest determination of stellar masses for both stars.

The two stars affect each other mainly in two ways:

- Irradiation by the other companion
- Gravitational distortion

The incoming radiation is absorbed on the surface, by a zone called *skin depth*. It can be shown, that in the end a negligible amount of mass is affected by the irradiation, and thus the effect of it in regards of the whole star is small. The effect of gravitational distortion is described by the *tidal force*. In essence, one looks at the difference of the force the companion star exerts onto the other stars surface, and to its core. In equation form it is written as

$$f_{\text{tide}}(r) = \frac{GM_2}{(d-r)^2} - \frac{GM_2}{d^2} \approx \frac{2GM_2 r}{d^3}.$$

Here d is the distance between the stars as point masses, r is the distance from the affected stars core to a mass element on its surface, G is the gravitational constant and M_2 the mass of the companion star.

Both of these mechanisms have relatively small effect on the stars, if they are not close enough for mass transfer. In order for mass transfer between the stars to be possible, their *equipotential surfaces* must merge into one. Before talking more of this phenomenon, it is useful to see what determines the accretion of material from one star to the other. Looking at a single star of mass M and radius R, surrounded by material (i.e. gas), we can assume that the star will accrete material from its surroundings. In a simple case this accretion is spherically symmetric. As the star accretes material, it releases gravitational energy. If this accretion happens over a time interval δt, the average rate of gravitational energy release is proportional to the average accretion rate

$$\dot{E}_{\text{grav}} = \frac{\delta E_{\text{grav}}}{\delta t} = \frac{GM\delta m}{\delta t R} = \frac{GM\dot{M}}{R},$$

where δm depicts an accreted mass element. To satisfy thermal equilibrium, this obtained energy must be radiated away in the form of *accretion luminosity*:

$$L_{\text{acc}} = \dot{E}_{\text{grav}}.$$

If we take a star like the Sun, and assume that it doubles its mass by accretion in 10^{10} years, its average rate would be $\dot{M} = 10^{-10} M_\odot \text{yr}^{-1}$. Thus the accretion luminosity of the Sun would be $L_{\text{acc}} = GM_\odot \dot{M}/R_\odot \approx 3 \cdot 10^{-3} L_\odot$. Here $M_\odot$, $R_\odot$ and $L_\odot$ are the mass, radius and luminosity of the Sun, respectively. As such, luminosity from accretion would be insignificant compared to the star's own luminosity. Inputting to the equation the values of a WD would result in a luminosity value of about 100 times higher, which is considerably higher than the usual luminosity of WDs.

There is an upper limit for the accretion rate and resulting accretion luminosity, called Eddington critical luminosity. Past a certain point, the radiation of the star will push back any material that is accreted. The Eddington luminosity is

$$L_{\text{Edd}} = \frac{4\pi c G M}{\kappa} = 3.2 \cdot 10^4 \left(\frac{M}{M_\odot}\right) \left(\frac{\kappa_{es}}{\kappa}\right) L_\odot.$$

Thus, $\dot{M} < 4\pi cR/\kappa$, and if $\kappa = \kappa_{es}$, then $\dot{M} < 10^{-3} R/R_{\odot} M_{\odot} \mathrm{yr}^{-1}$. Here κ describes opacity, and κ_{es} is the electron-scattering opacity. It can be seen that the accretion rate limit depends only on the radius of the star. Furthermore, it can be seen that compact stars such as WDs are able to obtain notable accretion luminosities even if the mass accretion rate is far from the upper limit.

The material is accreted onto the surface of the star, which as a result will have a temperature T_{b}(b meaning boundary). If we approximate the star as a blackbody, we can use Stefan-Boltzmann law to estimate the temperature to be

$$T_{\mathrm{b}} = \left(\frac{L_{\mathrm{acc}}}{4\pi R^2 \sigma} \right)^{1/4} = \left(\frac{GM\dot{M}}{4\pi R^3 \sigma} \right)^{1/4}.$$

Here σ is the Stefan-Boltzmann cosntant. Using the above result for $\dot{M}$, for a WD we obtain a surface temperature of $T_{\mathrm{b}} = 10^6\,\mathrm{K}$. A WD with this kind of surface temperature would radiate in the X-ray region. So it would seem that dead stars like WDs, which alone are not bright, can achieve high luminosities as a result of accretion of material from companion stars.

1.2.2 Mechanism of mass transfer

Isolated stars have a spherically symmetric gravitational field around them, created by their mass. This field can be thought of as equipotential surfaces, centered on the star. Equipotential surface simply means that on that surface the potential, in this case the gravitational potential, is the same on all points. If a test particle moves on this surface, it can do so without gaining or losing energy. Moving through different potential surfaces does affect the energy of the particle. In a binary system the equipotential surfaces of the stars have different geometrical shapes. If the distance between the stars is large, both have their own, approximately spherical equipotential surfaces. Very close to each other, the stars share one equipotential surface. The interesting case is in the between, when the transition from two surfaces to one occurs.

Assuming two stars of mass M_1 and M_2, where $M_1 \geq M_2$, the stars orbit around their common center of mass with angular velocity ω, which is

$$\omega^2 = G(M_1 + M_2)/a^3. \tag{1.1}$$

Here a is now the constant distance between the stars. The above is actually an expression of Kepler's third law ($P \propto a^3$), as $\omega = 2\pi/P$, where P is the period of rotation. The gravitational potential can be written in equation form as

$$\begin{aligned} \Phi = &- \frac{GM_1}{(x^2+y^2+z^2)^{1/2}} - \frac{GM_2}{[(x-a)^2+y^2+z^2]^{1/2}} \\ &- \frac{1}{2}\omega^2 \left[\left(x - \frac{M_2 a}{M - 1 + M_2} \right)^2 + y^2 \right]. \end{aligned} \tag{1.2}$$

The above equation is written in Cartesian coordinate system, which is comoving with the stars. (0, 0, 0) is at the location of star 1, the masses of star 1 and star 2 are at (0, 0, 0) and (a, 0, 0), respectively, and the center of mass

for the system is at the point $(x_{\mathrm{CM}}, 0, 0)$, where $x_{\mathrm{CM}} = M_2 a/(M_1 + M_2)$. The equation is made up of three different terms: first two are the gravitational potentials of the stars, approximated as point masses, and the third term describes the rotational potential which is a result of the centrifugal force in the rotating system. The equation can also be written in normalized form:

$$\Phi' = \frac{2}{(1+q)(x^2+y^2+z^2)^{1/2}} + \frac{2q}{(1+q)[(x-1)^2y^2+z^2]^{1/2}} \left[\left(x - \frac{q}{1+q}\right)^2 + y^2\right], \tag{1.3}$$

where now

$$\Phi' = \left[-\frac{G(M_1+M_2)}{2a}\right]^{-1} \Phi$$

is the normalizing coefficient. In the normalized potential, $q \equiv M_2/M_1$ is the mass ratio, and the distances are measured in units of a. Thus, normalizing the potential equation leads to an equation that is only dependant of one parameter, the mass ratio q. As stated earlier, equipotential surfaces are constant with respect to the gravitational potential, so $\Phi = C$. These potentials are described as *Roche equipotentials*, after Edouard Albert Roche, who in the 1900's was the first to study this problem.

If the constant C is large, the equipotential surfaces are closed and separate. Decreasing the value of C begins to distort the surfaces towards the center of mass, and reaching a critical value of C, the individual surfaces will touch. This leads to the *Roche limit* surface, and the contact point of the surfaces is known as *inner Lagrangian point* L_1. The two volumes inside the surfaces are called *Roche lobes*. The lobes act as a limit for the mass within, as the lobes determine the region where each stars gravitational potential is stronger. In other words, if the star fits inside its lobe, the material is not attracted by the companion star. Having a mass ratio of $q = 1$, the lobes are identical. With decreasing values of q, the lobe around star 1, the more massive in mass, expands, while the lobe around the less massive star shrinks. Decreasing further the value of q, the lobes transform into one continuous surface.

Even though the formulation of the equipotential surfaces was done with point masses, it can be approximated to be useful with real cases, where the stars occupy the volume within the lobes. One can define a *Roche radius* r_L, which describes a radius of a sphere that has a volume equal to a respective Roche lobe. Peter Eggleton [5] has provided an equation for Roche radius:

$$\frac{r_L}{a} = \frac{0.49q^{2/3}}{0.6q^{2/3} + \ln\left(1+q^{1/3}\right)}, \tag{1.4}$$

which describes the Roche radius for M_2. For M_1, q must be replaced with q^{-1}. A less accurate approximation is

$$\frac{r_L}{a} \approx 0.5 \left(\frac{q}{1+q} \right)^{1/3}, \tag{1.5}$$

which gives the ratio of Roche lobe radii as $r_{L,2}/r_{L,1} \approx q^{1/3}$.

What type of configuration of Roche lobes leads to mass transfer from one star to the other? An answer was proposed by Zdenek Kopal, namely a *Semidetached binary*. In this case, the radius of one star exceeds the boundary of its Roche lobe, initiating mass transfer to the companion star.

1.2.3 Conservative mass transfer

In the case of conservative mass transfer, we assume that the mass and the angular velocity of the system are conserved. Assuming also circular orbits for the stars in the binary system, the total angular momentum will be

$$J = M_1 a_1^2 \omega + M_2 a_2^2 \omega + I_1 \omega_1 + I_2 \omega_2. \tag{1.6}$$

The terms involving mass describe the orbital motion, and the latter two terms describe the stellar spin. These last two terms are only small corrections to the resulting total angular momentum, as the moments of inertia $I_{1,2}$ for stars are small, and as such they can be neglected. Stars rotating in circular orbits around a common center of mass exert an equal but opposite force to each other, which allows us to write

$$a_1 = a \frac{M_2}{M_1 + M_2} \qquad \text{and} \qquad a_2 = a \frac{M_1}{M_1 + M_2},$$

so we obtain

$$J = \frac{M_1 M_2}{M_1 + M_2} a^2 \omega.$$

Substituting earlier description for angular velocity, Eq.(1.1) to the above equation, we obtain

$$J = \left(\frac{G}{M_1 + M_2} \right)^{1/2} M_1 M_2 a^{1/2}.$$

Now we can use the assumption of a conservative system:

$$\frac{d}{dt}(M_1 + M_2) = 0 \qquad \longrightarrow \qquad \dot{M}_1 = -\dot{M}_2, \tag{1.7}$$

which simply means that mass gained by one star is lost by the other. The other assumption made gives

$$\frac{dJ}{dt} = 0 \qquad \longrightarrow \qquad \frac{\dot{M}_1}{M_1} + \frac{\dot{M}_2}{M_2} + \frac{1}{2}\frac{\dot{a}}{a} = 0. \tag{1.8}$$

Combining the equations (1.7) and (1.8) we get

$$\frac{\dot{a}}{a} = \frac{2\dot{M}_1(M_1 - M_2)}{M_1 M_2}. \tag{1.9}$$

This last equation tells us that as mass is lost by one star, and thus gained by the other, the separation (and through Kepler's third law, the period) changes as well. The direction of the change of separation is determined by the star that loses mass; if $\dot{M}_1 < 0$, then $\dot{a} < 0$, and the stars get closer to each other. This strengthens the mass-transfer rate, thus decreasing the separation further. Eventually, the system may approach a runaway scenario. This kind of process also answers the *Algol paradox*. An Algol binary is a system where a low-mass giant orbits with a more massive main-sequence star. This shouldn't be possible, as the more massive a star is, the faster it leaves the main sequence and enters the giant phase. Due to mass transfer from the more massive star to the less massive, we may find binary systems where enough mass has been lost by the giant to the main sequence star.

In the case of $\dot{M}_1 > 0 \longrightarrow \dot{a} > 0$, meaning the less massive star fills its Roche lobe and thus loses mass to the companion star, increasing the distance between the stars. This means that the mass ratio $q = M_2/M_1$ decreases, which results in decreasing Roche lobe radii. Due to this, the mass losing star may continue to fill its Roche lobe, forming a continous state of mass transfer. Systems where the more massive and compact (compact as it does not fill its Roche lobe) star is a WD, and it accretes material from the less massive companion star, are called *cataclysmic variables*.

Mass accumulated by a star in a binary system is not straightforward. The mass particles have different angular momentum, and this needs to be accounted for. Indeed, mass transfer leads to an accretion disc, where the particles orbit around the star at differing radii.

1.2.4 Accretion discs

As noted in the last section, steady mass transfer between a WD and another star in a binary system leads to cataclysmic variables. We can assume that the WD is accompanied by a main-sequence star. It is customary to define the mass-accreting star as the *primary*, and mass-losing star as *secondary*, and we will be using these definitions going forward. As also stated earlier, the point of interest in a system where the individual Roche lobes have merged into one, is the inner Lagrangian point L_1. At this point the forces exerted by both stars are equal, so a test particle there would stay there. Thus, as the system rotates around the common center of mass, the test particle must be provided the centripetal force necessary to rotate by the two stars. As the more massive star M_1 exerts more force to the particle than M_2, the L_1 must be further away from the latter than from the center of mass. The location of x_{CM} is at

$$x_{\mathrm{CM}} = \frac{M_2 a}{M_1 + M_2} \qquad \longrightarrow \qquad \frac{X_{\mathrm{CM}}}{a} = \frac{q}{1+q}. \tag{1.10}$$

If a test particle were to be at x_{CM}, it would be affected more by the primary star than the secondary star, so for the particle to be in equilibrium in L_1, it must be that $x_{L_1} > x_{\mathrm{CM}}$ (origin is at M_1). In this co-moving coordinate frame, on the line of centres between the stars $y = z = 0$, and we can find x_{L_1} from the equation

$$\frac{GM_1}{x^2} - \frac{GM_2}{(a-x)^2} = \omega^2(x - x_{\mathrm{CM}}), \tag{1.11}$$

which is obtained by taking the derivative of Equation (1.2) with respect to x: $d\Phi(x,0,0)/dx = 0$. Normalizing Equation (1.11) in the same way as Equation (1.3), we obtain

$$(1+q)x^5 - (2+3q)x^4 + (1+3q)x^3 - x^2 + 2x - 1 = 0. \tag{1.12}$$

Using units of a for distance makes the equation dimensionless. If the masses of the stars are equal, so that $q = 1$, it leads to one real root for Equation (1.12), $x_{L_1} = \frac{1}{2} = x_{\mathrm{CM}}$. Thus, only if the masses are equal, is the equilibrium point at the center of mass. Decreasing $q = \frac{M_2}{M_1}$, or increasing the mass of the primary, $x_{\mathrm{CM}} \to 0$, so the center of mass gets closer to the primary, which is expected. At the same time, $x_{L_1} \to 1$, so the Lagrangian point gets closer to the secondary. This is also expected, as the forces must be equal at L_1.

The L_1 can be thought as the maximum of the potential Φ, where the test particle sits at the top. Any small perturbation to either direction on the x-axis leads the particle to fall into the potential well of one star or the other. Evaluating the Equation (1.12) further gives two other maxima for the potential: for values $0 < q < 1$, an L_2 exists on the far side of M_2, and L_3 on the far side of M_1. A test particle on either of these points may fall into the binary system, or escape outwards. It is good to remember that here the calculations are done for a simplified one-dimensional case. The real three-dimensional case is greatly more complex, but one gets the idea.

So far we've gathered that a particle in the Lagrangian point L_1 is in equilibrium. Let us assume that it gains some velocity towards M_1. The velocity obtained by the particle can be of the order of the thermal velocity in the atmosphere of the secondary star. Compared to the rotational velocity it is small, but still enough to perturb the particle from equilibrium. As the particle has angular momentum, due to the rotation around the center of mass, it cannot fall directly onto the primary star. Eventually, the particle will begin to orbit the primary star in a Keplerian orbit. As more and more particles are perturbed from L_1 with this small velocity, their individual trajectories will be similar. The particles will eventually form a disc around M_1, as they lose angular momentum due to friction between other particles. This accumulation of particles into a disc happens on the equator, where the gravitational field spreads them evenly. We can estimate the radial extension of this disc with following assumptions:

- Inside the primary's Roche lobe the secondary star has no effect
- The angular momentum is conserved

The second point means in essence that the angular momentum of a particle at L_1 is equal to that of the Keplerian orbit around M_1, when both are taken with respect to an axis passing through the center of M_1 perpendicularly to the orbital plane in a stationary frame of reference. The specific angular momentum at L_1 with respect to M_1 is

$$j_1 = x_{L_1}^2 \omega = x_{L_1}^2 \left[\frac{G(M_1 + M_2}{a^3} \right]^{1/2}. \tag{1.13}$$

Assuming also that $x_{L_1} \approx a - r_{L,2}$ and using (1.5) for $r_{L,2}$, we obtain

$$j_1 = \sqrt{GM_1 a}(1+q)^{1/2} \left[1 - 0.5 \left(\frac{q}{1+q} \right)^{1/3} \right]^2. \tag{1.14}$$

If now a particle orbits around the primary on a circular orbit at a distance r_d, it will have a velocity of $\sqrt{GM_1/r_d}$, and thus angular momentum $j_2 = \sqrt{GM_1 r_d}$. Now we can use the equality $j_1 = j_2$ to obtain

$$\frac{r_d}{a} = (1+q) \left[1 - 0.5 \left(\frac{q}{1+q} \right)^{1/3} \right]^4. \tag{1.15}$$

Using now relation (1.5) for $r_{L,1}$, the above equation can be expressed as

$$\frac{r_d}{r_{L,1}} = 2[(1+q)^{1/3} - 0.5q^{1/3}]^4, \tag{1.16}$$

which varies for values $q = 0.1$ and $q = 0.9$ as 0.8 and 0.65, respectively. Thus, using these assumptions, we see that the disc's radius employs a large part of the primary's Roche radius, and that it is only loosely dependent on the mass ratio of stars. Due to the large surface area of the disc, it can have a large luminosity compared to the stars.

As the disc forms, particles continue streaming towards the primary star. These particles, with high enough velocity, impinge upon the rim of the disc. This spot is called *hot spot*, and it can radiate huge amounts of energy, as the particles settle on the disc. The amount of energy radiated can equal or even surpass the combined radiation of both stars and the accretion disc. That said, in our case the hot spot should not be a dominating factor, as we show below that the mass transfer rate is relatively low.

1.2.5 Cataclysmic variables

In the systems called cataclysmic variables, the primary star is a WD which accretes material from a companion star, e.g a main-sequence star. The name of this systems arises from the violent eruptions of material that occur during and due to accretion. CV stars can be classified in several ways, and it depends on e.g. if the star has been observed to erupt more than once or not,

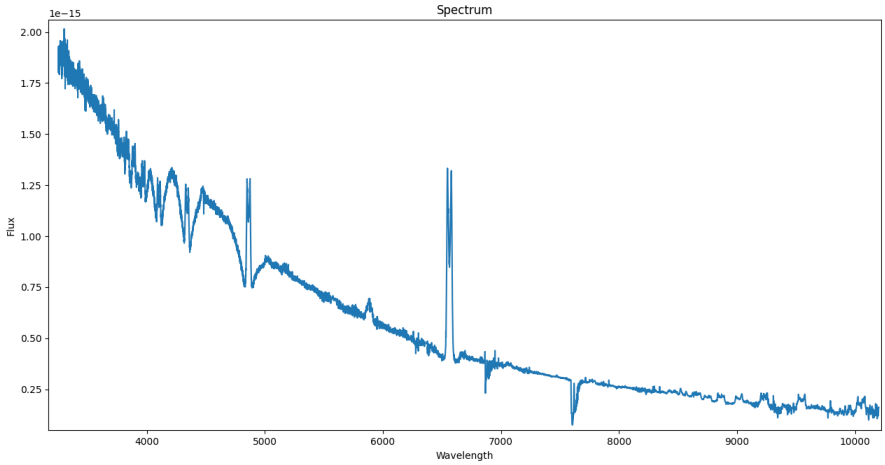

FIGURE 1.1: The spectrum of BW Scl, a cataclysmic variable star.

or if the outburst is due to thermonuclear runaway or the release of gravitational energy.

Objects of our interest are classified as *Dward novae* (DN). In DN, the outbursts are due to a temporal high increase in the accretion rate, which in turn increases the amount of energy that is gravitationally released. The outbursts have durations ranging from days to tens of days. The increase of brightness can be a few magnitudes, but certain types of DN, for example WZ Sge, can have up to 8 mag increase. The objects of interest for us are WZ Sge like objects. These outbursts are of recurring nature, and the time between outbursts can range from tens of days to tens of years. We are using spectra that are obtained between outbursts, when the system is in quiescence. The spectrum, as can be seen in figure 1.1, shows strong Balmer emission lines from the accretion disc. In optical wavelengths, absorption lines due to the WD can be seen around the emission lines. In the ultraviolet part of the spectrum the WD dominates, and the Balmer jump due to the disc is seen as well. The contribution of the secondary star can be seen in infrared, but the strength of the contribution depends on the type of the star. A main-sequence star will have a larger contribution to the whole spectrum of the system when compared to e.g. a brown dwarf.

Evolution of CV's and resulting phenomena

For a stable accretion in a CV system, a mechanism for angular momentum loss (AML) for the whole system must be in place. As angular momentum decreases, the distance between stars and the orbital period $P_{\rm orb}$ of the system decrease. Thus the mass-losing secondary, while shrinking in size, is still able to fill its Roche lobe. The AML mechanism is related to $P_{\rm orb}$. If $P_{\rm orb} \lesssim 3\,\mathrm{h}$, angular momentum is lost due to gravitational wave radiation(GR) (Patterson [6]), and for longer periods the magnetic braking(MB) due to stellar wind from the secondary acts as the dominating mechanism (Spruit and Ritter [7]).

Between $2\,\mathrm{h} \lesssim P_{\mathrm{orb}} \lesssim 3\,\mathrm{h}$, there is an observable gap in the amount of systems. In this period gap, the secondary plays a role in changing the AML mechanism (Knigge [8] and Knigge et al. [9]). The strength of MB is reduced, and the AML is driven by GR. Without GR the system would stay as a detached binary and the accretion of material would stop, as the secondary star no longer fills its Roche lobe. Because of this, systems with this period are hard to detect, hence the gap. Due to GR, the orbital separation is reduced until the secondary once again fills its Roche lobe, at which point $P_{\mathrm{orb}} \simeq 2\,\mathrm{h}$. Contraction of the secondary stops at $P_{\mathrm{orb}} \simeq 80\,\mathrm{min}$, and the system stops shrinking. This leads to increasing P_{orb} for the system, due to which they are called Period-bouncers.

The mean mass-transfer rate is linked to the effective temperature of a WD (Sion [10] and Townsley and Bildsten [11]): on the surface accreted material is compressed, which in turn creates heat. Due to this relation, the accurate measure of T_{eff} is of great interest. Due to the high temperatures of WDs, for which $T_{\mathrm{eff}} \gtrsim 10000\,\mathrm{K}$, the intensity of radiation peaks in the ultraviolet region. In addition, the contribution of radiation from accreting matter and the secondary star is low, and these factors allow easier measuring of T_{eff} (e.g Gänsicke et al. [12] and others). Specifically, the Lyman-α line is of great importance.

In a paper by Pala et al. [13], 40 CV systems were observed using Hubble Space Telescope in order to increase the number of CVs with known effective temperatures and WD masses. Earlier studies by Townsley and Gänsicke [14] yielded 43 CV systems with known T_{eff}. Thus, regarding the amount of systems with known T_{eff}, the amount was doubled. The evaluation of T_{eff} conducted by Pala et al. [13] seems to indicate that the theory of CV evolution has some flaws. Above the period gap ($2\,\mathrm{h} \lesssim P_{\mathrm{orb}} \lesssim 3\,\mathrm{h}$) temperatures obtained ($T_{\mathrm{eff}} \simeq 16000\,\mathrm{K} - 26000\,\mathrm{K}$) were lower than predicted by models ($T_{\mathrm{eff}} \simeq 38000 - 43000\,\mathrm{K}$). Below the gap, the temperatures vary more than predicted by theorized CV evolution. Lastly, the theorized bounce after reaching minimum period ($P_{\mathrm{orb}} \lesssim 80\,\mathrm{min}$, $T_{\mathrm{eff}} \lesssim 11500\,\mathrm{K}$) was not clearly identified. A more in-depth look at the analysis and results is provided by Pala et al. [13].

The accretion disc spectrum

The gas particles in the disc rotate differentially. Due to the nature of the gas flow in the disc, the disc can be approximated as two-dimensional, meaning it is thin in the vertical direction. The disc is also assumed to be in a steady-state, meaning there are e.g. no changes over time in the radial structure of the disc. In reality, the accumulation of material into the disc is not equivalent to the transfer of material from the disc to the star, meaning there can be changes in the thickness of the disc in the radial direction. But for the purpose of this discussion and for the construction of the following theory, steady-state is a valid assumption.

As the gas has viscosity, the particles feel a shear rate. This leads to dissipation of energy as heat and as the temperature of the gas increases, it radiates this energy away. This dissipation of energy from the faces of the disc can be written as

$$D(R) = \frac{3GM_*\dot{M}}{8\pi R^3}\left[1 - \left(\frac{R_*}{R}\right)^{1/2}\right], \tag{1.17}$$

where M_* and R_* are the mass and radius of the star, respectively, and R is some radius of the disc. Due to this dissipation of energy, we can write for the luminosity of the disc

$$L(R_1, R_2) = 2\int_{R_1}^{R_2} D(R) 2\pi R \, \mathrm{d}R = \frac{3GM_*\dot{M}}{2}\int_{R_1}^{R_2}\left[1 - \left(\frac{R_*}{R}\right)^{1/2}\right]\frac{\mathrm{d}R}{R^2}, \tag{1.18}$$

which results in

$$L_{\mathrm{disc}} = \frac{GM_*\dot{M}}{2R_*}, \tag{1.19}$$

when we integrate using limits $R_1 = R_*$ and $R_2 \to \infty$. This can be compared to the situation where all of the kinematic energy of gas particles is transformed to radiation at the surface, meaning

$$L_{\mathrm{acc}} = \frac{GM_*\dot{M}}{R_*}. \tag{1.20}$$

Thus, half of the possible energy is radiated out in the disc, and half remains to be used in the boundary layer.

From the dissipation rate $D(R)$ we can obtain a function for the temperature $T(R)$. This is possible if the disc is optically thick in the vertical direction (but still geometrically thin). In this scenario, the faces of the disc radiate as a blackbody, meaning that the dissipation rate is equal to the blackbody flux:

$$\sigma T^4(R) = D(R). \tag{1.21}$$

Using equation 1.17 we get

$$T(R) = \left\{\frac{3GM_*\dot{M}}{8\pi R^3\sigma}\left[1 - \left(\frac{R_*}{R}\right)^{1/2}\right]\right\}^{1/4}. \tag{1.22}$$

This can also be written in the form

$$T = T_*(R/R_*)^{-3/4}, \tag{1.23}$$

if $R \gg R_*$. T_* is a constant of form

$$T_* = \left(\frac{3GM_*\dot{M}}{8\pi R_*^3\sigma}\right)^{1/4}. \tag{1.24}$$

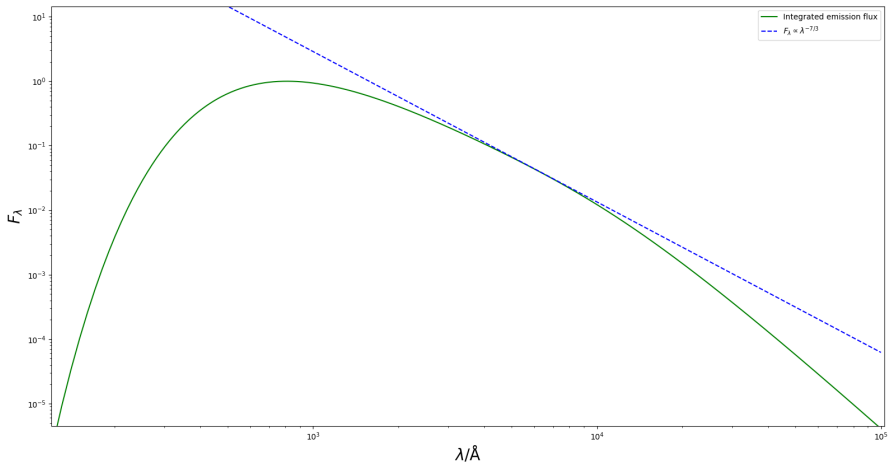

FIGURE 1.2: The integrated blackbody spectrum of an accretion disc, with $R_{\text{out}} = 35R_{\text{in}}$, where $R_{\text{in}} = R_*$.

This $T(R)$ can be used to obtain an approximation for the spectrum of the disc, because for each small slice of the disc the spectral radiance can be written as

$$I_\lambda = B_\lambda[T(R)] = \frac{2hc^2}{\lambda^5}\frac{1}{(e^{hc/\lambda kT(R)} - 1)}, \tag{1.25}$$

where $B_\lambda[T(R)]$ is the familiar Planck function for spectral radiance. Integrating this over the whole disc gives the spectrum:

$$F_\lambda = \int_{R_*}^{R_{\text{out}}} B_\lambda[T(R)]2\pi R\mathrm{d}R = \frac{2\pi hc^2}{\lambda^5}\int_{R_*}^{R_{\text{out}}} \frac{R\mathrm{d}R}{e^{hc/\lambda kT(R)} - 1}. \tag{1.26}$$

The above equation 1.26 can be evaluated in parts. When $\lambda \gg hc/kT(R_{\text{out}})$, the Planck function reduces to the Rayleigh-Jeans form $B_\lambda[T(R)] = 2ckT\lambda^{-4}$, so that from 1.26 we get $F_\lambda \propto \lambda^{-4}$. On the other hand, if $\lambda \ll hc/kT_*$, then the Planck function is reduced to the Wien form $B_\lambda[T(R)] = 2hc^2\lambda^{-5}e^{-hc/\lambda kT}$. Now $F_\lambda \propto e^{-hc/\lambda kT}$, so in the hotter part of the disc ($R \sim R_*$, $T \sim T_*$), F_λ falls exponentially. In the center region of the disc plane, $hc/kT_* \ll \lambda \ll hc/kT_{\text{out}}$. For this we write $x = hc/\lambda kT(R) \cong (hc/\lambda kT_*)(R/R_*)^{3/4}$. Thus, writing $R = (x\lambda kT_*/hc)^{4/3}$ and $\mathrm{d}R = (R/R_*)^{1/4}(4\lambda kT_*R_*/3hc)$, the integral can be written as

$$F_\lambda \propto \lambda^{-7/3}\int_{x_1}^{x_2} \frac{x^{5/3}}{e^x - 1}\mathrm{d}x \propto \lambda^{-7/3}. \tag{1.27}$$

In figure 1.2 the integrated spectrum of a disc is shown. In this case, the outer radius of the disc is set to be $R_{\text{out}} = 35R_*$. The flat part where the flux follows a power- law $F_\lambda \propto \lambda^{-7/3}$ is almost non-existent. The flatness is due to the individual blackbody peaks of each ring in the disc. When the ratio $R_{\text{out}}/R_{\text{in}}$ is sufficiently large, this flatness can be more readily seen, see figures 1.3 and 1.4.

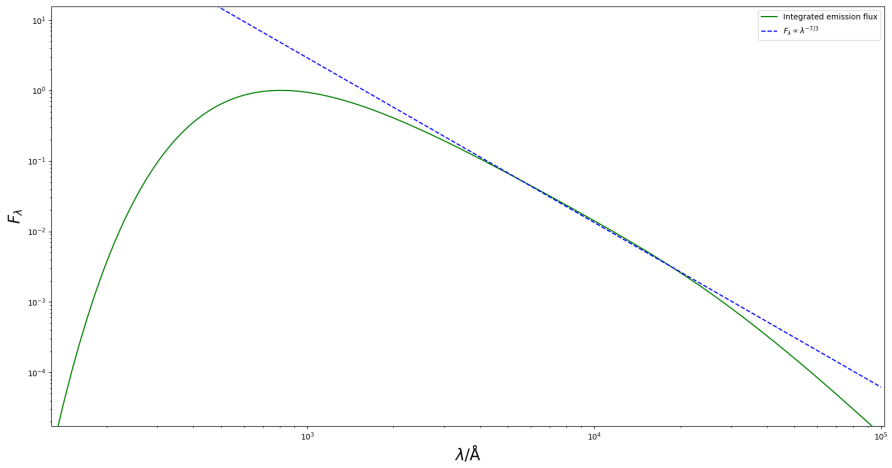

FIGURE 1.3: The integrated blackbody spectrum of an accretion disc, with $R_{\text{out}} = 100R_{\text{in}}$

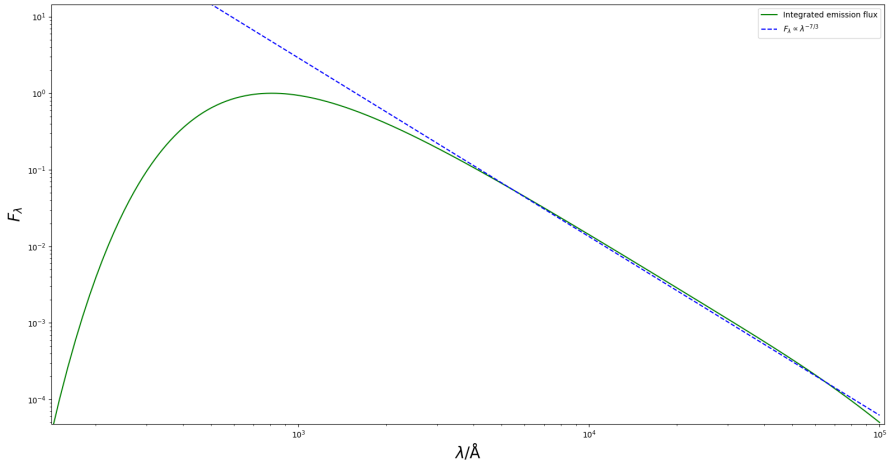

FIGURE 1.4: The integrated blackbody spectrum of an accretion disc, with $R_{\text{out}} = 500R_{\text{in}}$

The assumption of steady-state structure made above allows for easier evaluation of the disc parameters (e.g. surface density Σ, density ρ and central temperature T_c). For a steady-state structure, the time-derivatives in the conservation equations for mass and angular momentum transport are set to zero. The changes in radial structure in a geometrically thin disc happen on a viscous timescale t_{visc}. In other words, the time it takes for the viscosity to spread the matter in the disc, is given by t_{visc}. As external conditions change on timescales longer than viscous timescale, the disc can be assumed to be in a steady-state. But, making this assumption leads to theorized disc properties that are more or less independent of viscosity. Thus, comparing theory with observations is bound to bring up problems, as viscosity must be an important factor in the disc dynamics.

Changes to the disc structure (from internal mechanisms, not external) can occur on different timescales. These are the dynamical timescale t_ϕ, the thermal timescale t_{th} and t_z, which depicts the time it takes to smooth out changes to the hydrostatic equilibrium in the z-direction. These three different timescales are much shorter than the viscous timescale, which means that we can identify different instabilities of the disc. In cases where these instabilities grow and the perturbations are not damped, a steady-state is not possible. It can be shown that viscous stability is broken in the disc, when temperatures are such that hydrogen can be ionized, $T = T_{\text{H}} \sim 6500\,\text{K}$. If this condition is fulfilled in some parts of the disc, time-dependence of certain parameters must be taken into account. More in-depth discussion can be found e.g. in the book by Frank et al. [2].

1.2.6 Problem with UV spectroscopy of CVs

Observing objects in UV is not as straightforward as observing in optical. The amount of CVs observed in UV is low, which limits the study of them. One way to greatly increase this amount is to use optical spectroscopy, as much more CVs have been observed in that spectral region. Optical spectroscopy would allow for a bigger sample-size, and that in turn would mean the CV systems we observe would have a broader range in parameter values. The WD spectrum is contaminated in the optical region by e.g. the accretion disc spectrum. Thus, analysis of optical spectra and the comparison of resulting parameters (T_{eff} and $\log g$) to those obtained from UV spectra, could shed light on the possibility of using optical wavelengths in the extraction of accretion disc spectrum.

Chapter 2

Modelling stellar spectra

2.1 Stellar parameters $T_{\rm eff}$ and $\log g$

Effective temperature $T_{\rm eff}$ and surface gravity $\log g$ are the two cornerstones in modelling stellar spectra. These parameters are essential in describing the physical conditions in the atmosphere of stars and are directly related to physical properties (mass, radius and luminosity) of the star. Using analytical models for stellar atmospheres, which are constructed using the above mentioned parameters, one can compare between them and the observations. From this comparison one obtains the best match to the observed atmosphere, with specific parameter values. These obtained values can be used to check the values of the physical properties, and to see that they are consistent with values obtained in other ways. As there are objects for which these atmospheric parameters have not been determined (and neither mass/luminosity/radius for that matter), it is important that these parameters are well-defined and accurate. In our case these two parameters are most important, as they can be used solely to describe the physical phenomena of WDs. In a more general case, one would also be interested in the chemical composition of the star. But in our case, we are focused on hydrogen-rich white dwarfs (DA), so the chemical composition is known.

2.1.1 Effective temperature $T_{\rm eff}$

There is a relation between $T_{\rm eff}$ and total flux radiated by the star at the surface:

$$\sigma T_{\rm eff}^4 \equiv \int_0^\infty F_\upsilon \mathrm{d}\upsilon = F_* = \frac{L}{4\pi R_*^2}.$$

Here the temperature of a star is thought to be similar to that of a blackbody which has a similar luminosity and radius. Note, in reality the power radiated from a star at certain effective temperatures can be, and usually is, different to that of a black body. The definition of stellar surface is not strict, as it depends on the observed wavelength and type of the star. Thus, in order to assess $T_{\rm eff}$, which is a function of radius, care must be taken when evaluating R. In the book by Gray [15], radius is determined by the depth at which continuum of the stellar spectrum is formed.

If the star is at a distance D from Earth, the apparent flux of the star is $f_{\rm E} = L/4\pi D^2$. If the flux at the surface of a star is $F_* = L/4\pi R_*^2$, then from

the apparent flux the total flux can be obtained:

$$4\pi D^2 f_{\mathrm{E}} = L \quad \longrightarrow \quad \frac{4\pi D^2 f_{\mathrm{E}}}{4\pi (d/2)^2} = \frac{L}{4\pi R_*^2} \quad \longrightarrow \quad \frac{4 f_{\mathrm{E}}}{\theta^2} = F_*, \tag{2.1}$$

where d is the diameter of the star, and $\theta = d/D$ is the stellar angular diameter, which can be obtained with various methods.

2.1.2 Surface gravity $\log g$

The surface gravity is obtained from the mass and radius of the star,

$$g = g_\odot \frac{M}{R^2}.$$

The above equation is in solar units. In essence, the surface gravity measures the pressure in the photosphere.

2.2 Modelling the photosphere

In order to analyse stellar spectra that are obtained from observations, it is necessary to try to create theoretical models with known parameters, which can then be compared to these observations. Here a general idea of modelling stellar photospheres is depicted, without going into detail on how the models are created. We will also look specifically at the modelling of white dwarf spectra, as that is the first step in confirming if the optical spectra can be used to obtain T_{eff} and $\log g$. For a more detailed discussion on the subject, refer to Gray [15].

Modelling is an iterative process. The information obtained from observations of stars is used to deduce the conditions at the origin - in the atmosphere of the star. These conditions are a result of immense amount of physical phenomena, which can't all be accurately defined. As such, we must make hypotheses based on the information available, constructing the models using the observations and physical laws as the foundation. As the first models are created, they are tested against new observations, and this is the process that refines the models. When the models can match the data from observations, with acceptable accuracy, we can be somewhat satisfied. As the models depict the observational data, the properties of the star, i.e. effective temperature or surface gravity, are also properties of the models.

Few assumptions are made for basic models: 1) All physical variables are a function of one space coordinate, i.e. plane parallel geometry, 2) the photosphere has no dynamically significant mass loss, 3) granulation and starspots are negligible and 4) magnetic fields are excluded. In many cases, thermodynamic equilibrium is assumed when looked at a small volume element (local thermodynamic equilibrium, LTE). Using this assumption, the necessary parameters can all be characterized by this temperature. Lastly, the source function, which is the ratio of absorption coefficient and emission coefficient, is

thought to be of that of a blackbody. As a result of these approximations and assumptions, the models are described by temperature and pressure, which both are given as a function of optical depth.

Making accurate calculations for individual stars in order to model them is time consuming. A faster way is to use a grid of models, which have a range of values for effective temperature, surface gravity and for chemical composition, if that is also required. The use of a grid is further encouraged, if one uses a scaled temperature. In essence, a known temperature distribution, such as that of our Sun, is scaled by using an arbitrary scaling constant. Using this approach is notably faster than making the required radiative equilibrium calculations individually for every star in question.

2.2.1 Fitting observed spectra with theoretical models

Stellar spectra can be analysed in different ways, depending on what one wants to know about the object in question. Regarding the observation of WDs, the best way to gain knowledge is to look at its strongest lines. Using optical spectra, for DA-type WDs, the most prominent lines are Balmer lines (Finley et al. [16]). DA-type means the WD atmosphere is rich in hydrogen, with maybe traces of other elements (i.e. Helium). Due to this, the interesting part of the spectrum is located at $4000\,\text{Å} \lesssim \lambda \lesssim 6600\,\text{Å}$. The H$\epsilon$ line at $\sim 3970\,\text{Å}$, and the lines below are usually weak compared to the continuum around them, so they are disregarded from studies. Thus lines going up to Hα are used when studying DA-type WDs (some exceptions are discussed later).

In order to assess the two important parameters of stellar spectra, T_{eff} and $\log g$, the observed spectra must be fitted with model spectra, as discussed above. As also mentioned before, the most efficient way to evaluate observed spectra is to use a model grid. We used a grid of LTE pure-hydrogen models from Detlev Koester[1] (Koester 2010), which we retrieved from the Theoretical Spectra Web Server. The models assume local thermodynamic equilibrium, which is a valid assumption with lower temperatures ($T < 40000\,\text{K}$). In our studies of cataclysmic variable stars, we constrict our study to objects with $T_{\text{eff}} < 20000\,\text{K}$, so these models work well. The model grid of D. Koester also takes into account the effects of convection in the atmosphere. As shown by, e.g, Bergeron et al. [17], these models reproduce both UV and optical line profiles of DA stars with convective atmospheres accurately.

The task of the fitting routine is to minimize the quantity called squared chi, χ^2. It has the form of

$$\chi^2 = \sum_{i=1}^{n} \left(\frac{f_{\text{ob}}(\lambda_i) - f_{\text{th}}(\lambda_i, T_{\text{eff}}, \log g)}{\sigma_i} \right)^2 . \tag{2.2}$$

Here f_{ob} is the observed spectrum, σ_i is the uncertainty of each measurement, or the spectral noise at each point i of the F spectrum. So, in essence, χ^2 is the difference between observed and some model spectrum, summed over

[1] http://svo2.cab.inta-csic.es/theory/newov2/

each data point and weighed by the spectral noise at each wavelength. For a more in-depth discussion about this method, look at e.g the PhD thesis by Voß [18].

The expectation value of the χ^2 distribution is equal to the number of degrees of freedom of the distribution, or

$$N = n_{\text{ob}} - n_{\text{th}}, \tag{2.3}$$

where n_{ob} is the number of data points and $n_{\text{th}} = 2$, corresponding to the two directions of the model grid, temperature and surface gravity. For a good fit, one expects to find an expectation value of ~ 1 for χ^2/N, which is called reduced χ^2. If the value is much higher, it means the fit is not good. A large value for χ^2 can be the result of a few bad data points with very high value, and due to this the absolute χ^2 is not a useful indicator for a good fit. Instead, the relative χ^2 can be used to identify good fits.

The program used for the fitting of observed spectra is provided by Dr. Vitaly Neustroev.

2.2.2 Normalization of spectra

Usually people normalize. However, in cases where the observed spectrum can be accurately flux calibrated, normalizing the data is not always necessary. Normalizing is also not an easy or a quick task, so not doing it can be the right choice. It can also affect the underlying accretion disc spectrum, which we are trying to extract. As the data we are using is accurately flux calibrated (SDSS, X-Shooter and efosc), we are not incentivized to normalize. Nevertheless, we showcase later the results obtained from normalized WD spectra, to show the impact on obtained parameters.

2.3 Analysing White Dwarf spectra

Before modelling CVs, the modelling method was rigorously tested to assess its accuracy. Single WD spectra were modelled, and obtained parameters T_{eff} and $\log g$ were compared to database values. Further, modified theoretical spectra of single WDs were modelled, and resulting parameters were compared to original values.

Eight single WDs, for which the spectra are not contaminated by e.g. accretion discs or companion stars, were chosen from Montreal White Dwarf Database[2] (MWD) with parameter values $10000\,\text{K} < T_{\text{eff}} < 20000\,\text{K}$ and $8.00 < \log g < 9.00$. The average value for surface gravity of WDs in CV systems is observed to be $\log g = 8.35$, as stated in e.g. the paper by Wijnen et al. [19]. This corresponds to $M = 0.85 M_{\odot}$. The spectra were taken from the SDSS DR14 database. Bright stars were chosen for high S/N. In the SDSS database, wavelengths are given in vacuum wavelengths. These need to be transformed to air wavelengths, and the equation for this is given in the SDSS

[2] https://www.montrealwhitedwarfdatabase.org/

TABLE 2.1: Eight stars chosen for modelling single WD spectra. Best fits and resulting parameters are shown.

Object	Object name	Database $T_{\rm eff}$[K]	Model $T_{\rm eff}$[K]	Database $\log g$	Model $\log g$	Magnitude (u)
1	SDSS J143336.11+375140.1	10493 K	10500 K	8.58	9.00	17.76
2	SDSS J110600.57+621017.1	10207 K	10750 K	8.67	9.00	17.68
3	SDSS J12222957-02433.25	11421 K	16000 K	8.27	8.00	17.15
4	GD 59	13043 K	12750 K	8.02	8.00	15.70
5	PG 0101+059	14890 K	13750 K	8.45	8.25	16.18
6	SDSS J204446.30+153311.7	17062 K	17250 K	8.26	8.25	15.89
7	SDSS J073237.88+420454.3	18136 K	25000 K	8.40	8.75	16.49
8	PG 1325+168	20114 K	19250 K	8.29	8.25	16.41

webpage:

$$\mathrm{AIR} = \mathrm{VAC}/(1.0 + 2.735182 \cdot 10^{-4} + 131.4182/(\mathrm{VAC}^2 + 2.76249 \cdot 10^8)/\mathrm{VAC}^4).$$

2.3.1 Modelling optical spectra of WDs

The chosen objects were modelled using a convolved model grid. Convolving is required in order to take into account the finite spectral resolution of observed spectra. The grid starts at $T_{\rm eff} = 8000\,\mathrm{K}$ and $\log g = 7.50$, and for each temperature value the surface gravity goes from 7.50 to 9.50 with steps of 0.25. The temperature increases in steps of 250 K until 20000 K, after which it increases in steps of 1000 K to 40000 K, which is the highest value. Best fits are shown in figures 2.1-2.4. The resulting parameter values are shown in Table 2.1. Each spectrum was cut at $\lambda \approx 5050$ Å. At the bluer part of the spectrum, all the objects except PG 0101+059, SDSS J204446.30+153311.7 and PG 1325+168 (see figures 2.3a, 2.4a and 2.4b) were cut below H9. As can be seen from Table 2.1, all model temperatures except for objects 3 and 7 are within $\Delta T = 1200\,\mathrm{K}$ from database values. Usual accuracy when comparing obtained $T_{\rm eff}$ from different models is $\Delta T = 1000\,\mathrm{K}$. Obtained $\log g$ is within $\Delta \log g = 0.50$. Usual accuracy is $\Delta \log g = 0.25$.

We proceeded to model modified spectra of our objects, where the continuum was cut out and the total wavelength range of the spectrum was limited. The results for these tests are shown in figures 2.5-2.8. Notice that object SDSS J12222957-02433.25 has been left out of further evaluation due to bad data points, and that object PG 1325+168 has two spectra shown. The resulting values are shown in Table 2.2, and also a comparison between the results of the first two tests is shown in Table 2.3. Only small changes in obtained temperature values are seen.

Modelling normalized spectra

As already noted, normalizing a spectrum is a valid approach when dealing with objects for which flux calibration can not be done accurately or it is altogether impossible. As these objects are from the SDSS catalogue, they are flux calibrated. Nevertheless, we modelled normalized spectra of five objects. The results are shown in figures 2.9-2.11, and in the table 2.4. In conclusion, we are able to replicate $T_{\rm eff}$ and $\log g$ values from the database

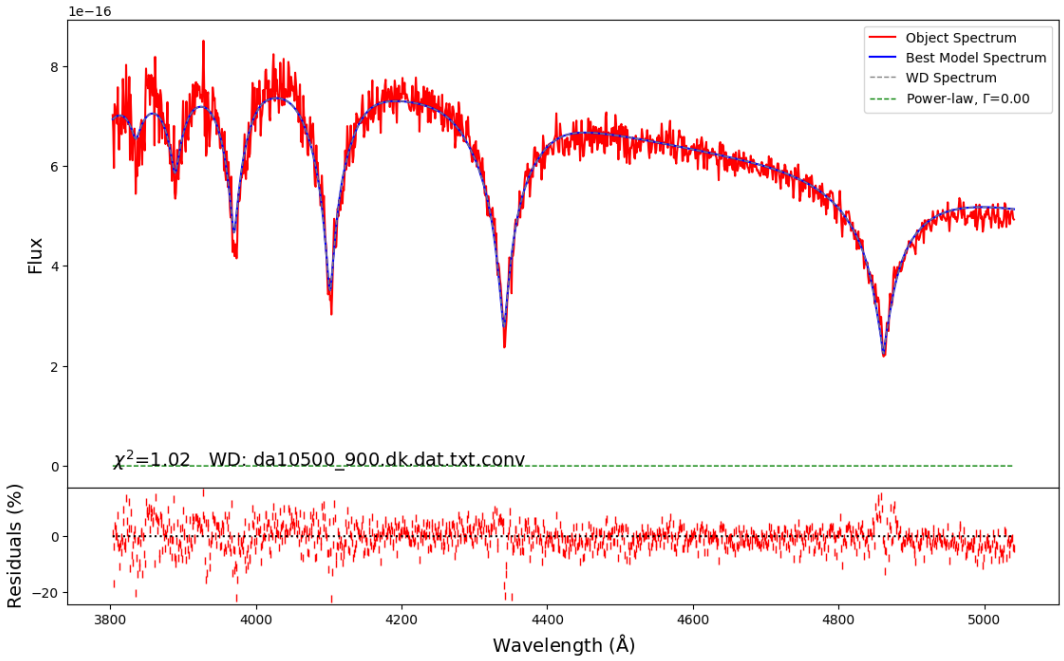

(A) SDSS J143336.11+375140.1

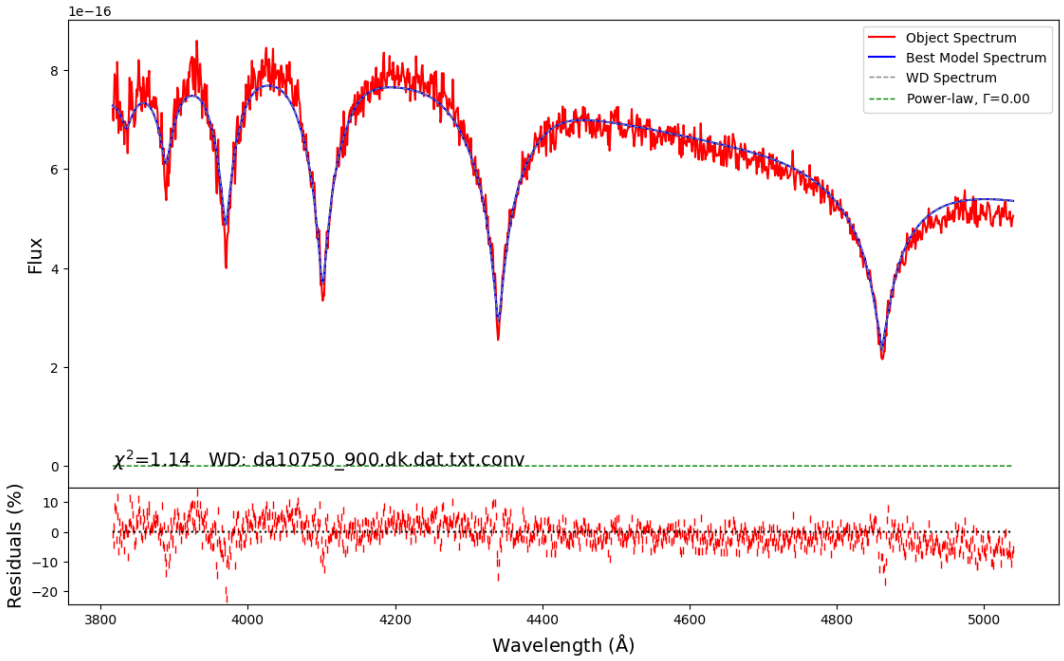

(B) SDSS J110600.57+621017.1

FIGURE 2.1: Objects SDSS J143336.11+375140.1 and SDSS J110600.57+621017.1 fit with Koesters models.

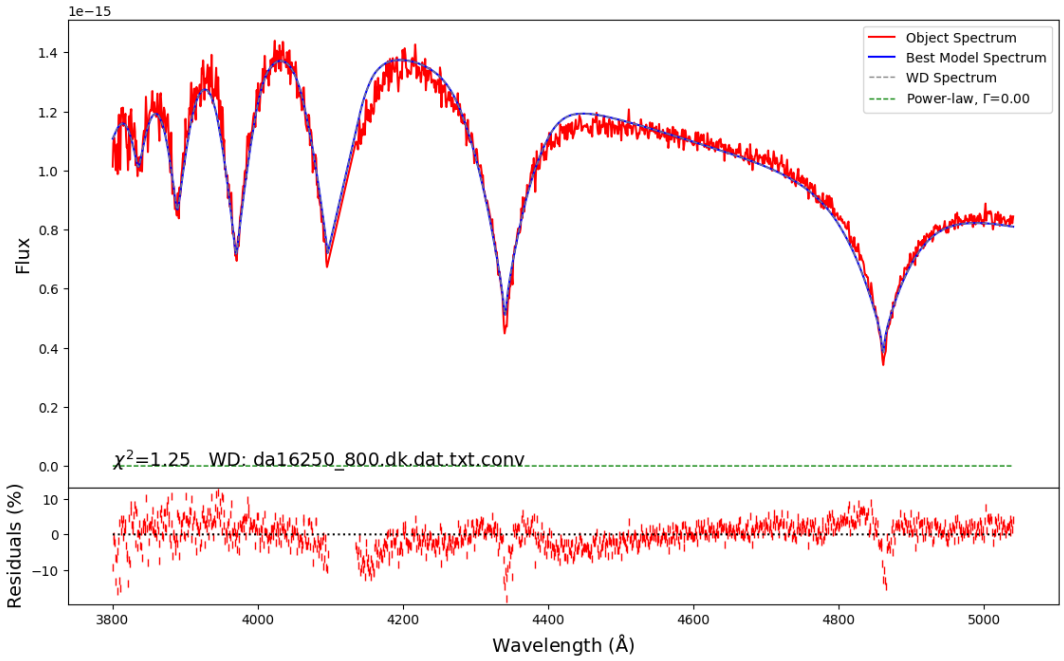

(A) SDSS J12222957-02433.25

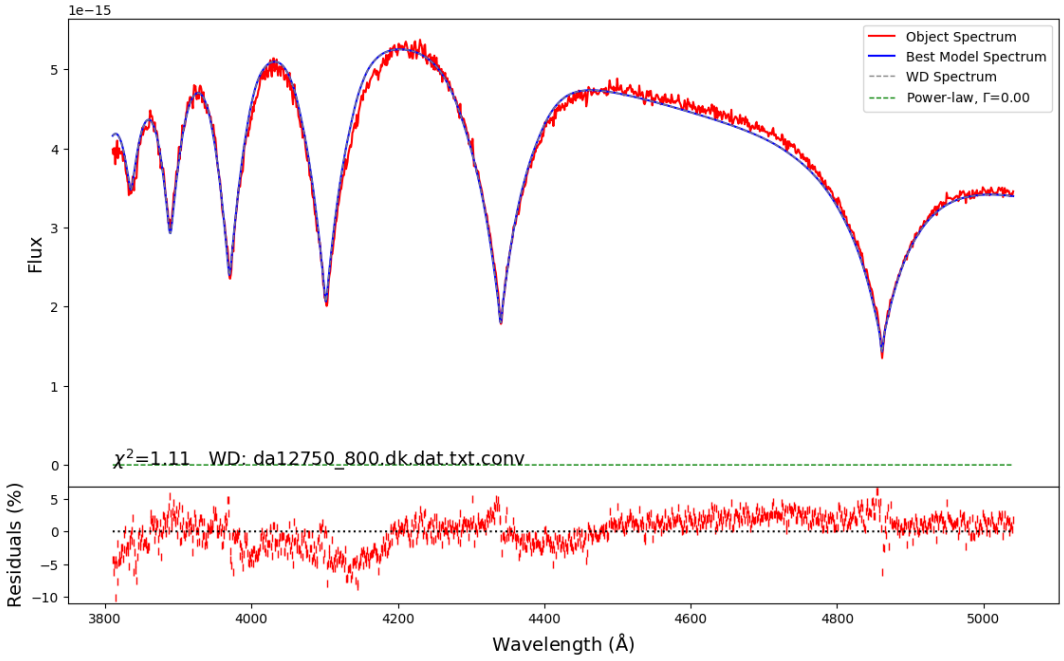

(B) GD 59

FIGURE 2.2: Objects SDSS J12222957-02433.25 and GD 59 fit with Koesters models.

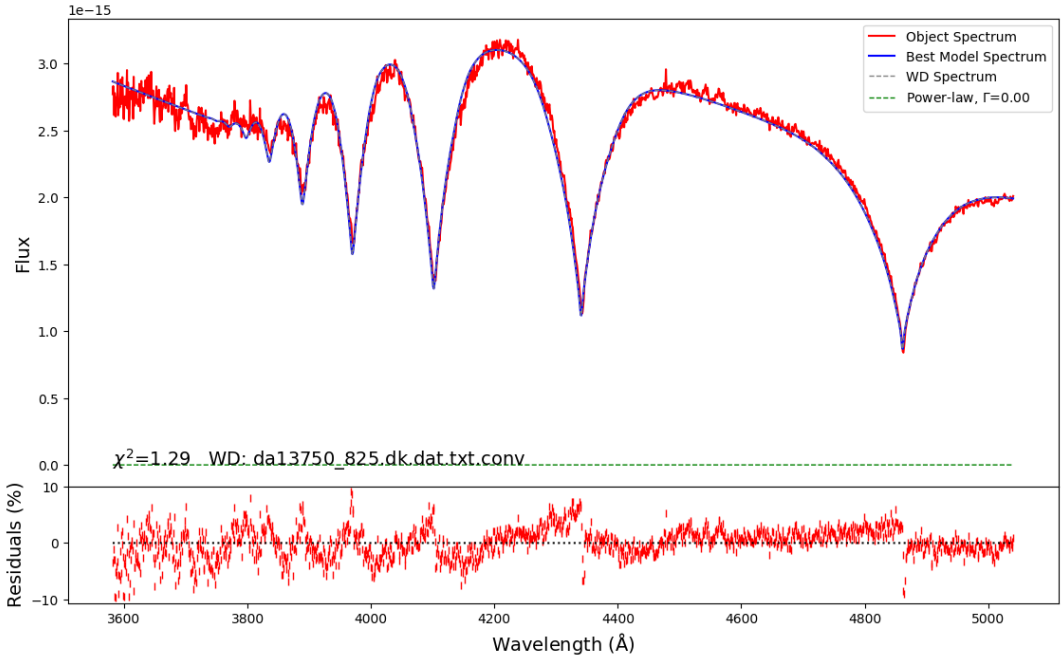

(A) PG 0101+059

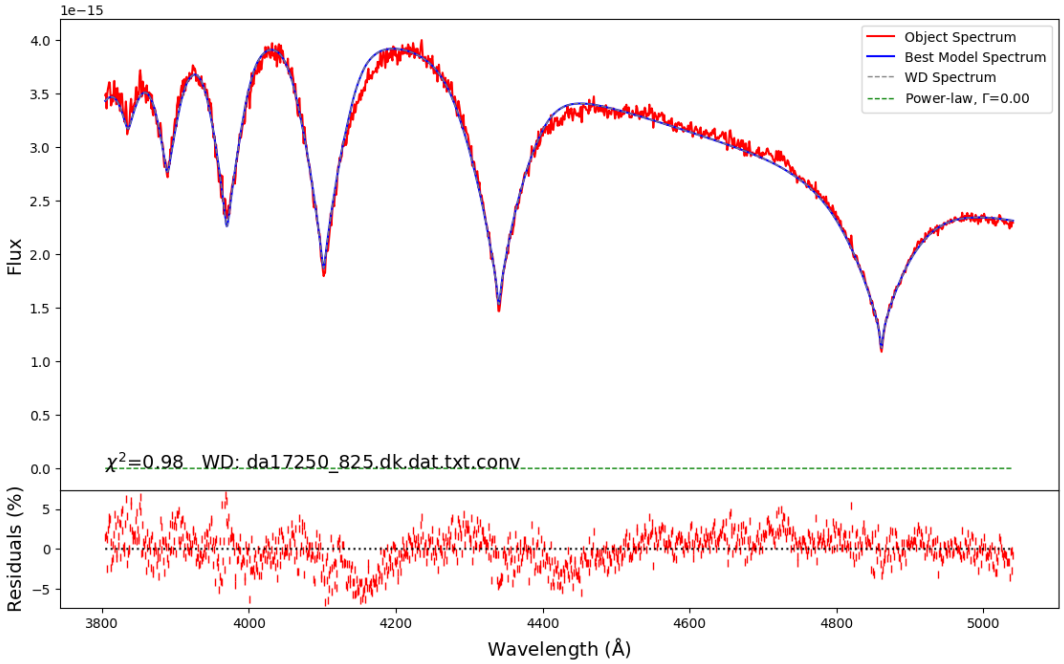

(B) SDSS J204446.30+153311.7

FIGURE 2.3: Objects PG 0101+059 and SDSS J204446.30+153311.7 fit with Koesters models.

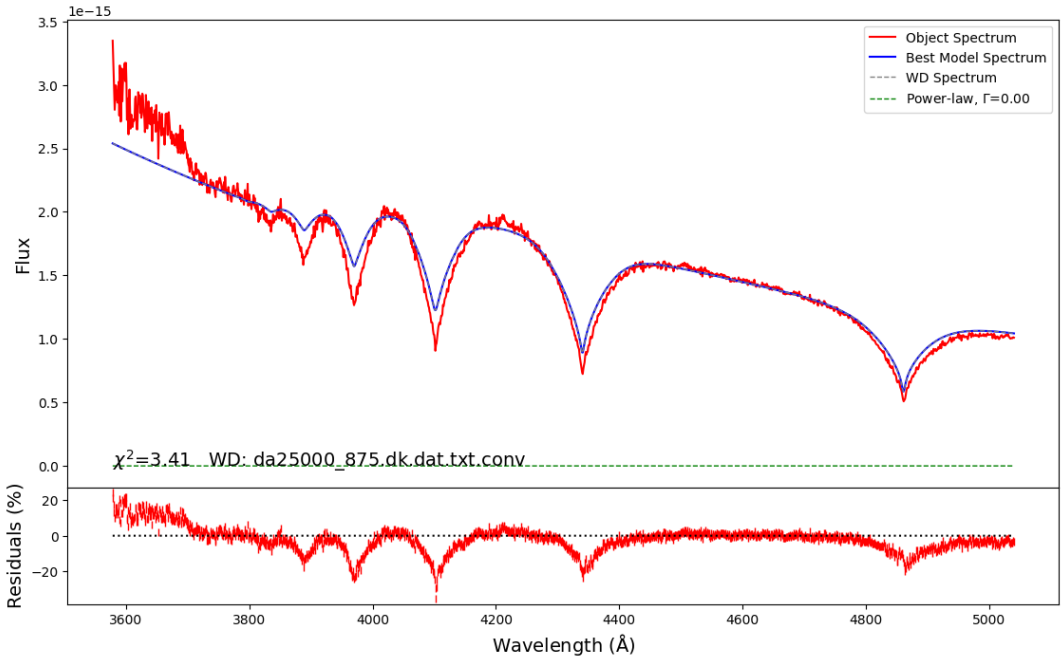

(A) SDSS J073237.88+420454.3

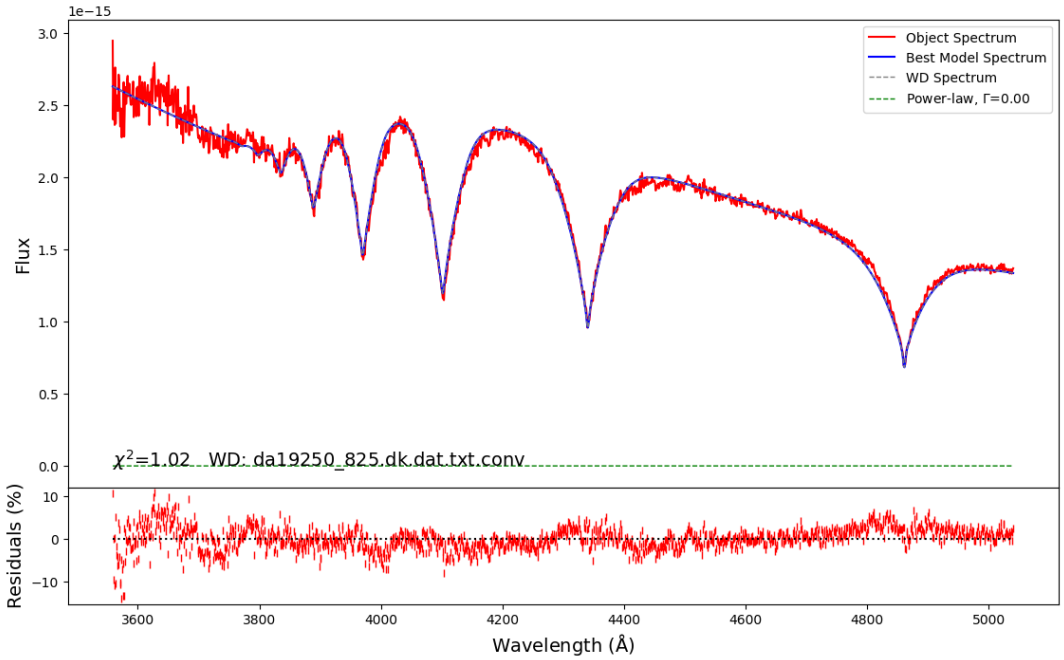

(B) PG 1325+168

FIGURE 2.4: Objects SDSS J073237.88+420454.3 and PG 1325+168 fit with Koesters models.

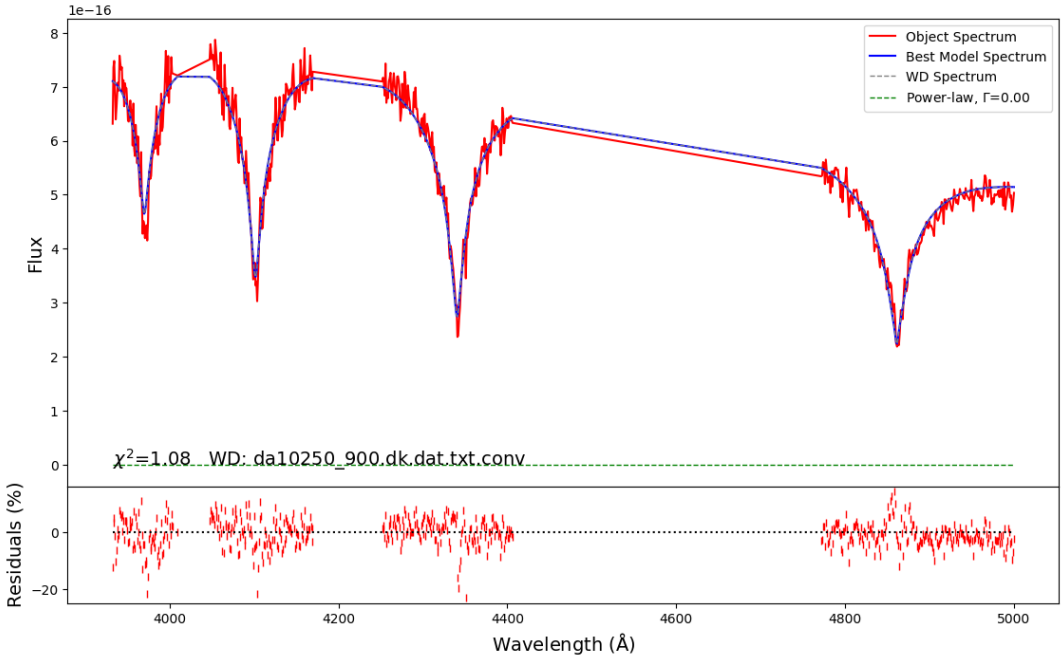

(A) SDSS J143336.11+375140.1, cut at $\lambda_{\text{min}} \approx 3930\,\text{Å}$ and $\lambda_{\text{max}} \approx 5000\,\text{Å}$. Continuum flux has been cut out.

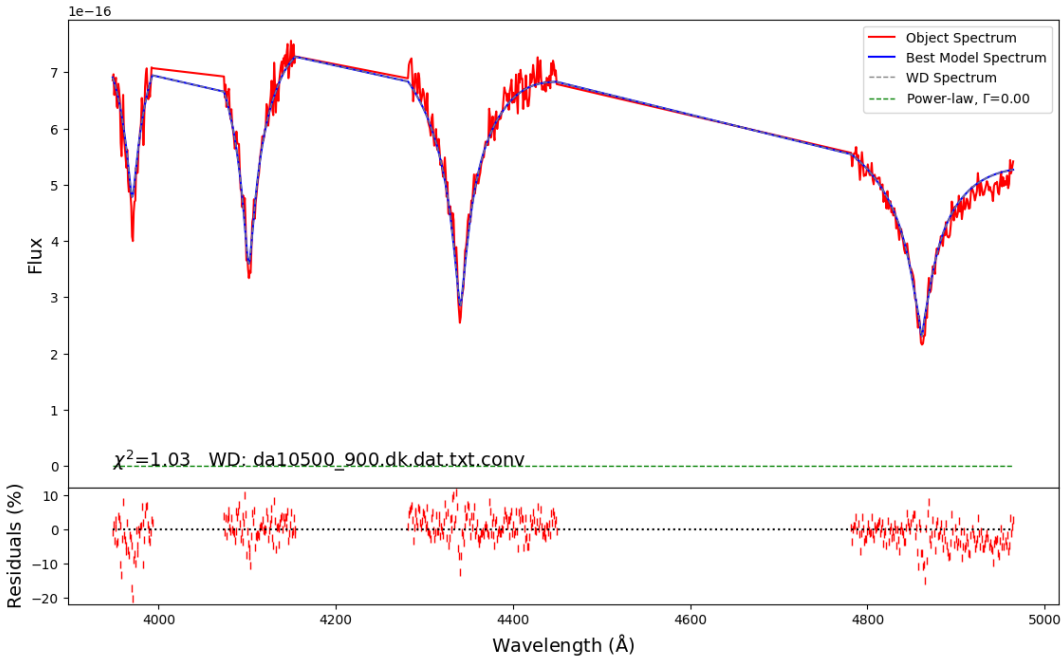

(B) SDSS J110600.57+621017.1, cut at $\lambda_{\text{min}} \approx 3950\,\text{Å}$ and $\lambda_{\text{max}} \approx 4960\,\text{Å}$. Continuum flux has been cut out.

FIGURE 2.5: Objects SDSS J143336.11+375140.1 and SDSS J110600.57+621017.1.

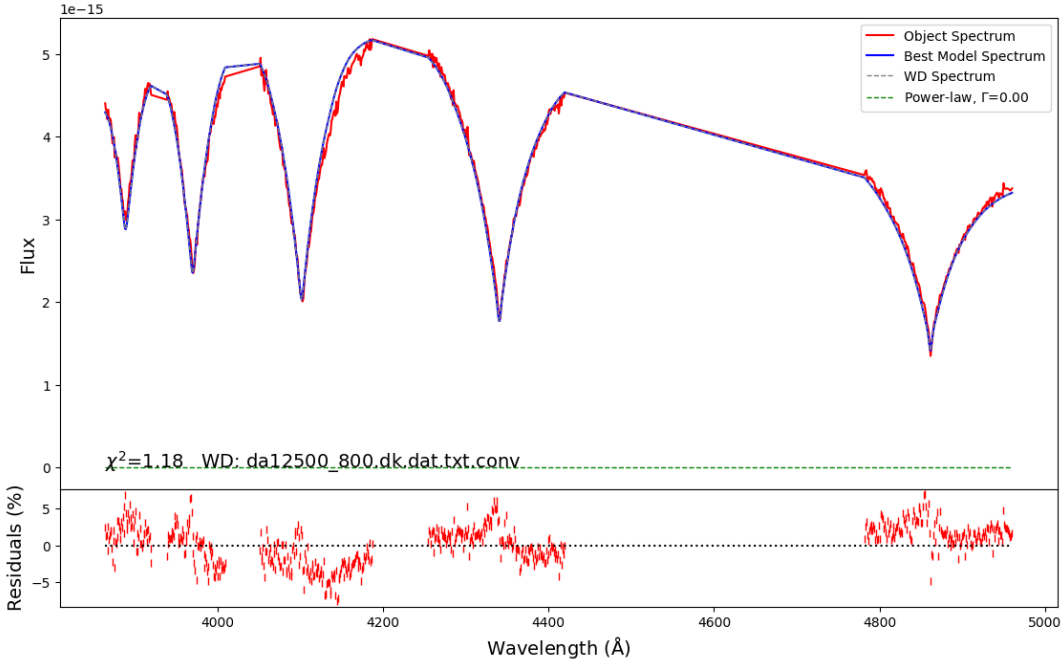

(A) GD 59, cut at $\lambda_{\text{min}} \approx 3864$ Å and $\lambda_{\text{max}} \approx 4960$ Å. Continuum flux has been cut out.

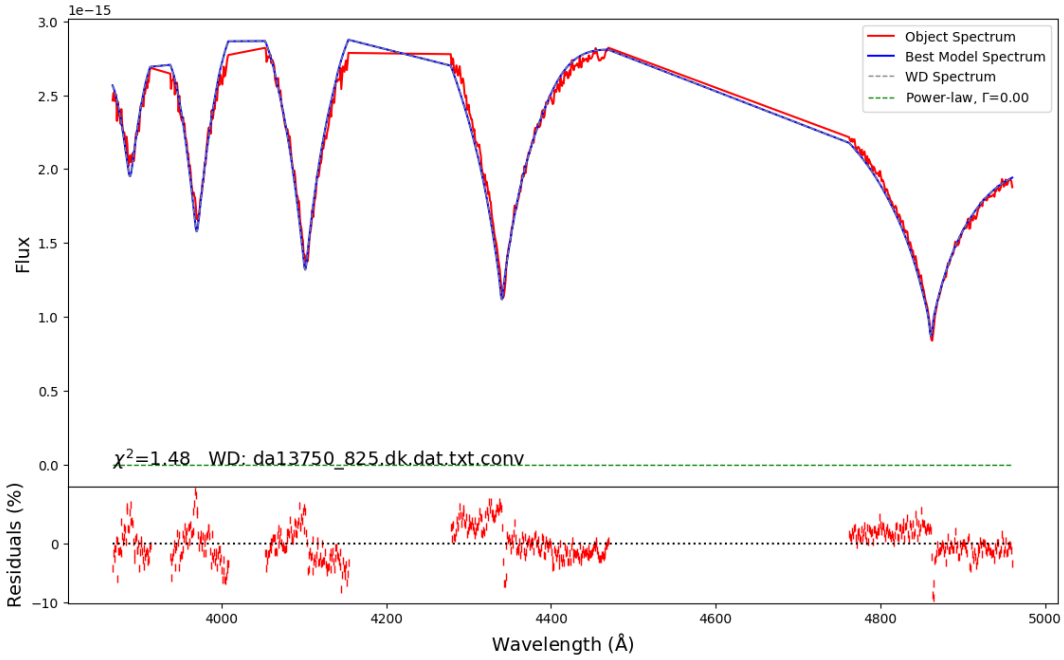

(B) PG 0101+059, cut at $\lambda_{\text{min}} \approx 3864$ Å and $\lambda_{\text{max}} \approx 4960$ Å. Continuum flux has been cut out.

FIGURE 2.6: Objects GD 59 and PG 0101+059.

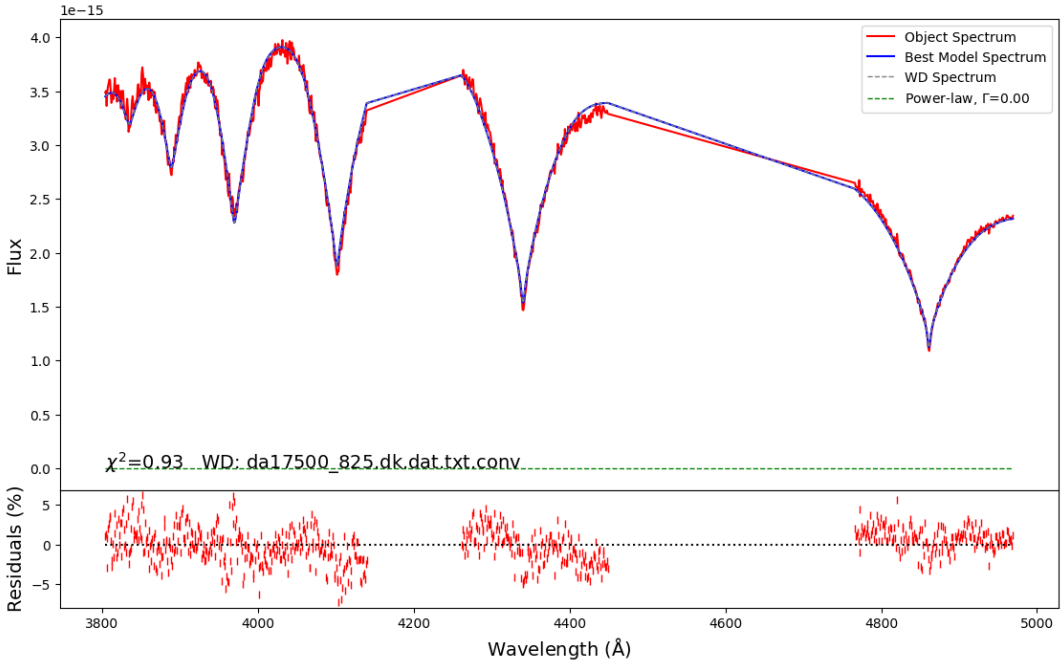

(A) SDSS J204446.30+153311.7, cut at $\lambda_{\text{min}} \approx 3804\,\text{Å}$ and $\lambda_{\text{max}} \approx 4969\,\text{Å}$. Continuum flux between Hβ-Hγ and Hγ-Hδ has been cut.

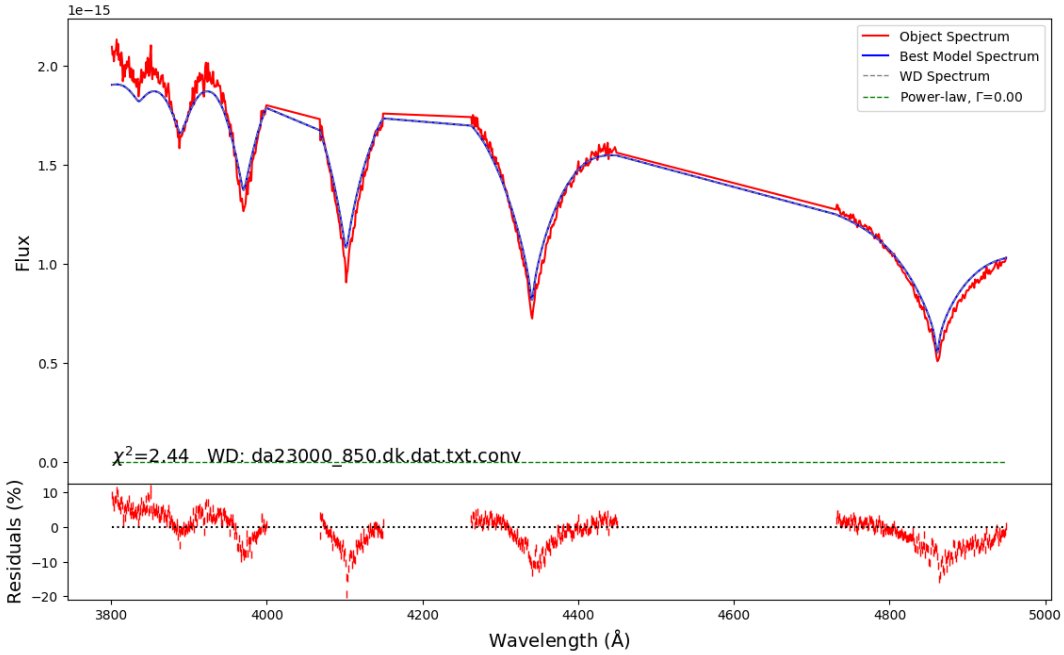

(B) SDSS J073237.88+420454.3, cut at $\lambda_{\text{min}} \approx 3801\,\text{Å}$ and $\lambda_{\text{max}} \approx 4950\,\text{Å}$. Continuum flux between Hβ-Hγ, Hγ-Hδ and Hδ-Hϵ has been cut.

FIGURE 2.7: Objects SDSS J204446.30+153311.7 and SDSS J073237.88+420454.3.

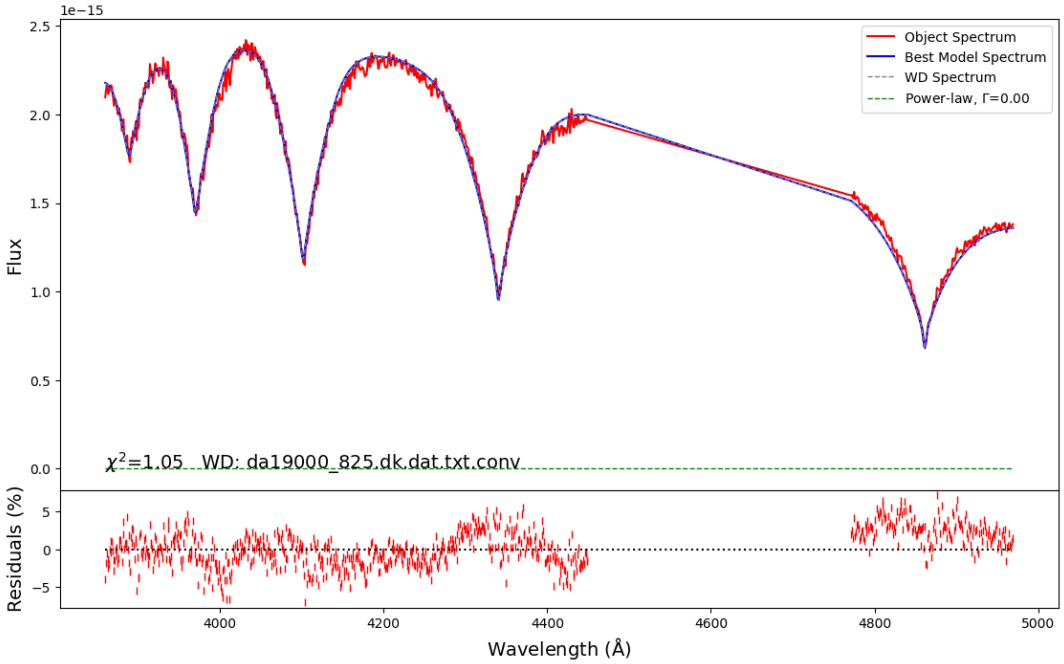

(A) PG 1325+168, cut at $\lambda_{\text{min}} \approx 3860$ Å and $\lambda_{\text{max}} \approx 4969$ Å. Continuum flux between Hβ-Hγ has been cut.

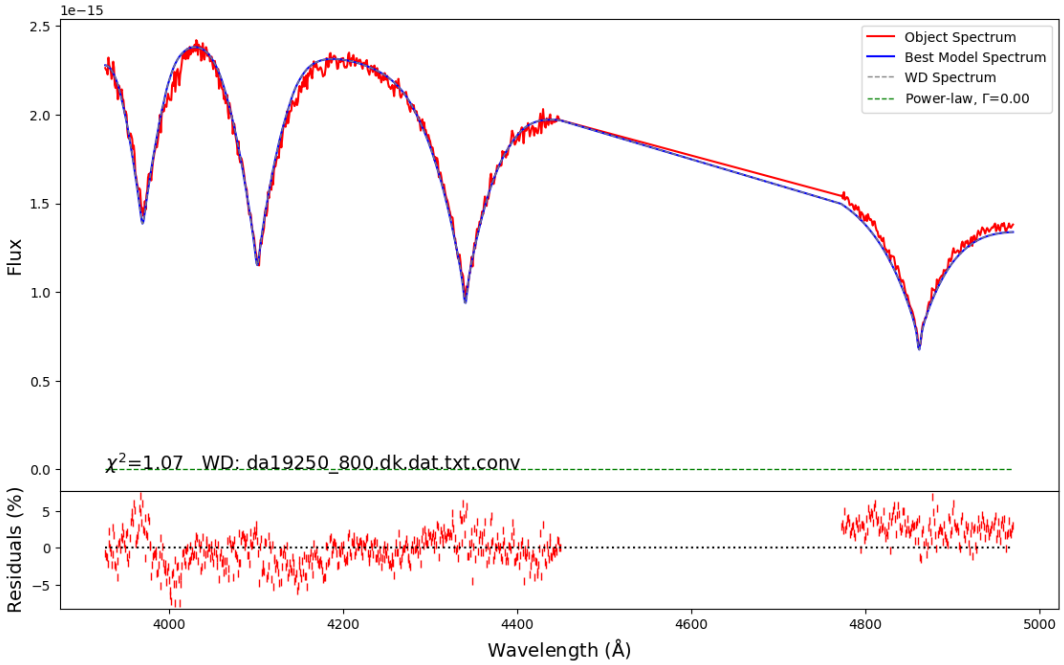

(B) PG 1325+168, cut at $\lambda_{\text{min}} \approx 3927$ Å and $\lambda_{\text{max}} \approx 4969$ Å. Continuum flux between Hβ-Hγ has been cut.

FIGURE 2.8: Object PG 135+168.

TABLE 2.2: Resulting best fits for the modified spectra of all objects except SDSS J1222-02, which was left out due to bad data points.

Object	**Object name**	**Database** T_{eff}	**Model** T_{eff}	**Database** $\log g$	**Model** $\log g$
1	SDSS J143336.11+375140.1	10493 K	10250 K	8.58	9.00
2	SDSS J110600.57+621017.1	10207 K	10500 K	8.67	9.00
4	GD 59	13043 K	12500 K	8.02	8.00
5	PG 0101+059	14890 K	13750 K	8.45	8.25
6	SDSS J204446.30+153311.7	17062 K	17500 K	8.26	8.25
7	SDSS J073237.88+420454.3	18136 K	23000 K	8.40	8.50
8	PG 1325+168	20114 K	19000 K	8.29	8.25
8	PG 1325+168	20114 K	19250 K	8.29	8.00

TABLE 2.3: Comparison between resulting parameter values from modelling between unaltered and altered spectra.

Object	**Object name**	**Model** $T_{\text{eff},1}$	**Model** $T_{\text{eff},2}$	**Model** $\log g_1$	**Model** $\log g_2$
1	SDSS J143336.11+375140.1	10500 K	10250 K	9.00	9.00
2	SDSS J110600.57+621017.1	10750 K	10500 K	9.00	9.00
4	GD 59	12750 K	12500 K	8.00	8.00
5	PG 0101+059	13750 K	13750 K	8.25	8.25
6	SDSS J204446.30+153311.7	17250 K	17500 K	8.25	8.25
7	SDSS J073237.88+420454.3	25000 K	23000 K	8.75	8.50
8	PG 1325+168	19250 K	19000 K	8.25	8.25
8	PG 1325+168	19250 K	19250 K	8.25	8.00

TABLE 2.4: Resulting best fits for the normalized spectra of objects 1, 2, 4, 6 and 8.

Object	**Object name**	**Database** T_{eff}	**Model** T_{eff}	**Database** $\log g$	**Model** $\log g$
1	SDSS J143336.11+375140.1	10493 K	10000 K	8.58	8.50
2	SDSS J110600.57+621017.1	10207 K	10500 K	8.67	8.50
4	GD 59	13043 K	14500 K	8.02	7.75
6	SDSS J204446.30+153311.7	17062 K	17750 K	8.26	8.00
8	PG 1325+168	20114 K	21000 K	8.29	7.75

with accuracy of $\Delta T_{\text{eff}} < 1200\,\text{K}$ and $\Delta \log g < 0.50$. Modifying the spectra does not reduce accuracy, and normalization does not increase accuracy.

A final note on SDSS J073237.88+420454.3: as can be seen in e.g. the figure 2.4a, a peculiar rise can be seen in the UV part of the spectrum. It is reminiscent of the Balmer jump that can be seen in CVs due to the accretion disc. We spent considerable time modelling this object, as our resulting parameter values were clearly off the mark. We chose not to include this object when evaluating the possibility of using optical spectra for the study of CVs. We later obtained the parameters with reasonable accuracy, through normalization of the spectrum. It was the only object where normalization was the only way to obtain comparable results with database values, which is in itself interesting.

2.3.2 Modelling modified theoretical single WD spectra

In addition to modelling single WD spectra, we modelled modified theoretical single WD spectra. As we know the model parameters, we know exactly what results we can expect. As seen in figure 1.1 the WD spectrum is contaminated e.g. by the accretion disc. By modelling modified theoretical spectra, we can see how our modelling method is able to recover the correct parameters. In essence, we treat the modified theoretial spectrum as if it was the spectrum of a CV star.

We introduced noise into the spectrum according to a wanted signal-to-noise ratio. We also cut a portion of the linecore out for multiple lines. The width of the emission line, and thus the width of absorption line to be cut, is related to the rotational velocity of the accretion disc. Lastly, we introduced a term, i.e. a power-law contribution, which is one theoretical way an accretion disc can affect the spectrum of a CV system.

Noise was added to a model spectrum with parameter values $T_{\text{eff}} = 12000\,\text{K}$ and $\log g = 8.35$. We used S/N values of 20, 50 and 100. Noise was generated using Gaussian distribution. Next, linewidths to be cut were determined using velocities 1000 km/s, 2000 km/s and 3000 km/s. The width is determined from $\Delta\lambda = \lambda_0 v/c$. The obtained widths are shown in table 2.5. A best fit to the spectrum is shown in figure 2.12, the rest in Appendix A. The χ^2 value should now be ignored, as there are no error values for this spectrum with noise. As can be seen, all best fits except one (fig. A.3) replicate the parameter values of the original model. It must be noted, that the

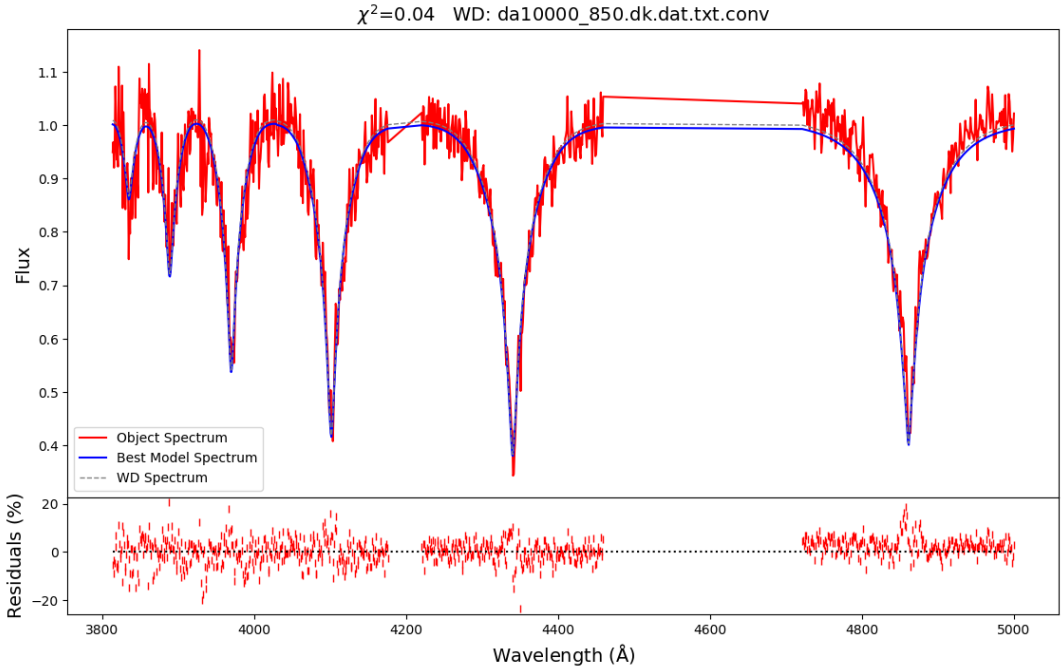

(A) Normalized spectrum of SDSS J143336.11+375140.1.

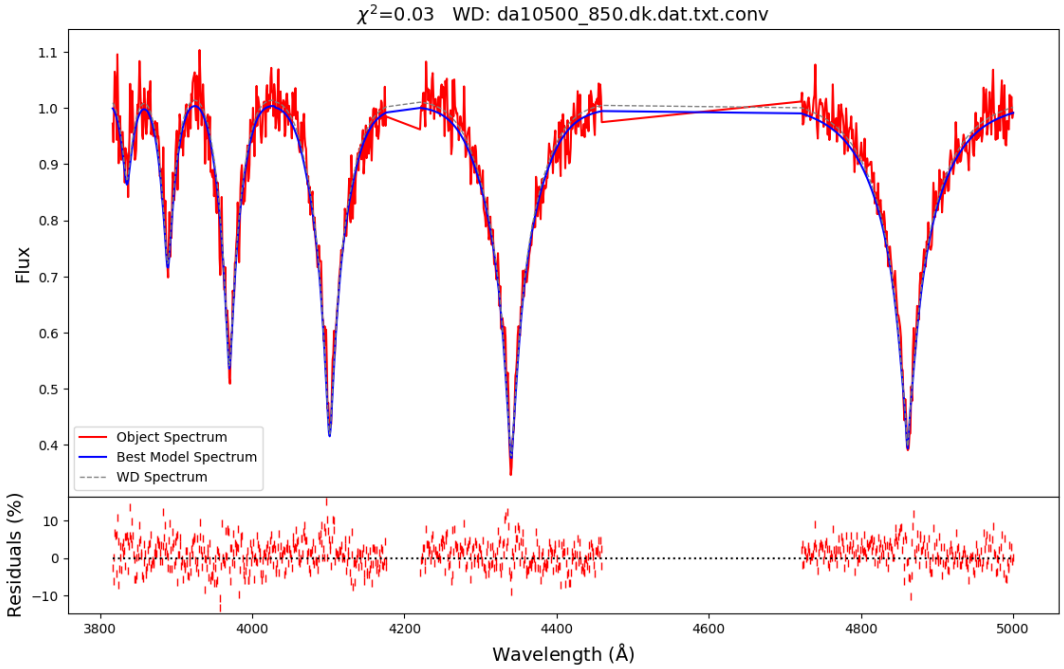

(B) Normalized spectrum of SDSS J110600.57+621017.1.

FIGURE 2.9: Objects SDSS J143336.11+375140.1 and SDSS J110600.57+621017.1 normalized to the continuum.

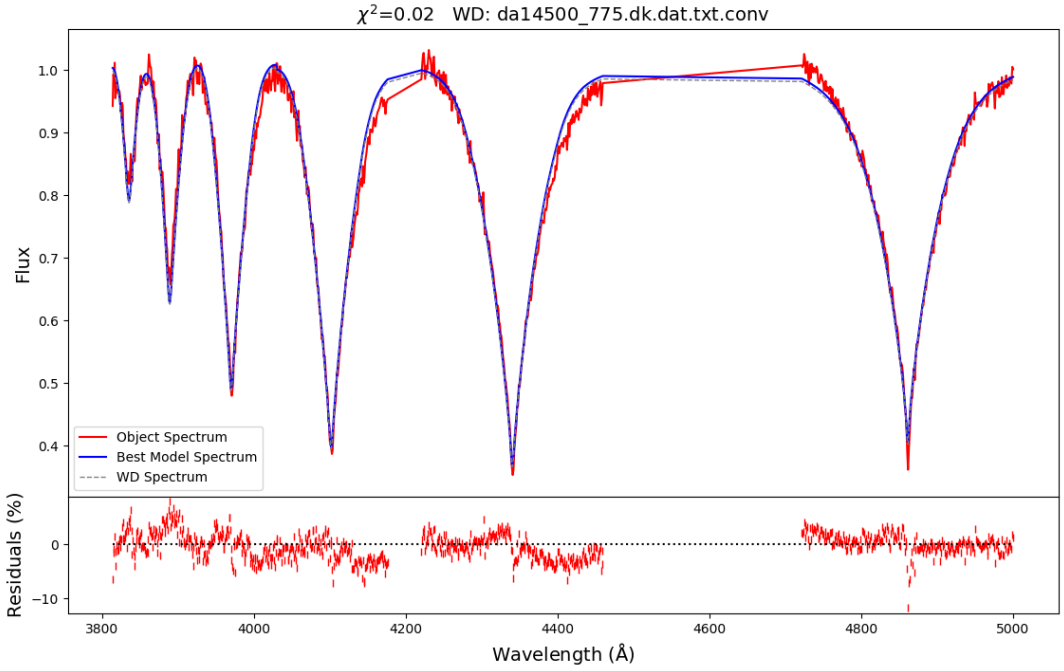

(A) Normalized spectrum of GD 59.

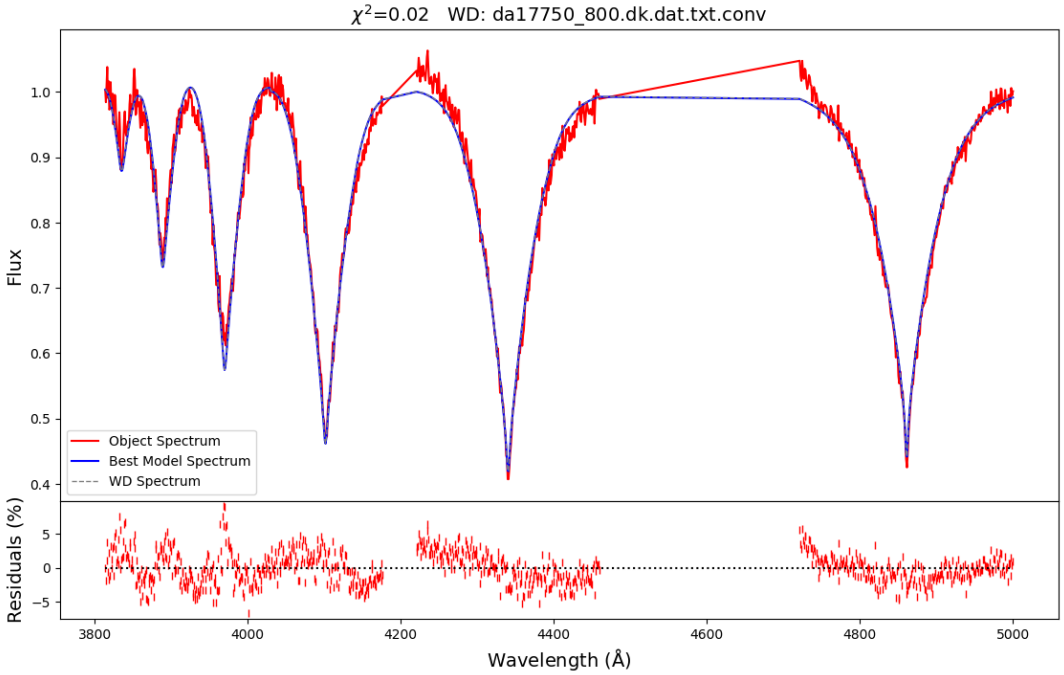

(B) Normalized spectrum of SDSS J204446.30+153311.7.

FIGURE 2.10: Objects GD 59 and SDSS J204446.30+153311.7 normalized to the continuum.

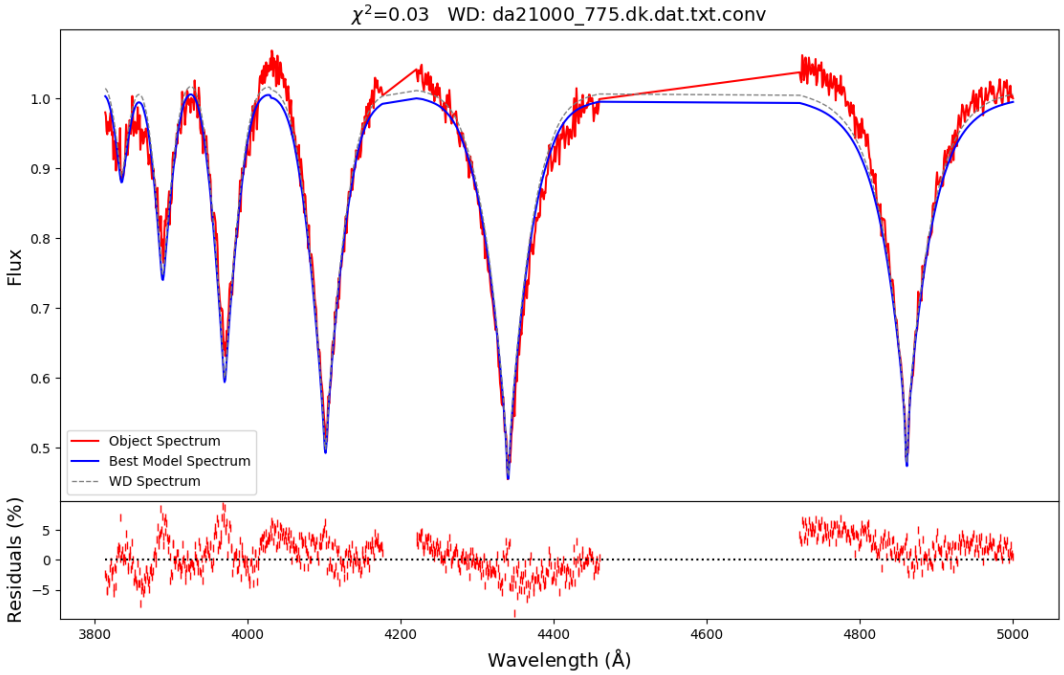

FIGURE 2.11: Object PG 1325+168 normalized to the continuum.

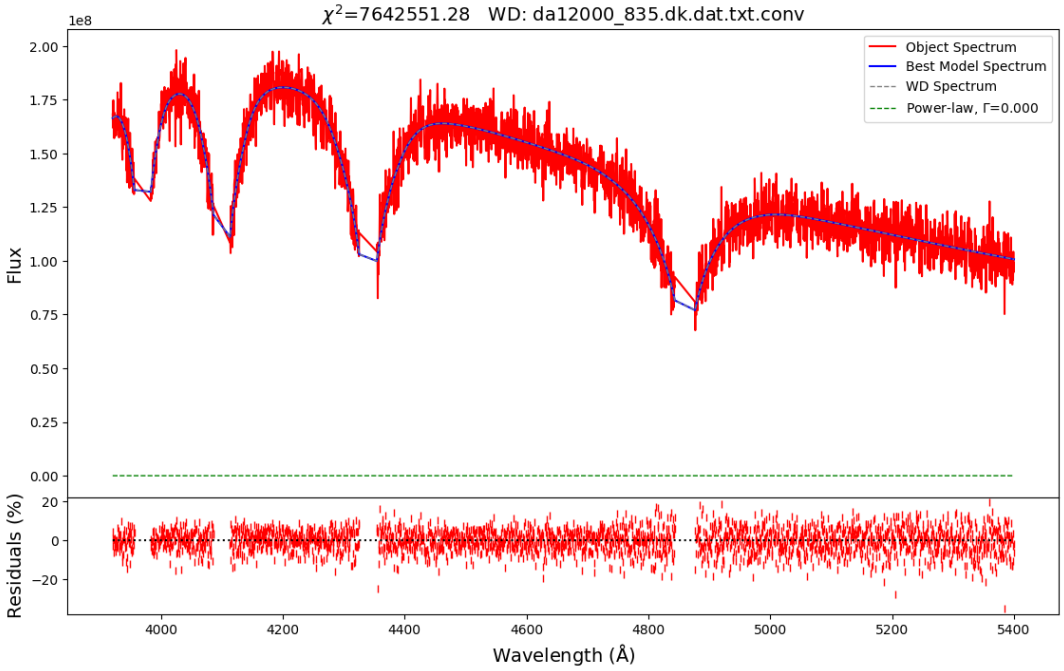

FIGURE 2.12: Spectrum with S/N=20 and $v = 1000\,\mathrm{km/s}$.

TABLE 2.5: Linewidths for each line that need to be cut off due to the rotational velocity of the accretion disc giving rise to emission lines inside the white dwarfs absorption lines.

Rotational velocity v	**H**ϵ	**H**δ	**H**γ	**H**β
$\pm$ 1000 km/s	$\pm$ 13 Å	$\pm$ 14 Å	$\pm$ 14 Å	$\pm$ 16 Å
$\pm$ 2000 km/s	$\pm$ 26 Å	$\pm$ 27 Å	$\pm$ 29 Å	$\pm$ 32 Å
$\pm$ 3000 km/s	$\pm$ 40 Å	$\pm$ 41 Å	$\pm$ 43 Å	$\pm$ 49 Å

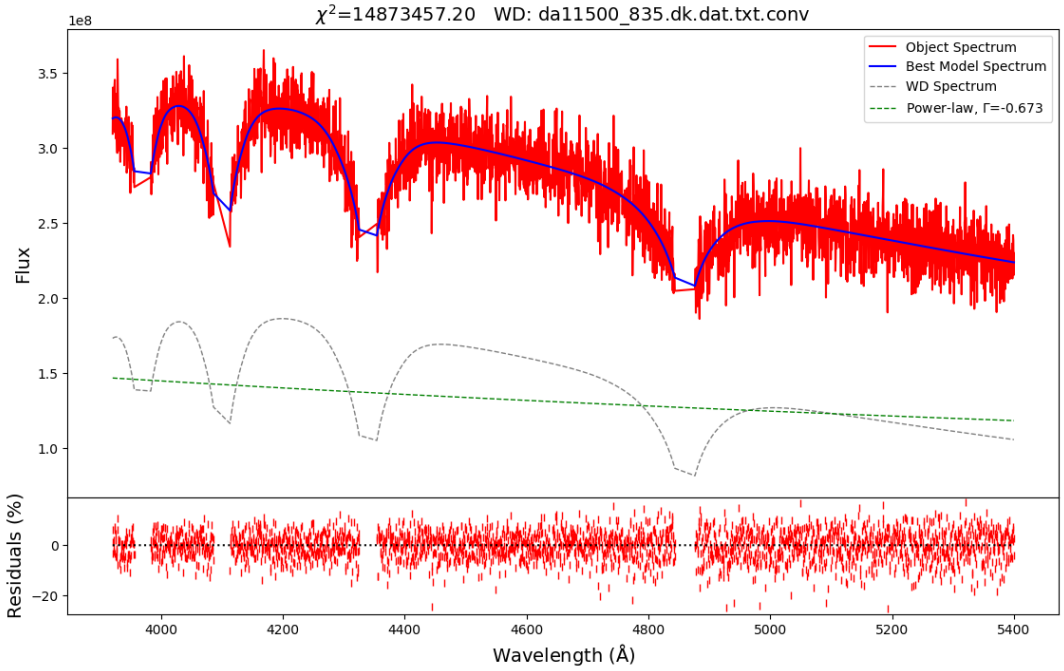

FIGURE 2.13: Spectrum with S/N=20, $v = 1000\,\mathrm{km/s}$ and power-law flux contribution of 100%.

surface gravity value was locked to 8.35, meaning that only the temperature value in the models was allowed to change. Even with $v = 3000\,\mathrm{km/s}$, the modelling method is able to reproduce the correct spectrum. But as it can be seen, the lines are almost completely cut off, and analysing such spectrum in reality might be difficult. Further analysis made in this section is done with $v = 1000\,\mathrm{km/s}$ and $v = 2000\,\mathrm{km/s}$.

Next, we introduced a term to the model spectrum, to act as if there was a power-law component due to an accretion disc. The first batch of results are done with $\log g = 8.35$, the second batch with both parameters free to change. One best fit is shown in figure 2.13, the rest are shown in appendix B. Figures B.1-B.11 show results with $\log g = 8.35$. Here we can see some deviation on the temperature value with lower S/N values (figures B.6 and B.9), $\Delta T = \pm 1500\,\mathrm{K}$. Figures B.12-B.26 show results where both parameters are free. We can see that now $\Delta T_{\mathrm{eff}} = 500\,\mathrm{K}$ and $8.00 \leq \log g \leq 8.75$.

We also modelled a modified spectrum with $T_{\mathrm{eff}} = 18000\,\mathrm{K}$ and $\log g =$

7.75. We obtained T_{eff} with $\Delta T_{\text{eff}} \leq 1250\,\text{K}$, $\log g$ was correctly modelled in all cases.

Rotational broadening of spectra

The rotation velocity of a star has an effect on the spectrum called rotational broadening. In essence, the spectrum is redshifted or blueshifted, depending on whether we observe the receding limb, or the approaching limb, of the star. The rotational velocity of a star has to be below the break-up velocity, which we can evaluate as follows: assuming keplerian angular velocity, the circular velocity will be $v_{\text{c}} = R_* \Omega_{\text{K}}$. Here $\Omega_{\text{K}} = (GM_*/R_*^3)^{1/2}$, where $R_* = 0.01 R_\odot$ and $M_* = 0.85 M_\odot$. This gives for a WD of average mass and radius $v_{\text{c}} \approx 4000\,\text{km/s}$. At this rotational velocity, the period of the white dwarf would be $P \sim 10\,\text{s}$. The objects of our interest have periods larger than this, so the rotational velocity will be smaller than this, as it needs to be. If we are to discern the spectrum of the accretion disc from the total spectrum of the system, we need to know how strong the effects of rotational broadening can be. Rotational broadening can be applied to a theoretical spectrum using e.g. the method outlined by Gray [15].

We used a non-convolved model spectrum with parameters $T_{\text{eff}} = 14000\text{K}$ and $\log g = 8.25$. Below in figures 2.14-2.15 we can see the effects of rotational broadening to a spectrum. The depth of the lines rises and the peaks broaden, hence the name. As the velocity rises, effects can also be seen in the continuum on the blue part of the spectrum. Also the wings of the lines are now affected. We can see from figure 2.14a, that even with rotational velocity of 1000 km/s, the effect is small, and thus should be negligible. Nevertheless, we verify this by modelling. The resulting best fit can be seen in figure 2.16. We are able to obtain the correct parameters, and thus rotational broadening should have only negligible effect on the spectrum, as the stars rotational velocity is much lower than 1000 km/s.

Zeeman-splitting

A WD can have a magnetic field of varying strength. The field can be seen in the spectrum of the star as a triplet pattern in the absorption lines. This is due to the atomic levels splitting into three equidistant sub-levels (Moran et al. [20]), which is called Zeeman-splitting. The two sub-levels are shifted and this shift can be calculated as

$$\Delta\lambda_L \simeq 4.7 \cdot 10^{-7} \lambda^2 B_{\text{s}}, \tag{2.4}$$

where λ depicts the wavelength of the radiation and is in Angstroms, and the average magnetic field strength B_{s} is in MG. When $B_{\text{s}} < 20\,\text{MG}$, the Zeeman-effect is linear. If $B_{\text{s}} > 20\,\text{MG}$, the linear effect is replaced by a quadratic form. A strong magnetic field will disrupt the formation of the inner part of the disc. For CV WDs with very strong magnetic fields, no accretion disc is formed, as the accreting matter is controlled by the field lines. These objects are called *Polars*. Polars have large linear and circular polarization in

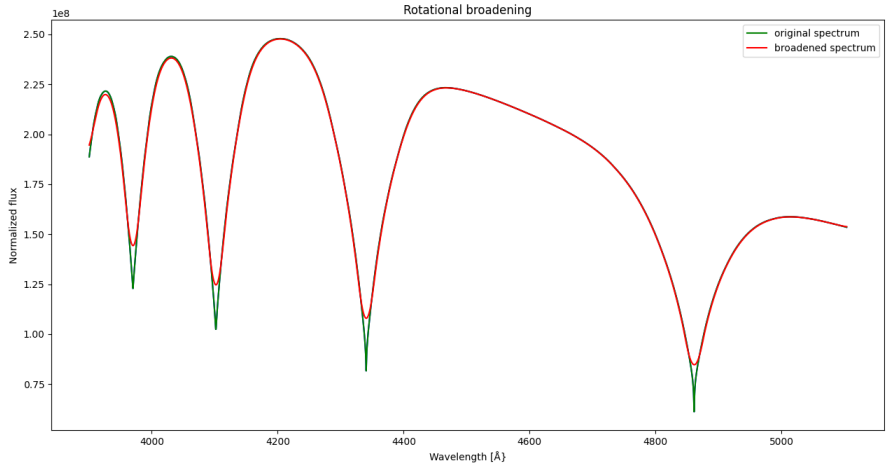

(A) Spectrum with rotational broadening due to rotational velocity of 1000 km/s.

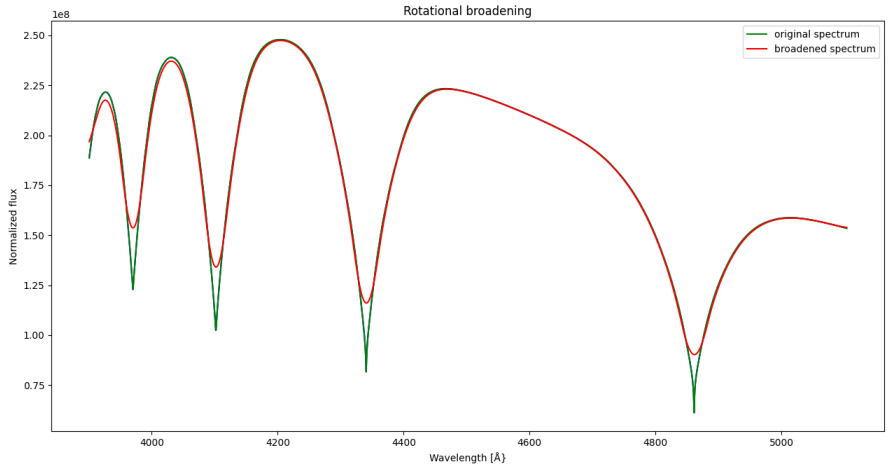

(B) Spectrum with rotational broadening due to rotational velocity of 1500 km/s.

FIGURE 2.14: Effect of rotational broadening on spectra with different rotational velocity terms.

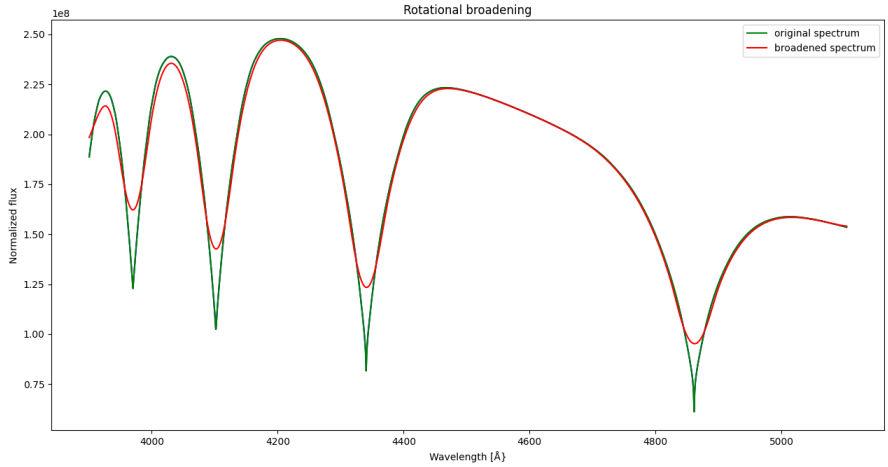

(A) Spectrum with rotational broadening due to rotational velocity of 2000 km/s.

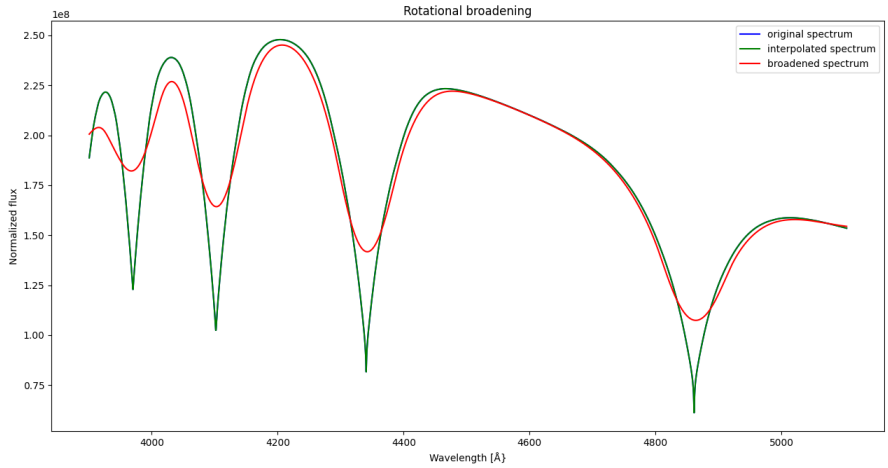

(B) Spectrum with rotational broadening due to rotational velocity of 3500 km/s.

FIGURE 2.15: Effect of rotational broadening on spectra with different rotational velocity terms.

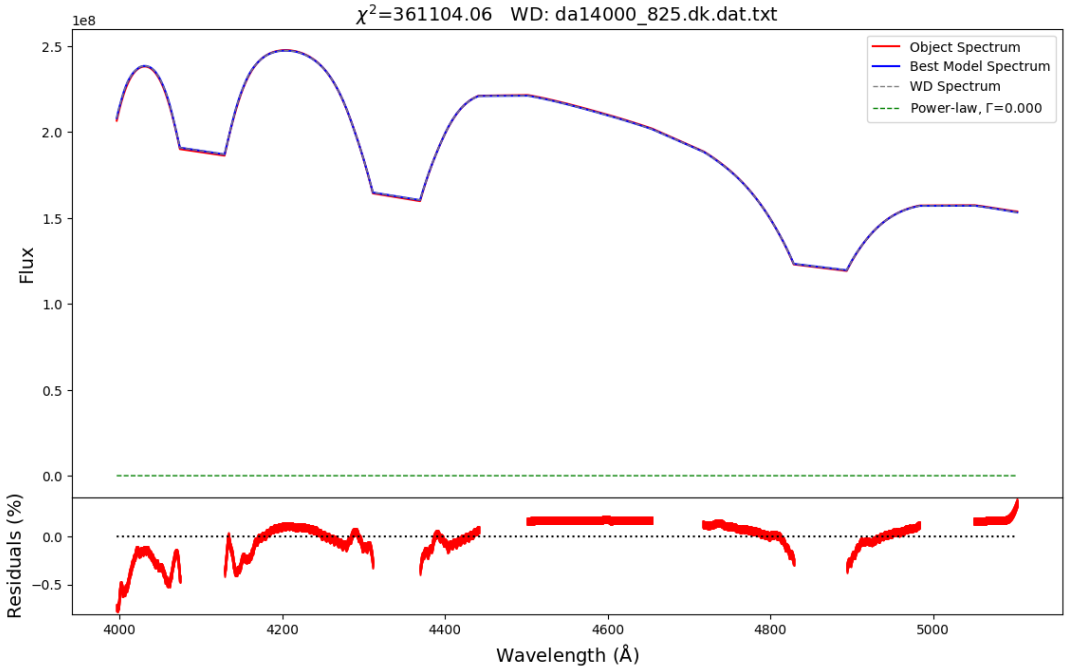

(A) Best fit to a model spectrum with rotational broadening ($v_r = 1000\,\mathrm{km/s}$) and lines cut according to $v_{r,ac} = 2000\,\mathrm{km/s}$.

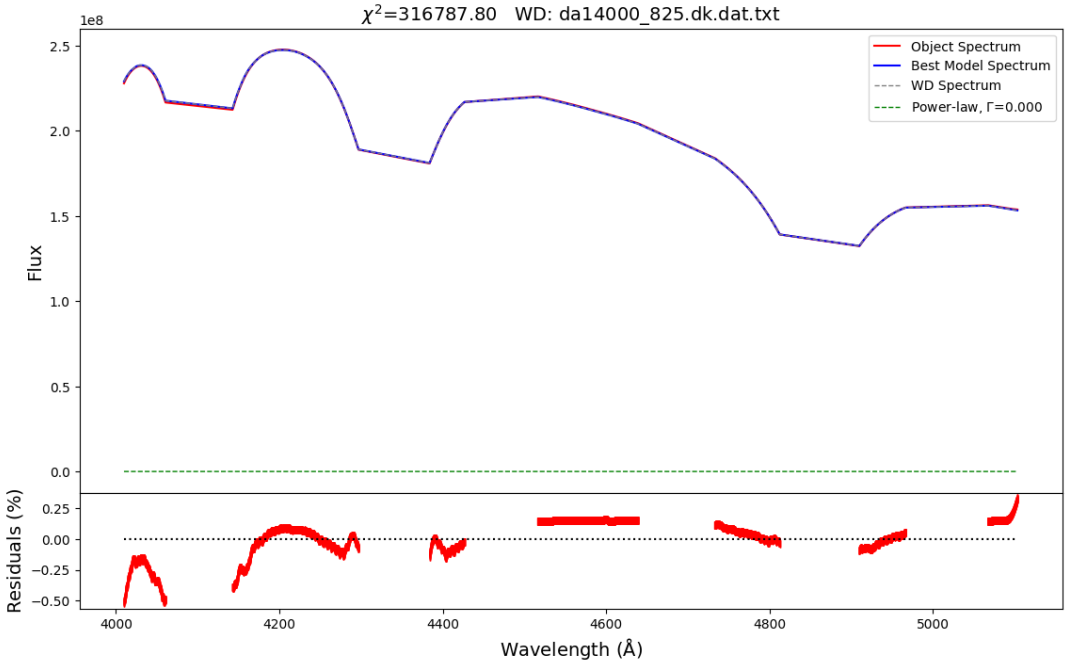

(B) Best fit to a model spectrum with rotational broadening ($v_r = 1000\,\mathrm{km/s}$) and lines cut according to $v_{r,ac} = 3000\,\mathrm{km/s}$.

FIGURE 2.16: Best fit to a model spectrum with rotational broadening and lines cut.

the optical regime in addition to strong X-ray emission. Polars rotate synchronously, i.e. the WD rotates at the same rate as the orbital motion. There are also objects called *Intermediate Polars*, which have weaker magnetic fields than polars. The circular polarization for IPs should be observable in optical wavelengths if $B_s \lesssim 10\,\mathrm{MG}$. They can be distinguished from polars due to their asynchronous rotation. Intermediate polars can have accretion discs, as the generated magnetosphere is not large enough. Refer to e.g. Warner [3] for a more thorough discussion on these objects.

For our objects, $B_\mathrm{s} \leqslant 0.5\,\mathrm{MG}$. This is clearly in the linear regime of Zeeman effect. Thus, we again took a model spectrum with parameters $T_\mathrm{eff} = 14000\,\mathrm{K}$, $\log g = 8.25$, and manually calculated the effect on the lines Hβ-Hϵ. After the shifts to longer and shorter wavelengths were calculated, they were combined together with the central part, giving us the total spectrum. In the figure 2.17 one can see the difference between a model spectrum unaffected by the Zeeman-effect, and one affected by it. In addition to the linecores having triplets, the continuum is slightly altered. The wings of the lines are also broadened. This can be more easily seen when we model the spectrum, and the results can be seen in figures 2.18-2.19. For 2.18, linecores have been cut according to $v_\mathrm{r,ac} = 1000\,\mathrm{km/s}$, and for 2.19 according to $v_\mathrm{r,ac} = 2000\,\mathrm{km/s}$. Figures 2.20-2.21 show best fits for spectra with noise applied (S/N = 30), for $B_\mathrm{s} = 300\,\mathrm{KG}$ and $B_s = 500\,\mathrm{KG}$. For lower values of B_s we are able to recover the correct parameters.

2.3.3 Conclusion

We modelled spectra of single WDs, modified theoretical spectra of single WDs, and tested the effects of rotational broadening and zeeman-effect on WD spectra. We showed that we are able with reasonable accuracy ($\Delta T_\mathrm{eff} < 1200\,\mathrm{K}$, $\Delta \log g < 0.50$) to obtain the parameters of single WDs. We showed that we are able to recover the parameters of modified theoretical single WD spectra with $\Delta T_\mathrm{eff} = \pm 1500\,\mathrm{K}$ for $\log g = 8.35$, and $\Delta T_\mathrm{eff} = 500\,\mathrm{K}$ for $8.00 \leq \log g \leq 8.75$. Lastly, we measured the effect of rotational broadening and zeeman-effect on a theoretical spectrum, and showed that with reasonable $v_c \ll 1000\,\mathrm{km/s}$ and $B_\mathrm{s} \leq 300\,\mathrm{MG}$, we are able to recover the correct parameters.

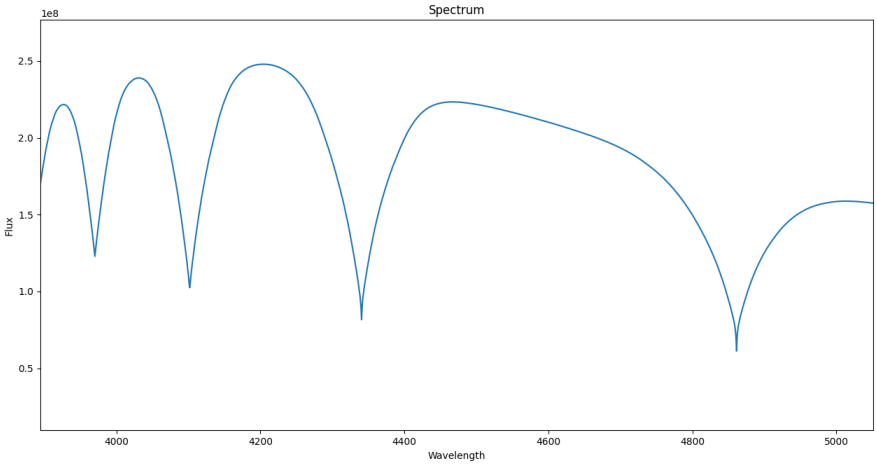

(A) Spectrum without Zeeman-effect ($T_{\text{eff}} = 14000\,\text{K}$, $\log g = 8.25$)

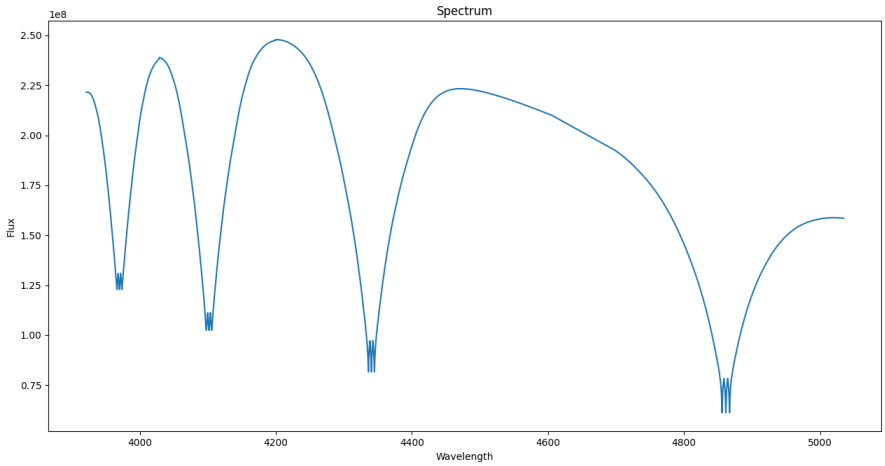

(B) Spectrum with Zeeman-effect due to $B_{\text{s}} = 500\,\text{KG}$.

FIGURE 2.17: Showcasing the differences between two spectra where one is under the effects of a magnetic field.

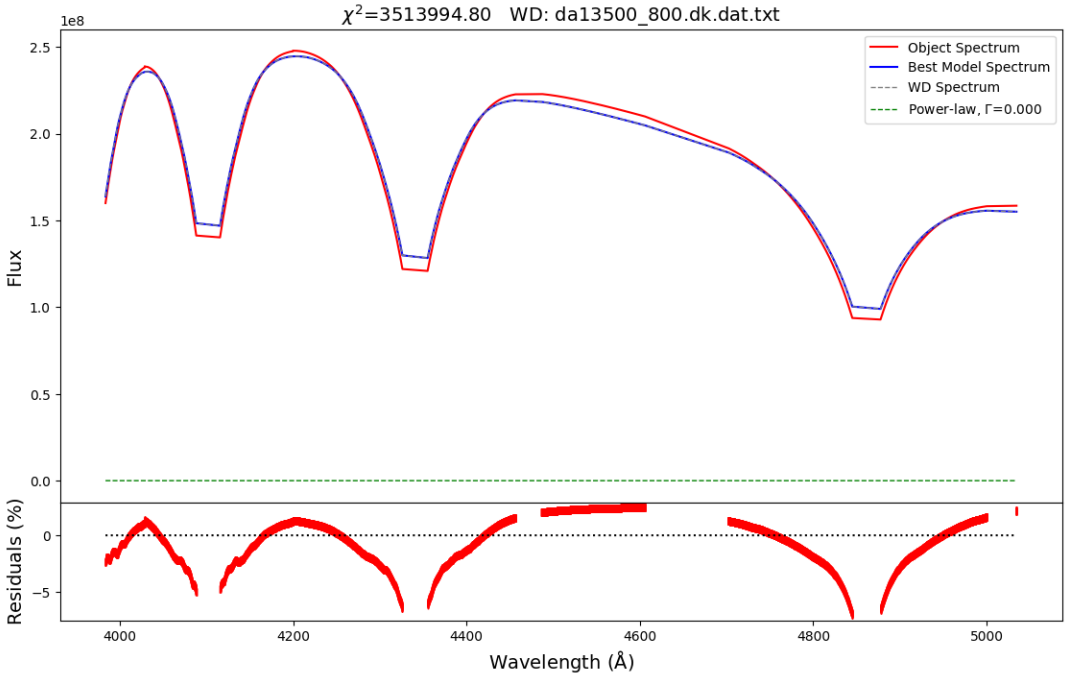

(A) The best fit to a model spectrum with Zeeman-effect ($B_s = 500\,\mathrm{KG}$).

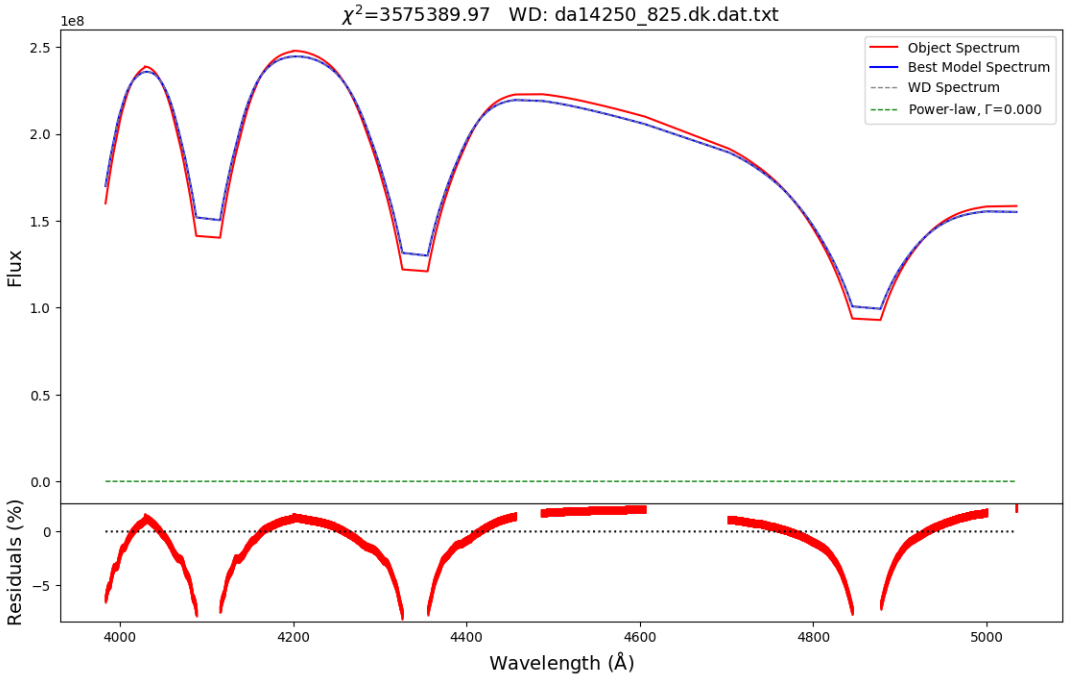

(B) The best fit to a model spectrum with Zeeman-effect($B_s = 500\,\mathrm{KG}$), only T_{eff} allowed to vary.

FIGURE 2.18: Best fits to a model spectrum with Zeeman-effect. Lines cut on both spectra according to $v_r = 1000\,\mathrm{km/s}$.

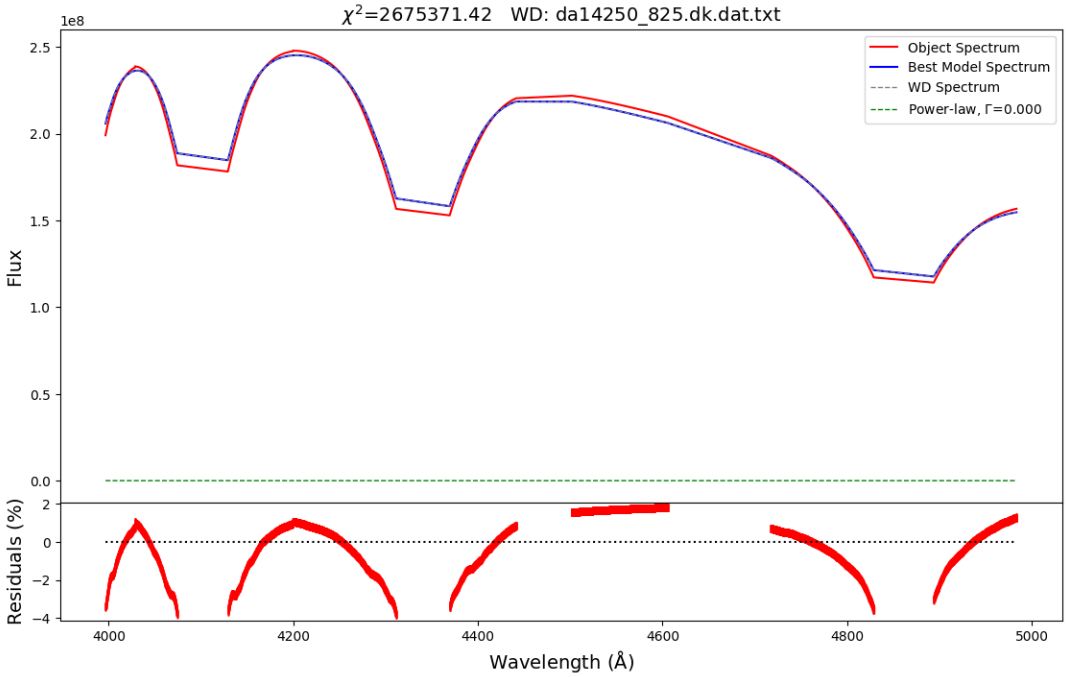

(A) The best fit to a model spectrum with Zeeman-effect ($B_s = 500\,\mathrm{KG}$).

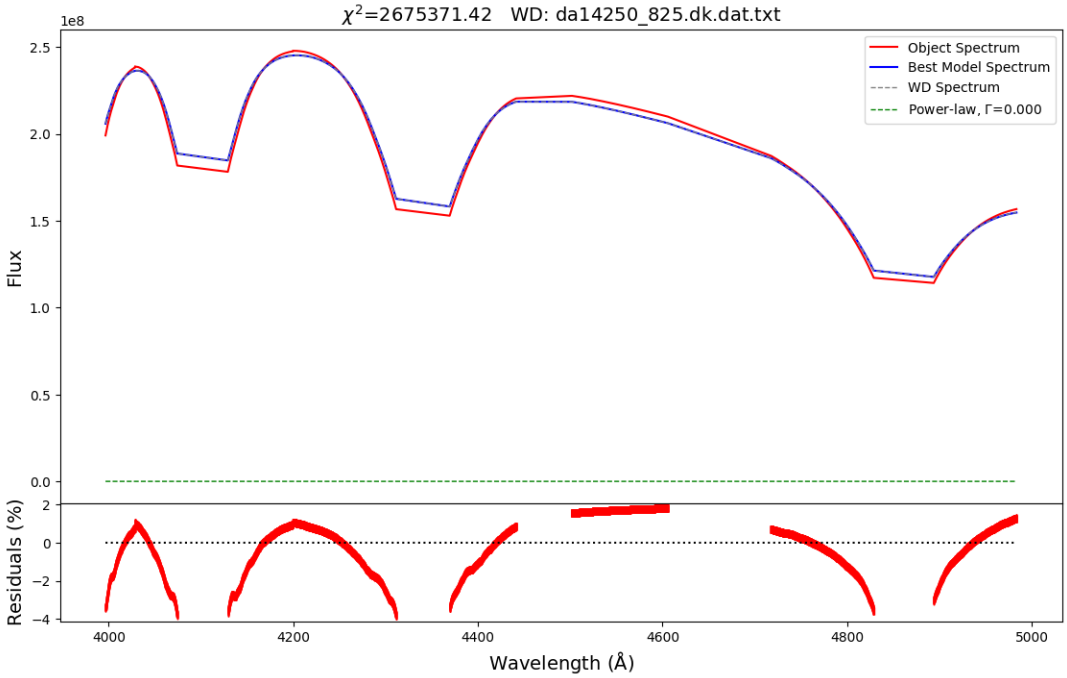

(B) The best fit to a model spectrum with Zeeman-effect($B_s = 500\,\mathrm{KG}$), only T_{eff} allowed to vary.

FIGURE 2.19: Best fits to a model spectrum with Zeeman-effect. Lines cut on both spectra according to $v_r = 2000\,\mathrm{km/s}$.

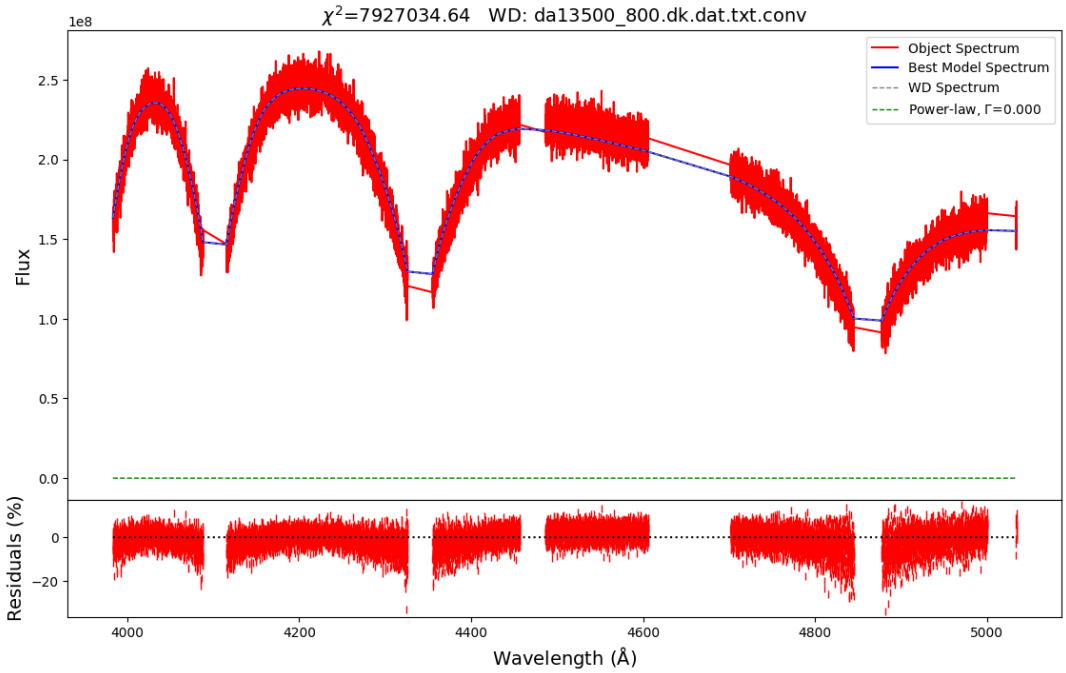

(A) The best fit to a model spectrum with Zeeman-effect ($B_s = 500\,\mathrm{KG}$), lines cut according to $v_r = 1000\,\mathrm{km/s}$ and noise applied such that S/N=30.

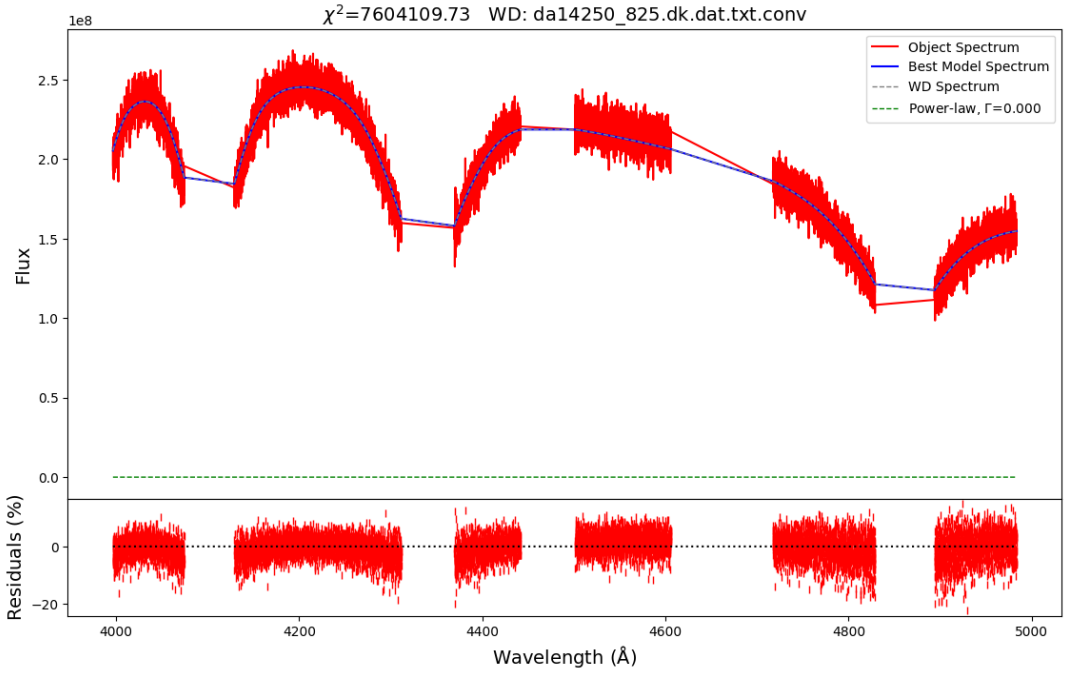

(B) The best fit to a model spectrum with Zeeman-effect($B_s = 500\,\mathrm{KG}$), lines cut according to $v_r = 2000\,\mathrm{km/s}$ and noise applied such that S/N=30.

FIGURE 2.20: Best fits to model spectra with Zeeman-effect, lines cut and noise applied.

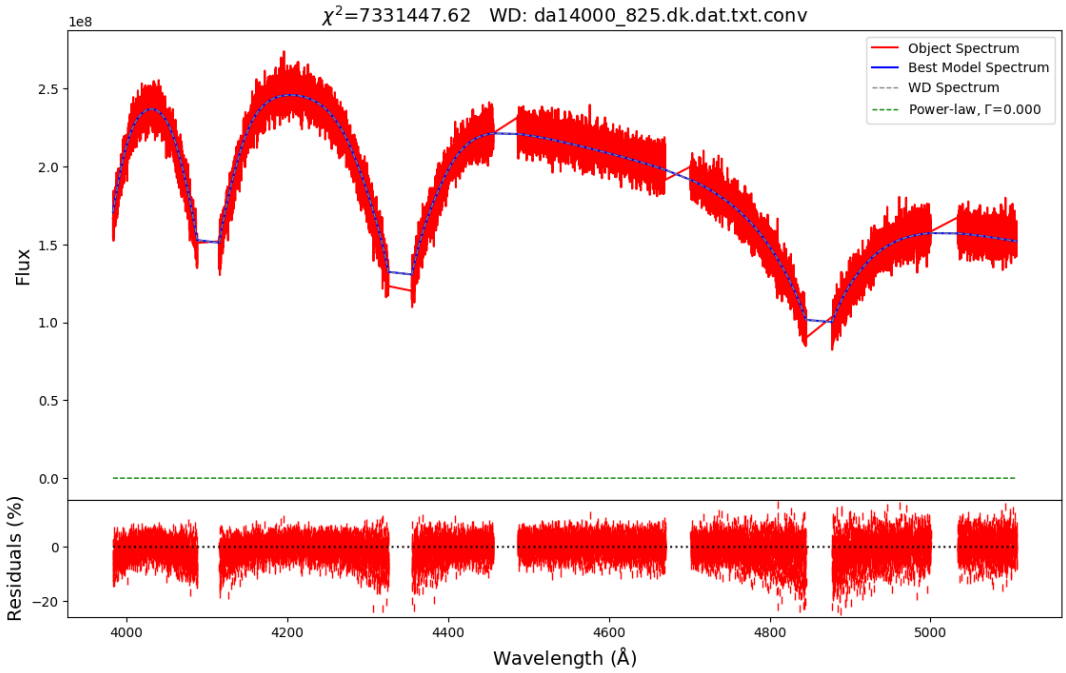

(A) The best fit to a model spectrum with Zeeman-effect ($B_s = 300\,\mathrm{KG}$), lines cut according to $v_r = 1000\,\mathrm{km/s}$ and noise applied such that S/N=30.

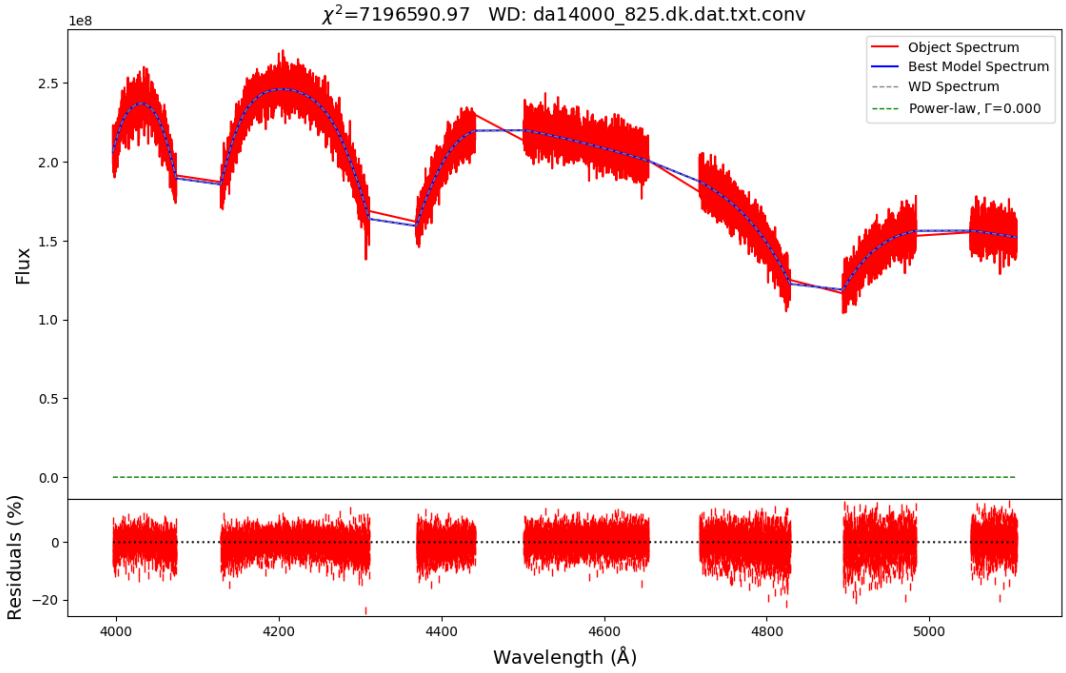

(B) The best fit to a model spectrum with Zeeman-effect($B_s = 300\,\mathrm{KG}$), lines cut according to $v_r = 2000\,\mathrm{km/s}$ and noise applied such that S/N=30.

FIGURE 2.21: Best fits model spectra with Zeeman-effect, lines cut and noise applied.

Chapter 3

Modelling real objects

3.1 Modelling cataclysmic variables

3.1.1 Modelling objects with comparison available

We chose four CV stars studied by Pala et al. [13] to measure $T_{\rm eff}$ using optical spectra. We were limited to four objects by only using the SDSS database. We compare our results with those obtained by Pala et al. [13], but we cannot make a direct comparison, as i.e. the observation dates differ. Nonetheless, a stark difference in the obtained parameter value could indicate that something is amiss. The objects are shown in Table 3.1.

As stated earlier, the average surface gravity is $\log g = 8.35$ (Wijnen et al. [19]), so for all our modelling we assume this value (there is one exception, see below). Thus, we use our modelling method to find $T_{\rm eff}$ for $\log g = 8.35$. The resulting best fits are shown below in figures 3.1-3.3, and the results are also shown in Table 3.2. Unlike for our other objects, for SDSS J123813.73-033932.9 we assumed $\log g = 8.50$. This object has been studied in more detail by e.g Pala et al. [21], where they found the mass to be higher than the average WD mass in CV's.

As can be seen, our results are generally consistent with those obtained by Pala et al. [13]. A superoutburst in RZ Leo was observed in December of 2000 (Ishioka et al. [22]). Our first spectrum of RZ Leo was taken in March of 2001. During an outburst (and superoutburst) the effective temperature is higher than in quiescence. Thus, we can attribute our higher obtained $T_{\rm eff}$ to the superoutburst. Two other spectra of RZ Leo were taken within 10 days of each other, in March 2011, by different telescopes. These spectra are not affected by the superoutburst, so tbe obtained $T_{\rm eff}$ is lower.

TABLE 3.1: Objects taken from the paper by Pala et al. [13].

Object name	$T_{\rm eff}$**[K]**	**Distance[pc]**	**Obs. date[dd.mm.yyyy]**
RZ Leo	15014	281	11.04.2013
GW Lib	16995	113	30.05.2013
SDSS J143544.02+233638.7	11940	208	09.03.2013
SDSS J123813.73-033932.9	18358$\pm$912	170	01.03.2013

TABLE 3.2: Obtained T_{eff} for four objects taken from the paper by Pala et al. [13].

Object name	**Obtained T_{eff}[K]**	**Cut velocity[km/s]**	**Obs. date[dd.mm.yyyy]**
RZ Leo (SDSS)	17250	3300	21.03.2001
RZ Leo (SDSS)	13250	3300	31.03.2011
RZ Leo (X-shooter)	13750	3000	21.03.2011
GW Lib	14750	2500	-
SDSS J143544.02+233638.7	13000	2000	04.05.2005
SDSS J123813.73-033932.9	15000	2500	03.03.2000

GW Lib was one of the objects studied by Townsley and Gänsicke [14]. They obtained a $T_{\text{eff}} = 14700\,\text{K}$, which is almost identical to our result of $T_{\text{eff}} = 14750\,\text{K}$. The temperature obtained by Pala et al. [13] is marked as an upper limit temperature, so considering all these we find our result to be plausible.

For SDSS J1238-03 the comparison parameters are $T_{\text{eff}} = 18358\,\text{K} \pm 912\,\text{K}$ and $\log g = 8.35$. We obtained, using $\log g = 8.50$ an effective temperature of $T_{\text{eff}} = 15000\,\text{K}$. In the paper by Pala et al. [21], the underlying quiescence effective temperature chosen for their modelling purposes was $T_{\text{eff}} = 14000\,\text{K}$. Comparing to this value, we are within an acceptable margin, as shown in Chapter 2.

Lastly, for SDSS J1435+23, we are again reasonably close ($\Delta T_{\text{eff}} \sim 1000\,\text{K}$) to the comparison value.

3.1.2 Modelling objects without comparison

In addition to the objects for which parameters resulting from modelling can be compared to earlier results, we also modelled spectra without reference T_{eff} and $\log g$. For these objects, we show the obtained T_{eff}. As before, we assume $\log g = 8.35$. The results can be seen in figures 3.4-3.10 and in Table 3.3. For all objects we used the distances obtained from *Gaia* database to constrain the flux of the WD. This allows a more precise measurement of the parameters.

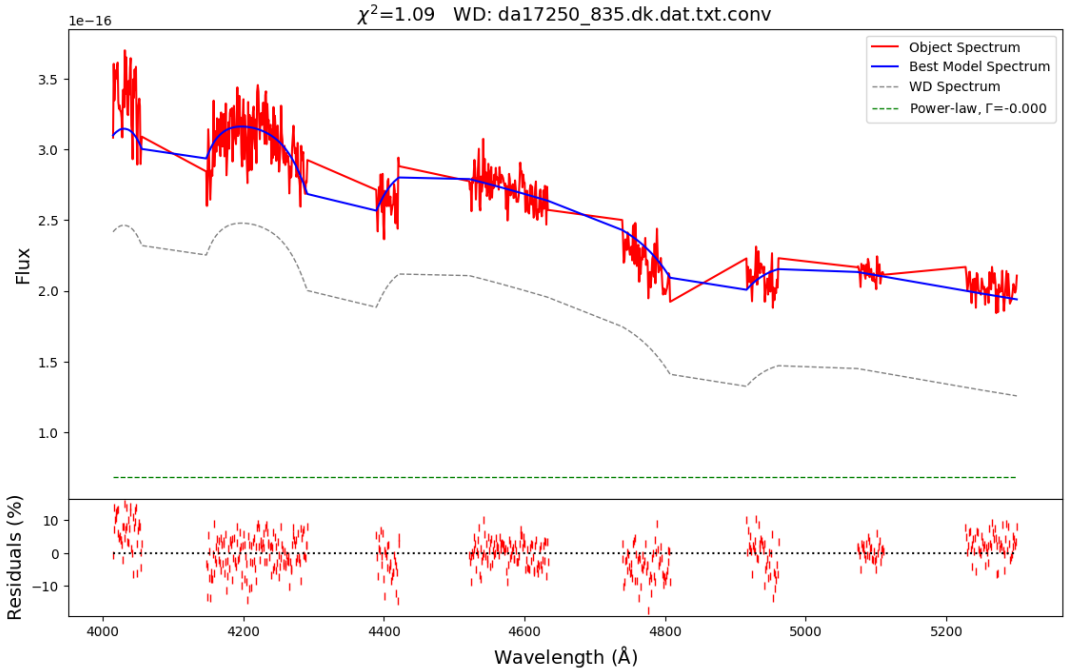

(A) The best fit to a spectrum of RZ Leo.

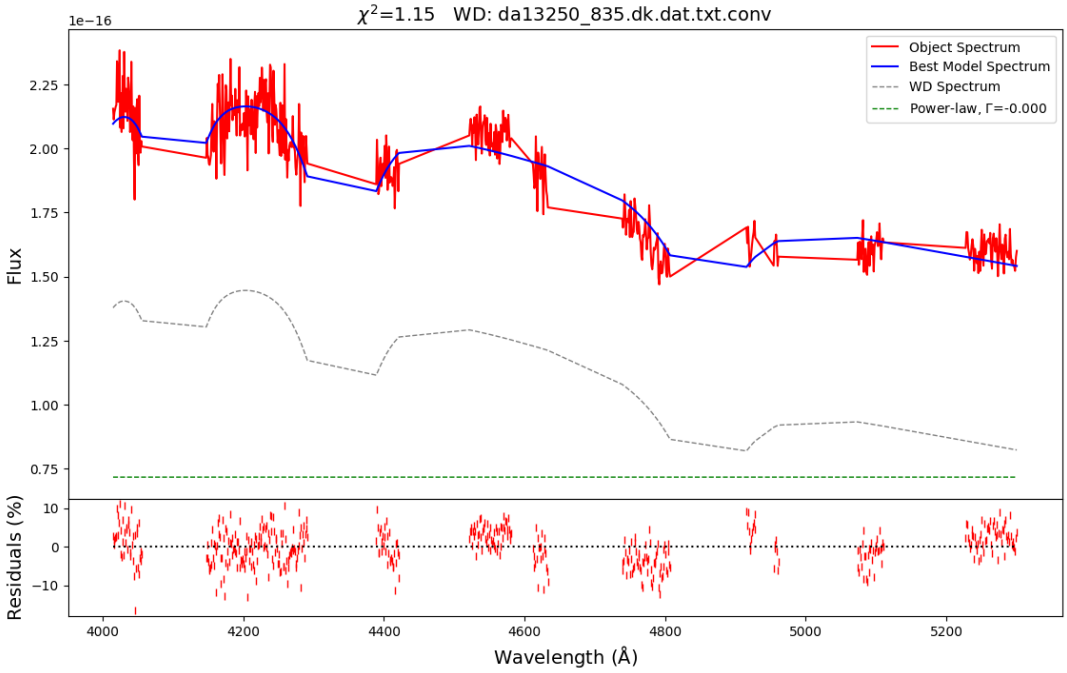

(B) The best fit to a spectrum of RZ Leo.

FIGURE 3.1: The best fits to two spectra of RZ Leo, taken from the SDSS ctalogue, observed at different times.

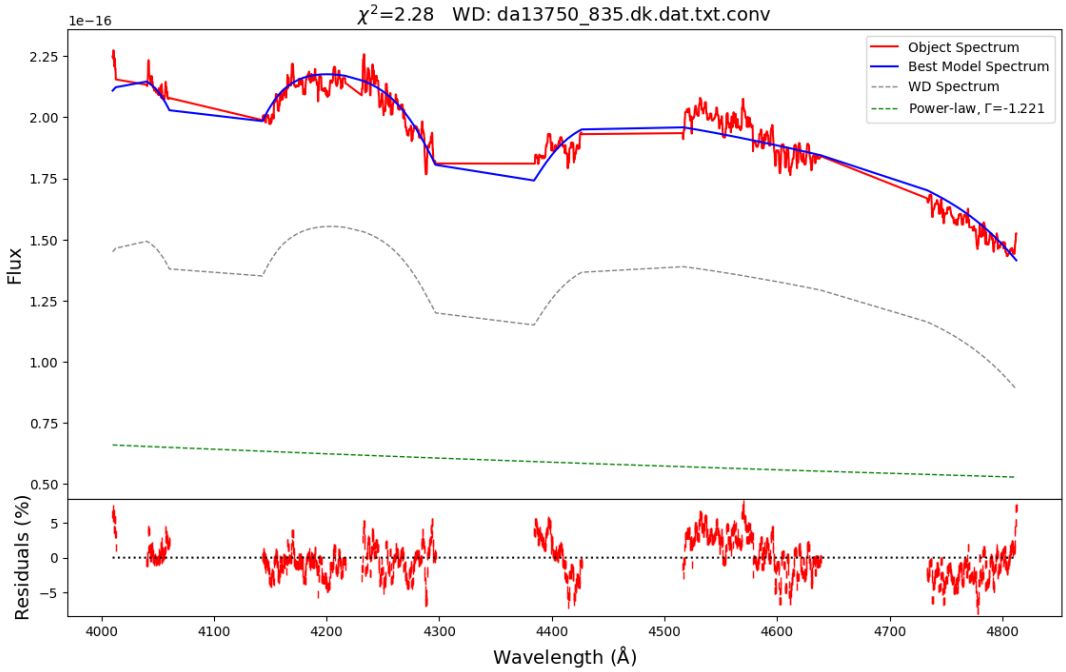

(A) The best fit to a spectrum of RZ Leo.

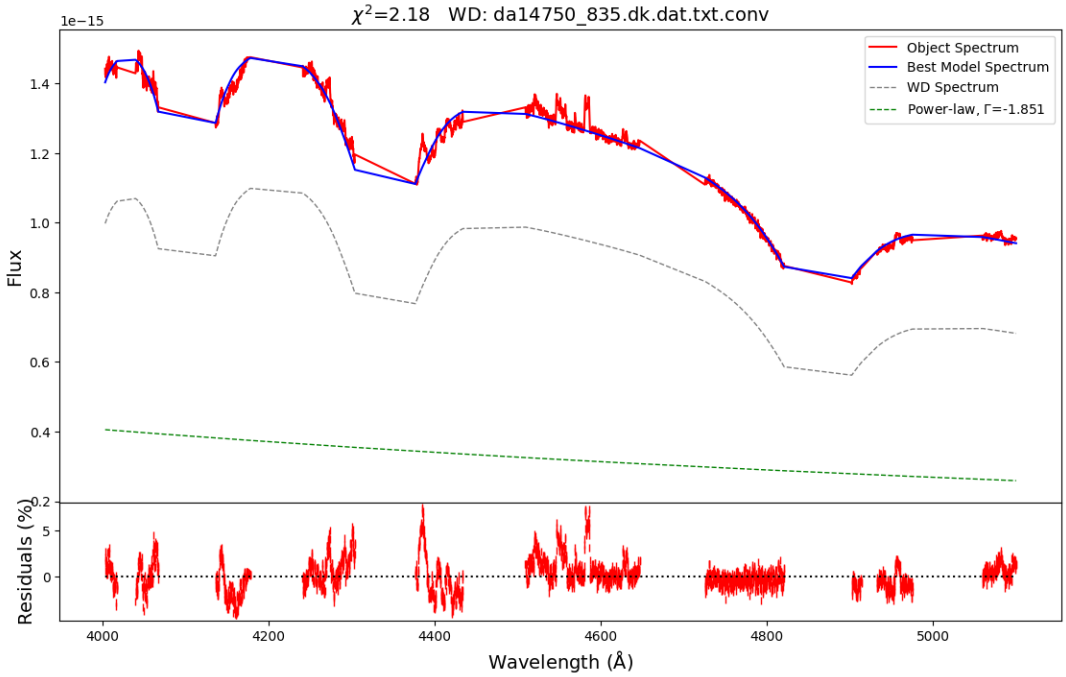

(B) The best fit to the spectrum of GW Lib.

FIGURE 3.2: The best fits to spectra of RZ Leo and GW Lib, both observed by XShooter.

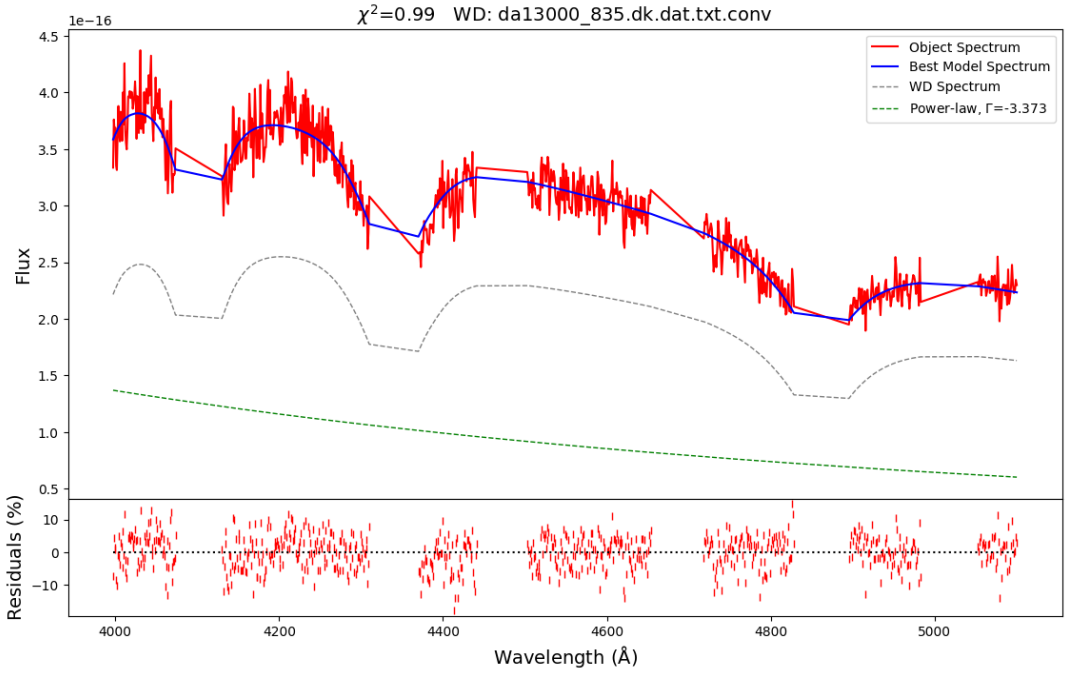

(A) The best fit to the spectrum of SDSS J143544.02+233638.7.

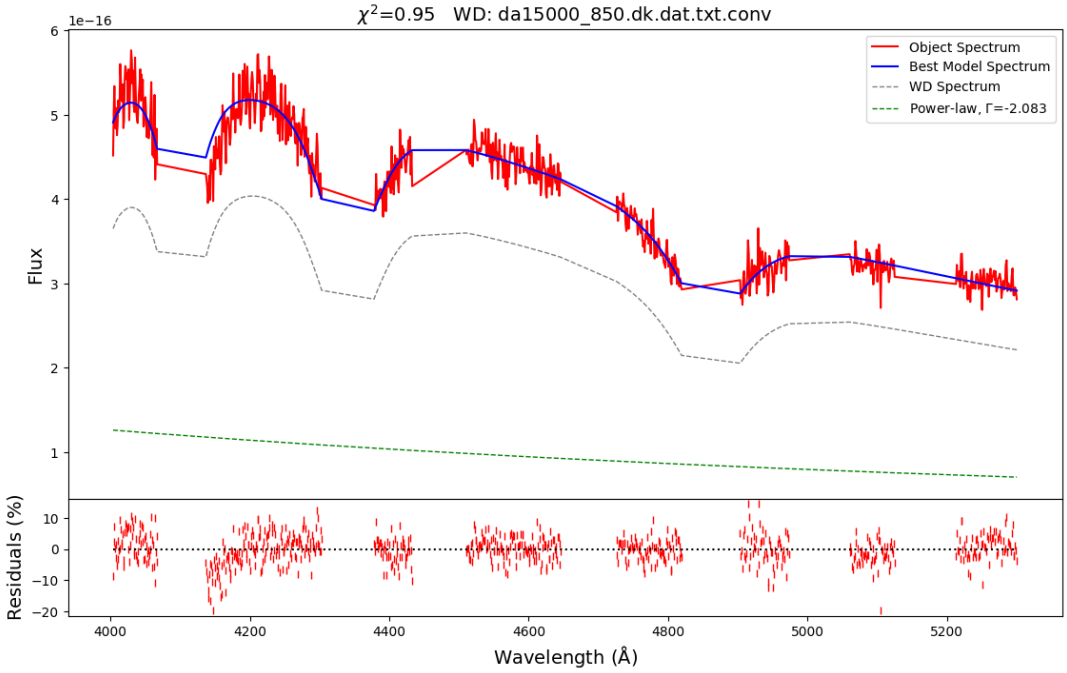

(B) The best fit to the spectrum of SDSS J123813.73-033932.9.

FIGURE 3.3: The best fits to spectra of SDSS J143533.02+233638.7 and SDSS J123813.73-033932.9, spectra taken from the SDSS catalogue.

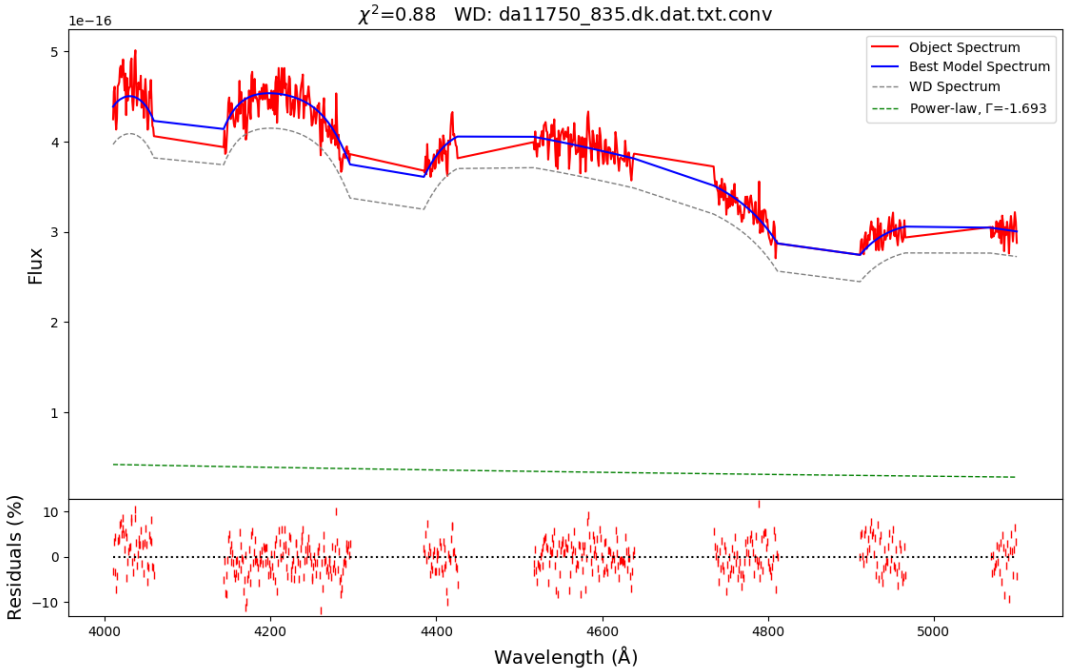

(A) The best fit to a spectrum of EZ Lyn.

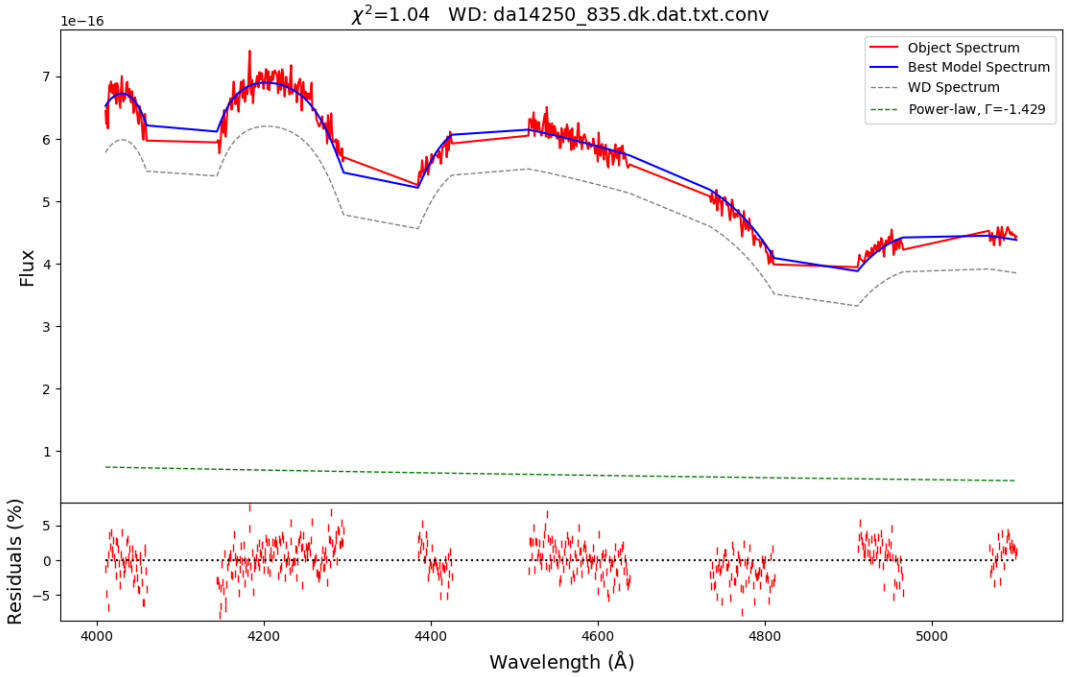

(B) The best fit to a spectrum of EZ Lyn.

FIGURE 3.4: The best fits to two spectra of EZ Lyn. Each spectrum was cut using $v_{r,ac} = 3000\,\mathrm{km/s}$ as well as cross-corrected.

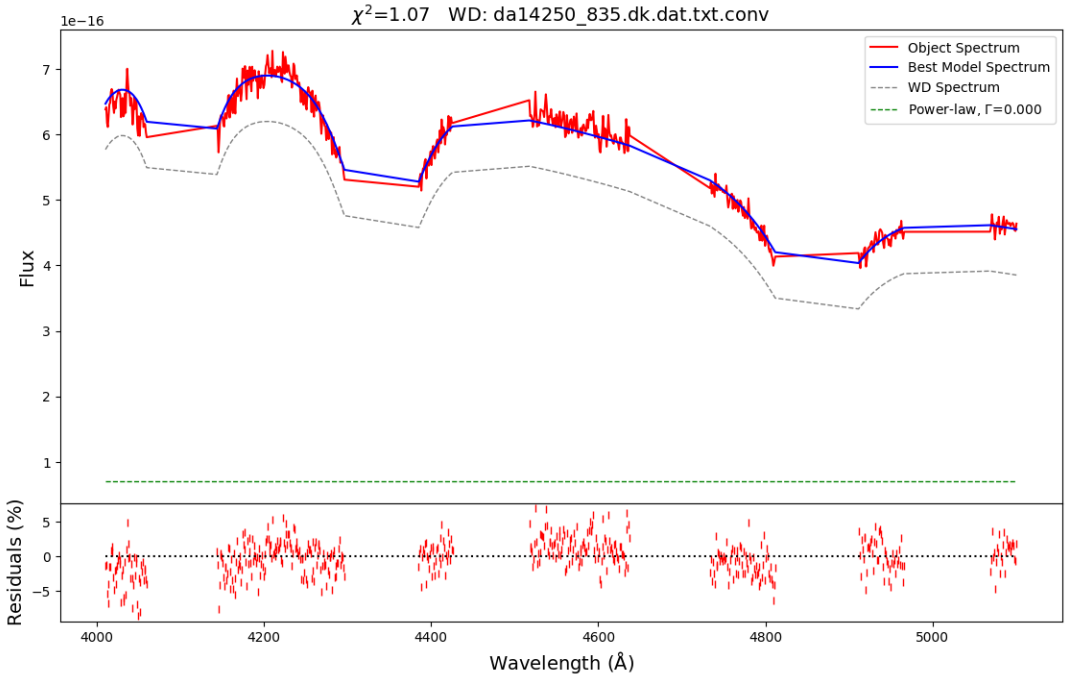

(A) The best fit to a spectrum of EZ Lyn.

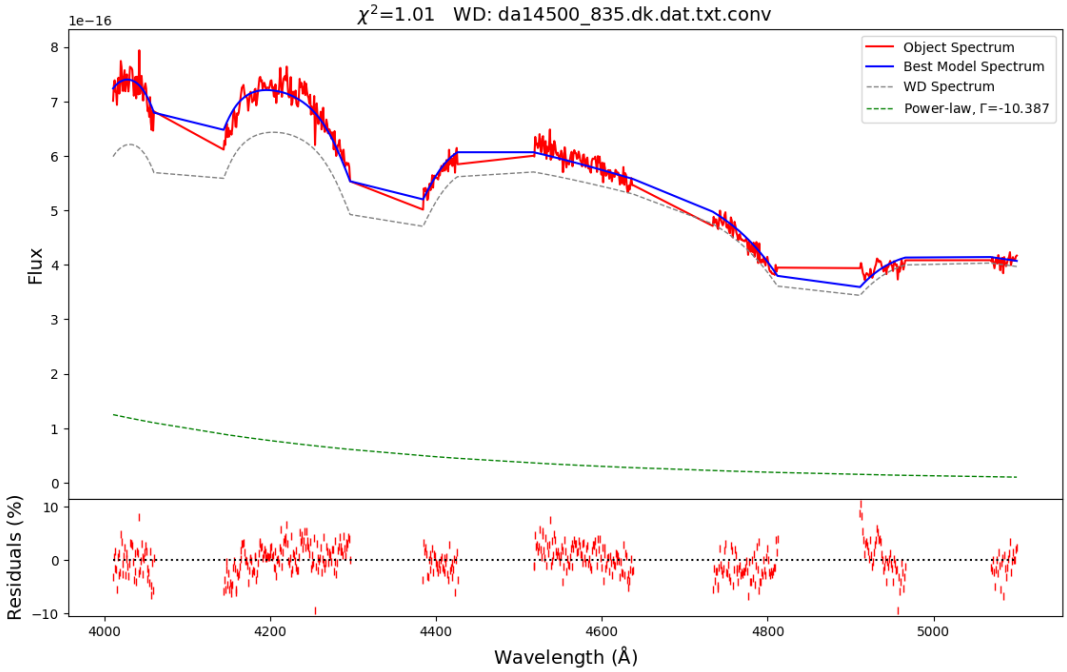

(B) The best fit to a spectrum of EZ Lyn.

FIGURE 3.5: The best fits to two spectra of EZ Lyn. Each spectrum was cut according to $v_{\mathrm{r,ac}} = 3000\,\mathrm{km/s}$ as well as cross-corrected.

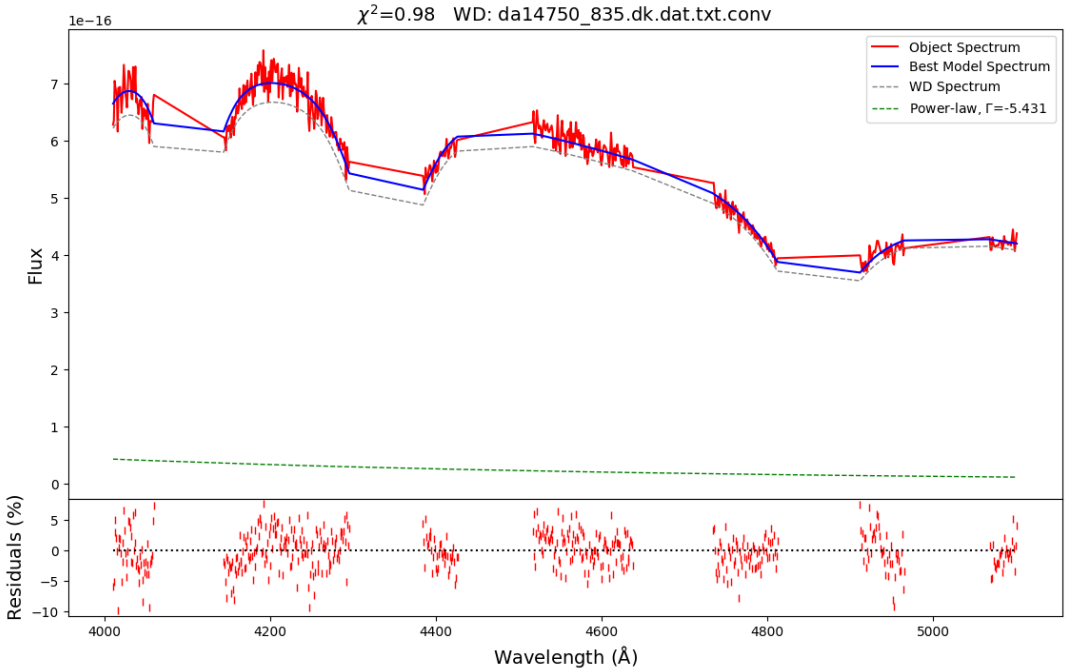

(A) The best fit to a spectrum of EZ Lyn.

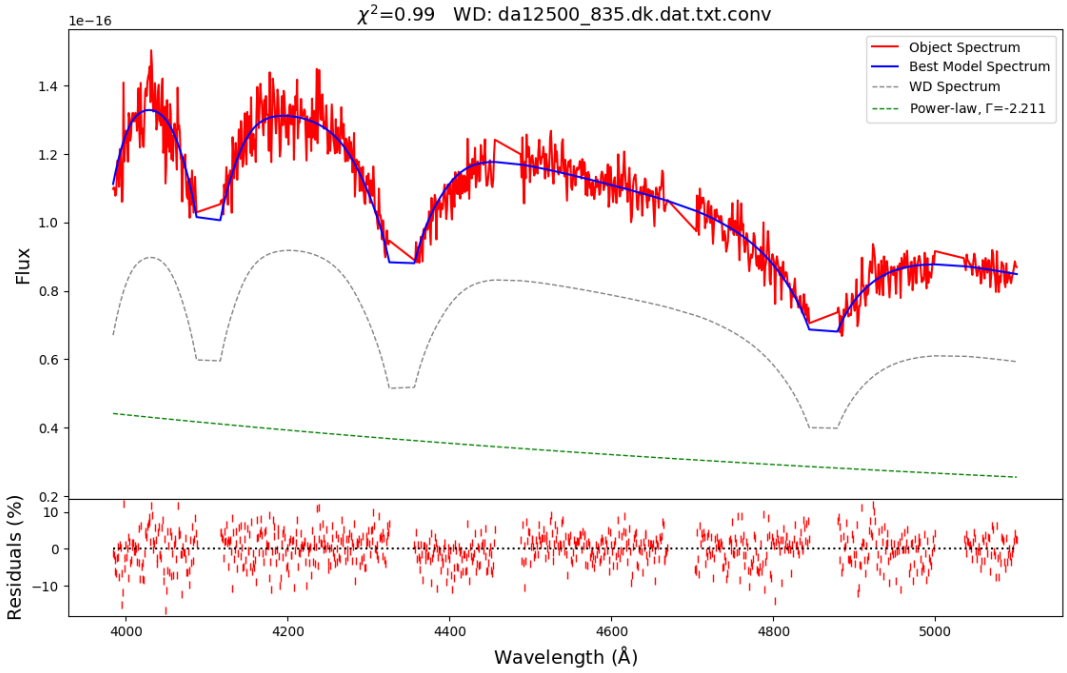

(B) The best fit to the spectrum of MT Com.

FIGURE 3.6: The best fits to spectra of EZ Lyn and MT Com. Spectrum of EZ Lyn was cut according to $v_{\mathrm{r,ac}} = 3000\,\mathrm{km/s}$, and MT Com according to $v_{\mathrm{r,ac}} = 1000\,\mathrm{km/s}$. Both were also cross-corrected.

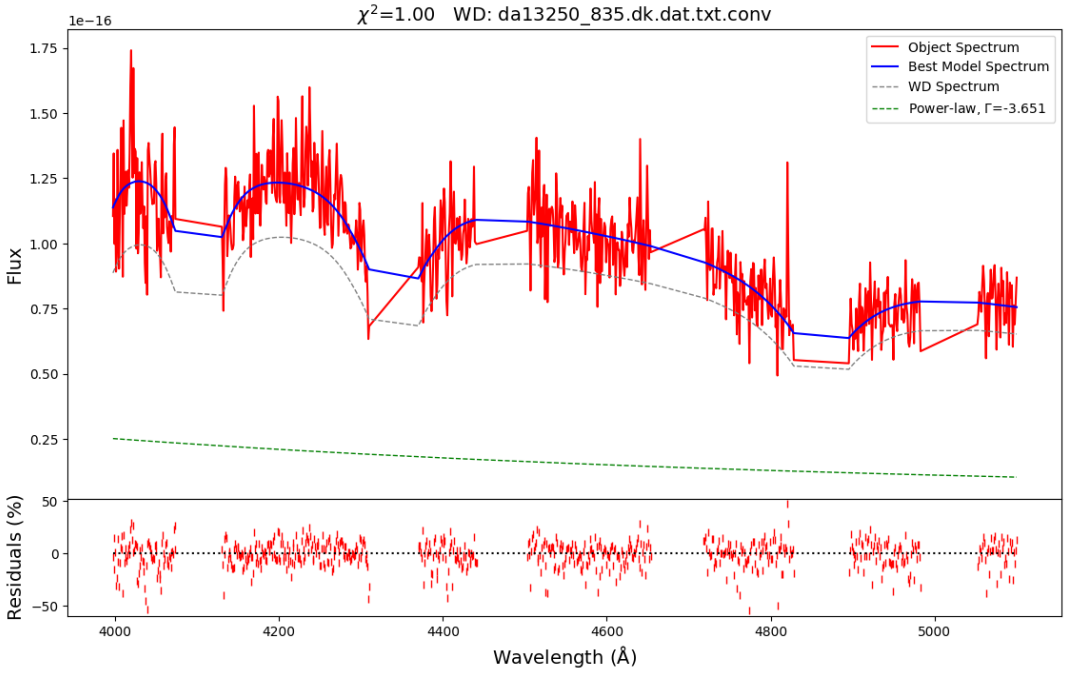

(A) The best fit to the spectrum of SDSS J090452.09+440255.4.

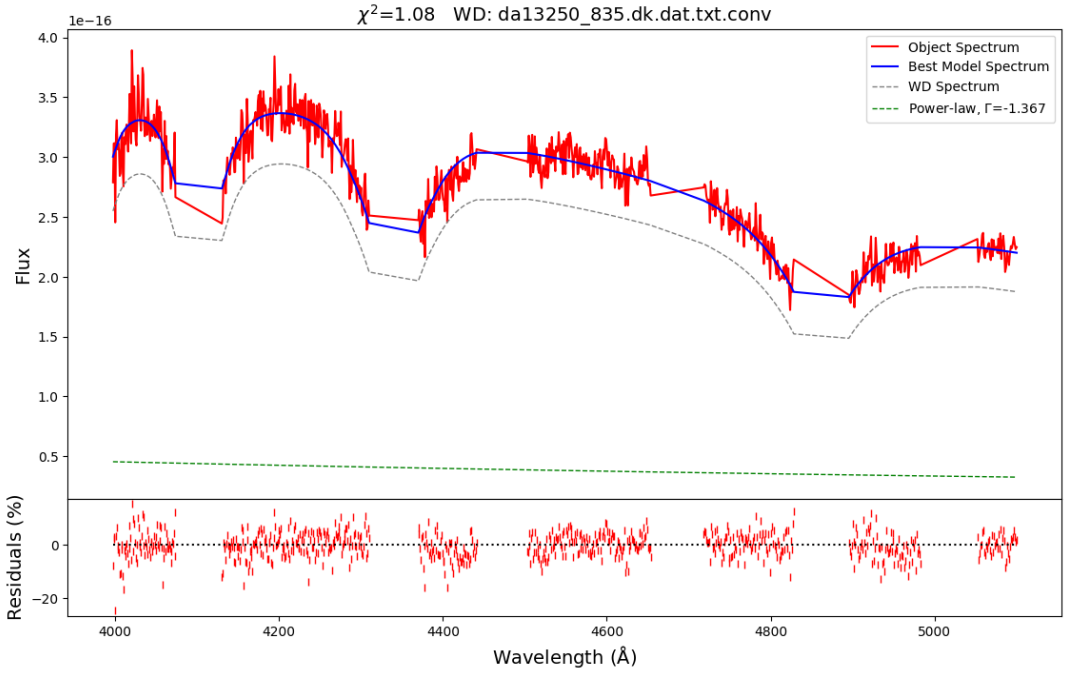

(B) The best fit to the spectrum of SDSS J091945.11+085710.0.

FIGURE 3.7: The best fits to spectra of SDSS J090452.09+440255.4 and SDSS J091945.11+085710.0. Both spectra were cut according to $v_{\mathrm{r,ac}} = 2000\,\mathrm{km/s}$.

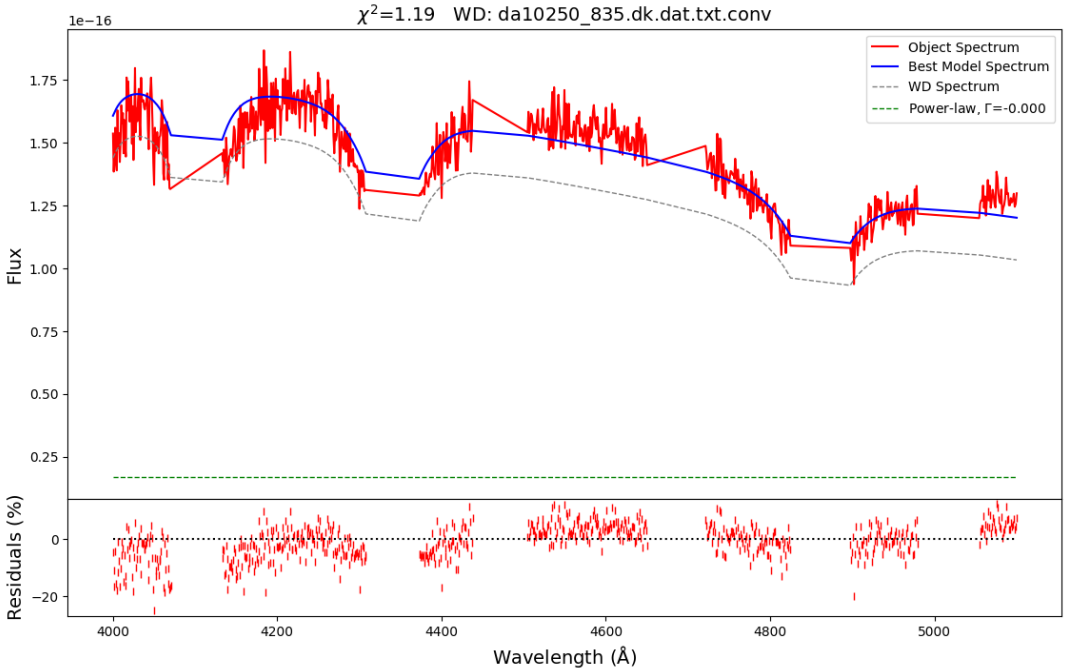

(A) The best fit to the spectrum of SDSS J103533.02+055158.4.

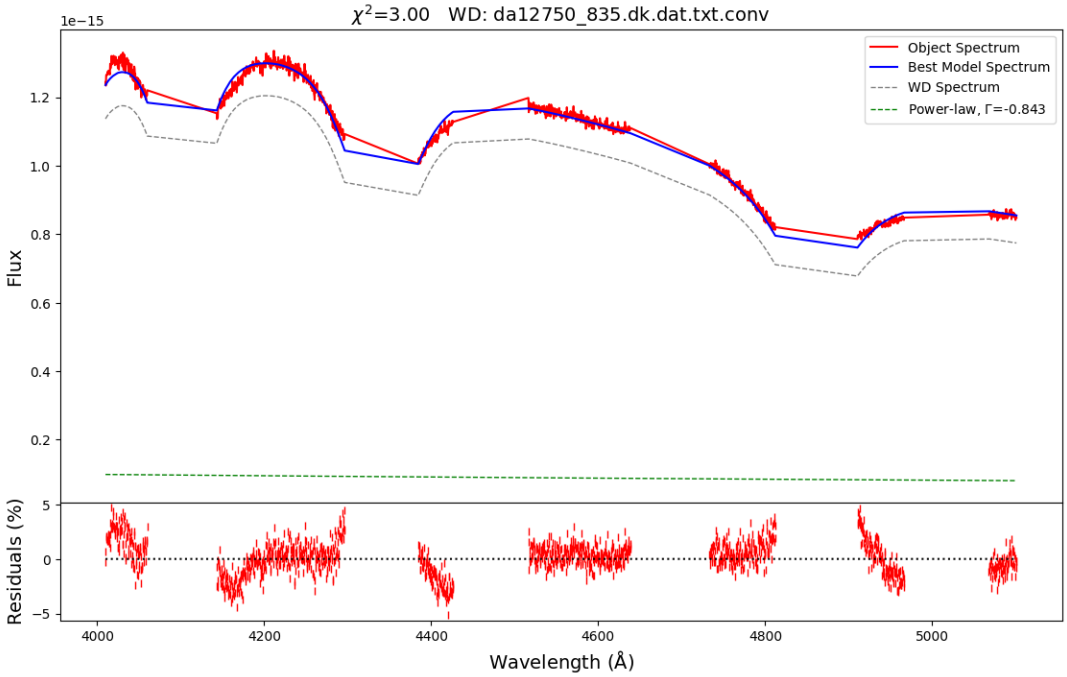

(B) The best fit to a spectrum of BW Scl (SDSS).

FIGURE 3.8: The best fits to spectra of SDSS J103533.02+055158.4 and BW Scl. Spectra were cut according to $v_{\mathrm{r,ac}} = 2200\,\mathrm{km/s}$, and $v_{\mathrm{r,ac}} = 30000\,\mathrm{km/s}$, respectively.

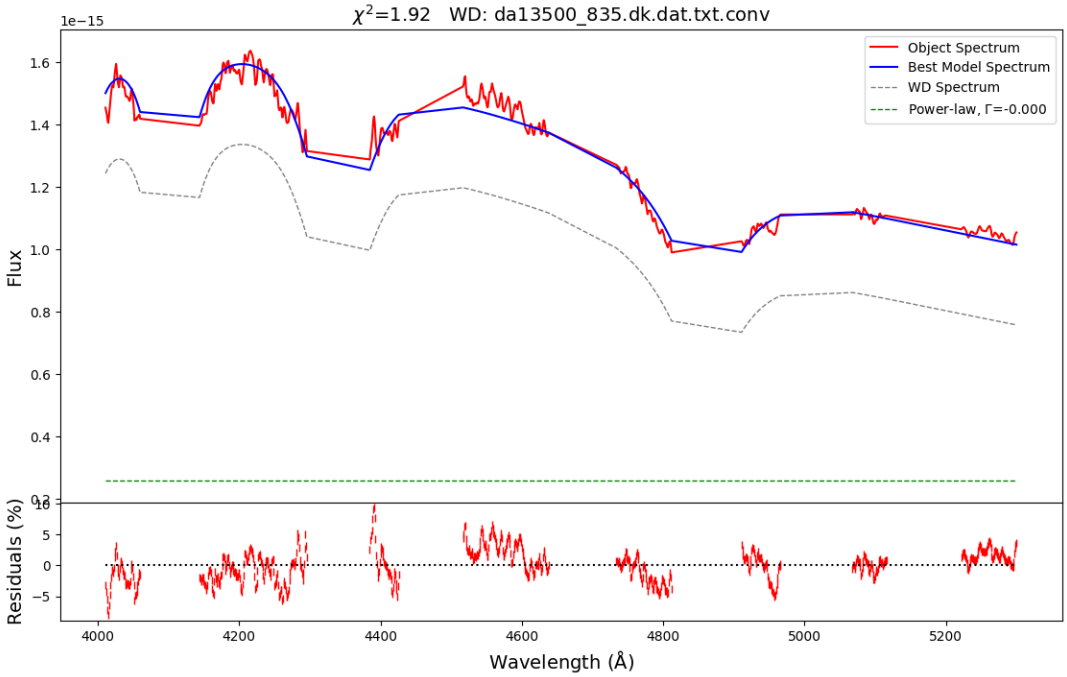

(A) The best fit to a spectrum of BW Scl (efosc).

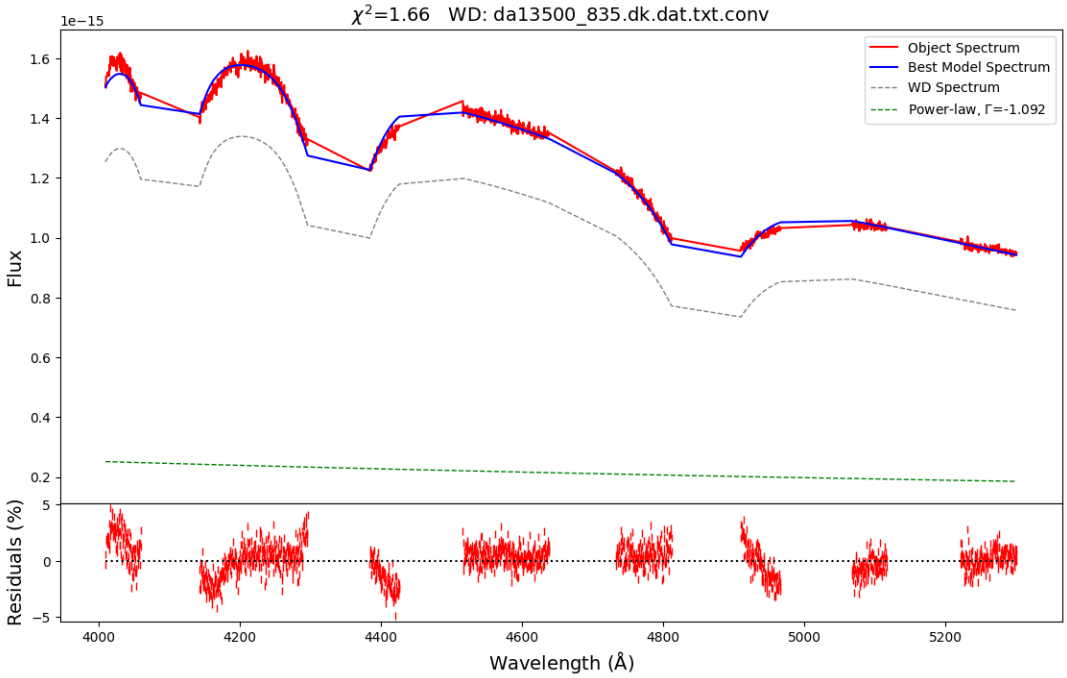

(B) The best fit to a spectrum of BW Scl (XShooter).

FIGURE 3.9: The best fits to two spectra of BW Scl, both cut according to $v_{\mathrm{r,ac}} = 3000\,\mathrm{km/s}$.

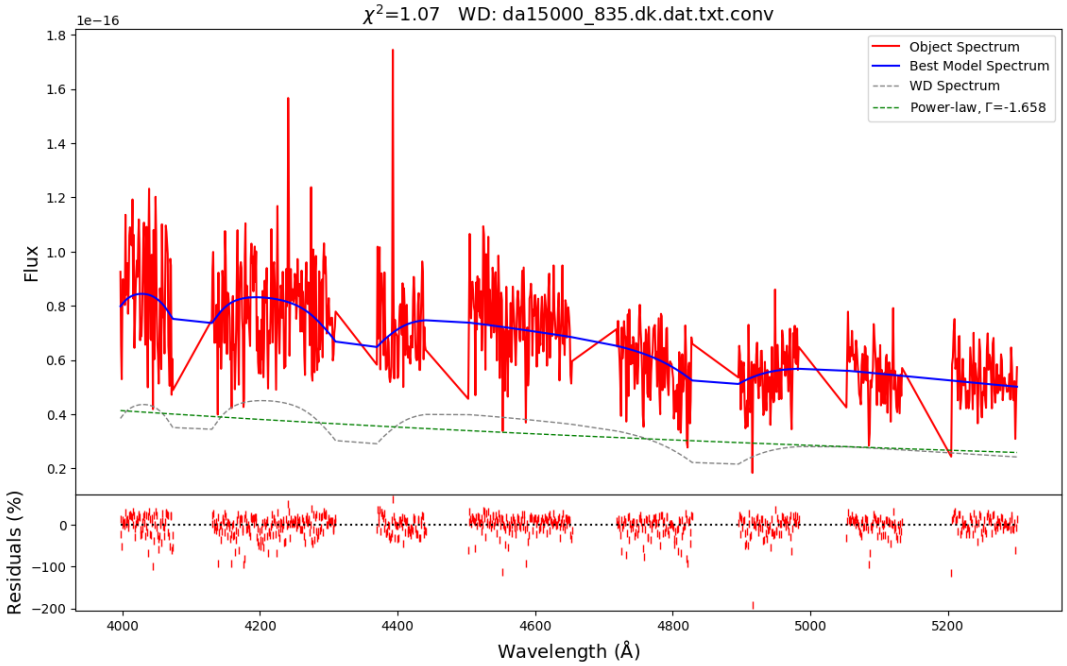

(A) The best fit to a spectrum of SDSS J145758.21+514807.9.

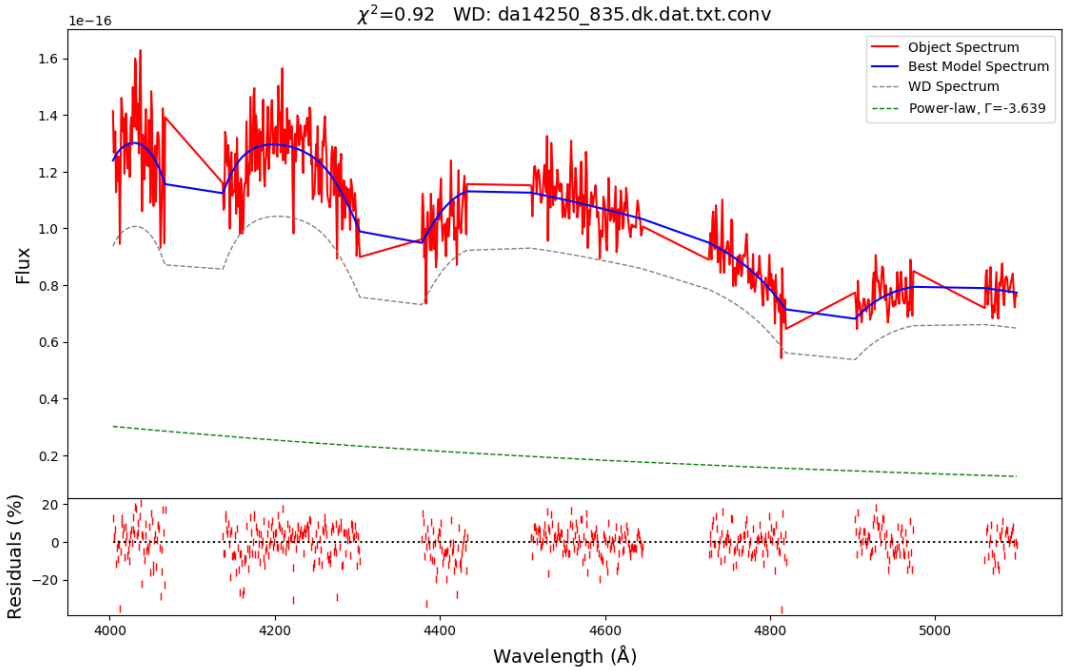

(B) The best fit to a spectrum of SDSS J145758.21+514807.9.

FIGURE 3.10: The best fits to two spectra of SDSS J145758.21+514807.9, cut according to $v_{\mathrm{r,ac}} = 2000\,\mathrm{km/s}$, and $v_{\mathrm{r,ac}} = 2500\,\mathrm{km/s}$, respectively.

TABLE 3.3: Obtained $T_{\rm eff}$ from modelling additional cataclysmic variables, no reference parameters.

Object name	**Obtained $T_{\rm eff}$[K]**	**Distance[pc]**	**Cut velocity[km/s]**
EZ Lyn (1)	11750	146	3000
EZ Lyn (2)	14250	146	3000
EZ Lyn (3)	15250	146	3000
EZ Lyn (4)	14500	146	3000
EZ Lyn (5)	14750	146	3000
MT Com	12500	340	1000
SDSS J090452.09+440255.4	13250	334	2000
SDSS J091945.11+085710.0	13250	197	2000
SDSS J103533.02+055158.4	10250	195	2200
BW Scl (SDSS)	12750	94	3000
BW Scl (efosc)	13500	94	3000
BW Scl (X-shooter)	13500	94	3000
SDSS J145758.21+514807.9 (1)	15000	572	2000
SDSS J145758.21+514807.9 (2)	14250	572	2500

Chapter 4

Average properties of accretion discs

4.1 Accretion disc spectra

In Chapter 3, the best fitting models to the objects were shown. Using these models, we extracted from each observed spectrum the contribution of the WD out. As these systems are relatively cool and in quiescence, the spectrum that is left shows the contribution of the accretion disc. For a couple of objects, the infrared part of the spectrum can be contaminated by the companion star. The accretion disc spectra can be seen in figures 4.1-4.10. The contamination by the companion star can especially be seen in fig. 4.10b.

Using the obtained accretion disc spectra, and the distances to these systems provided by *Gaia*, we estimated the luminosity of the disc. Furthermore, from the luminosities we obtained apparent and absolute magnitudes. We compared the obtained luminosity of each disc to the total luminosity of the system. The obtained values are shown in Table 4.1. We see that the contribution of the accretion disc to the total luminosity of the system ranges from 13 % to 78 %.

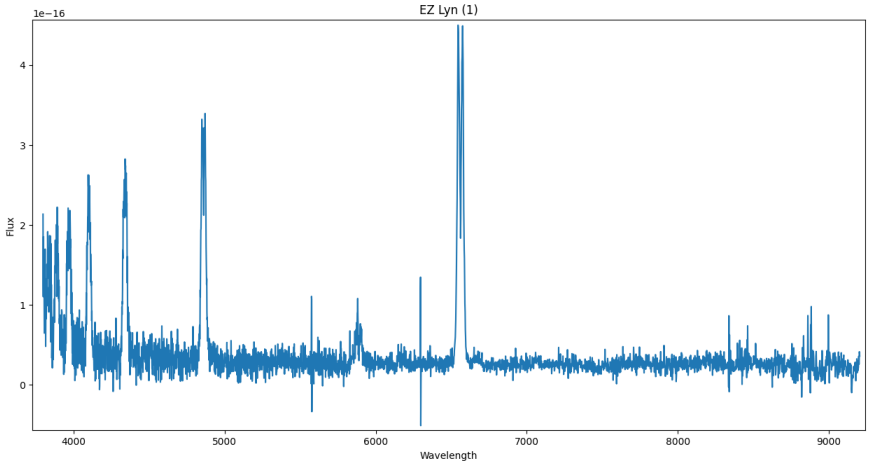

(A) The obtained accretion disc spectrum of EZ Lyn (1).

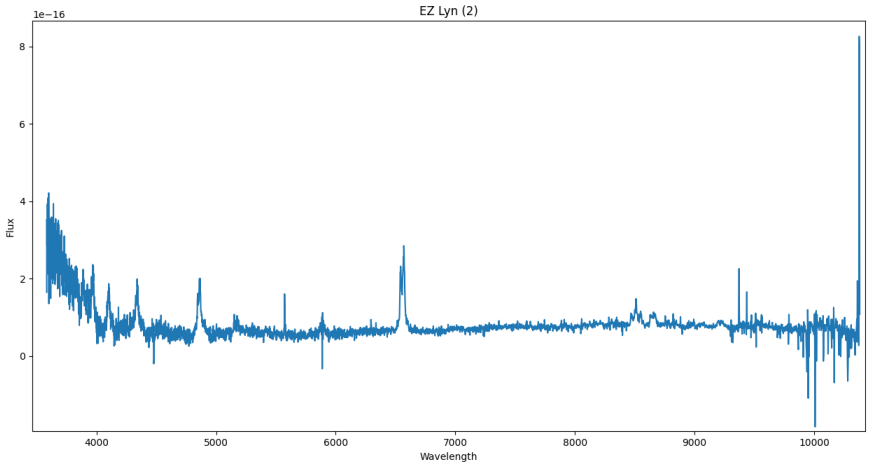

(B) The obtained accretion disc spectrum of EZ Lyn (2)

FIGURE 4.1: Accretion disc spectra obtained from two different spectra of EZ Lyn.

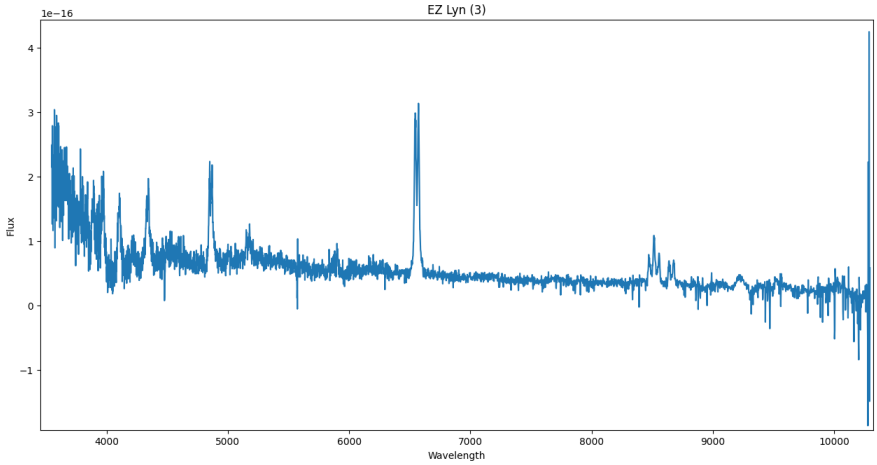

(A) The obtained accretion disc spectrum of EZ Lyn (3)

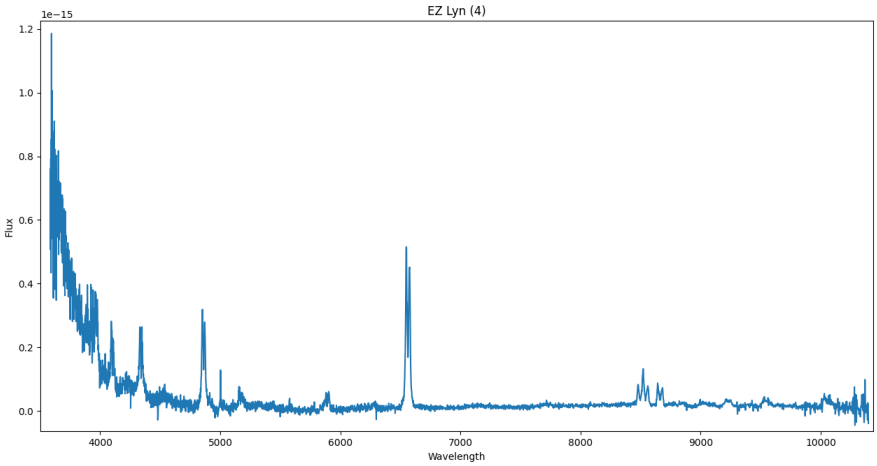

(B) The obtained accretion disc spectrum of EZ Lyn (4)

FIGURE 4.2: Accretion disc spectra obtained from two different spectra of EZ Lyn.

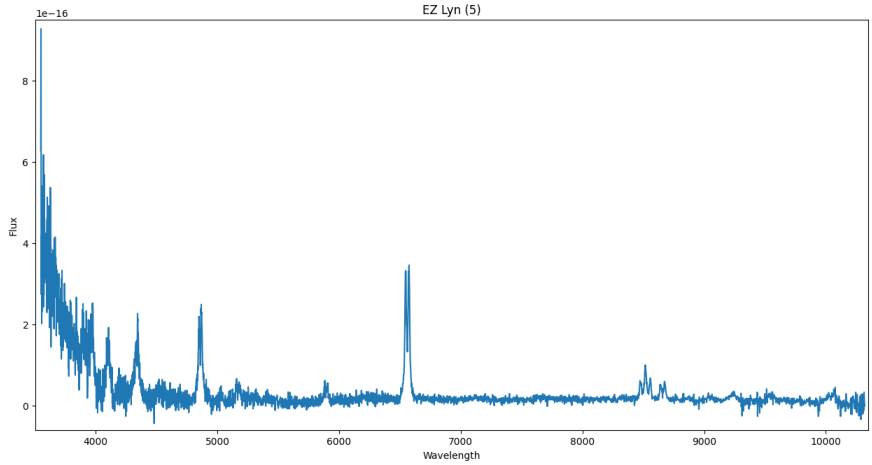

(A) The obtained accretion disc spectrum of EZ Lyn (5)

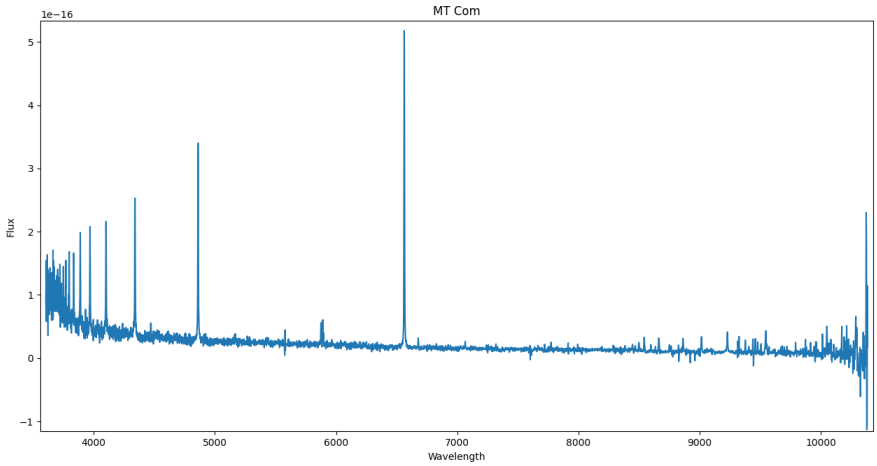

(B) The obtained accretion disc spectrum of MT Com

FIGURE 4.3: Accretion disc spectra obtained from the spectra of EZ Lyn (5) and MT Com.

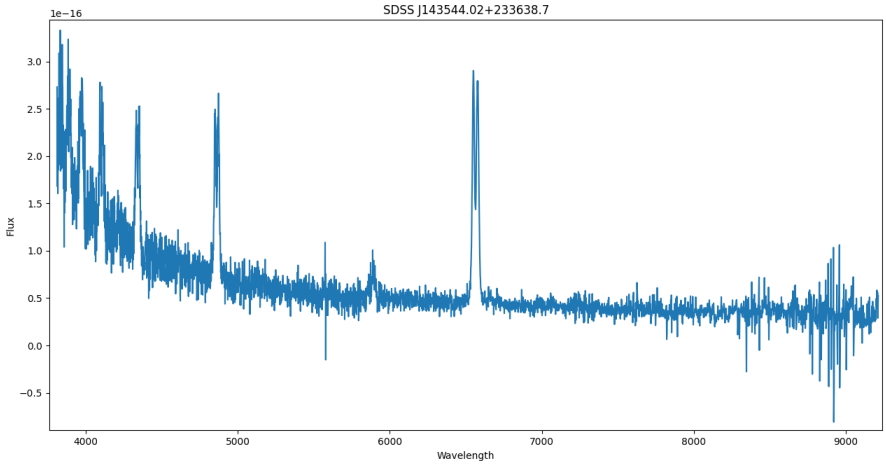

(A) The obtained accretion disc spectrum of SDSS J143544.02+233638.7.

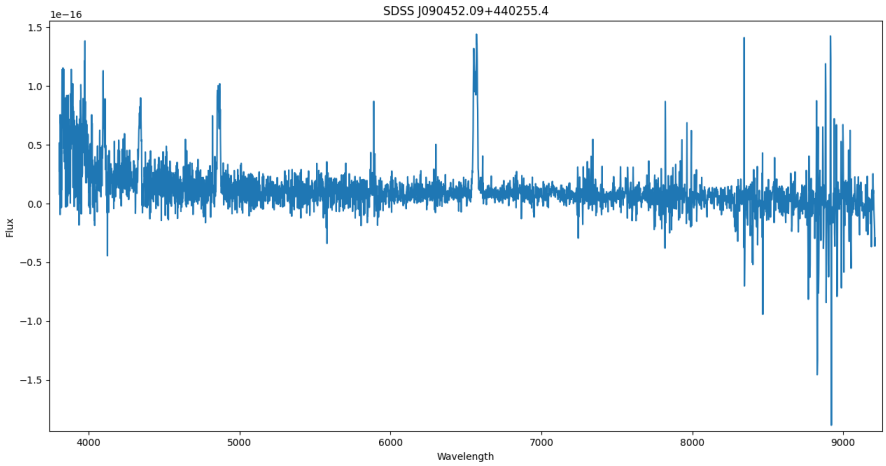

(B) The obtained accretion disc spectrum of SDSS J090452.09+440255.4.

FIGURE 4.4: Accretion disc spectra obtained from the spectra of SDSS J143544.02+233638.7 and SDSS J090452.09+440255.4.

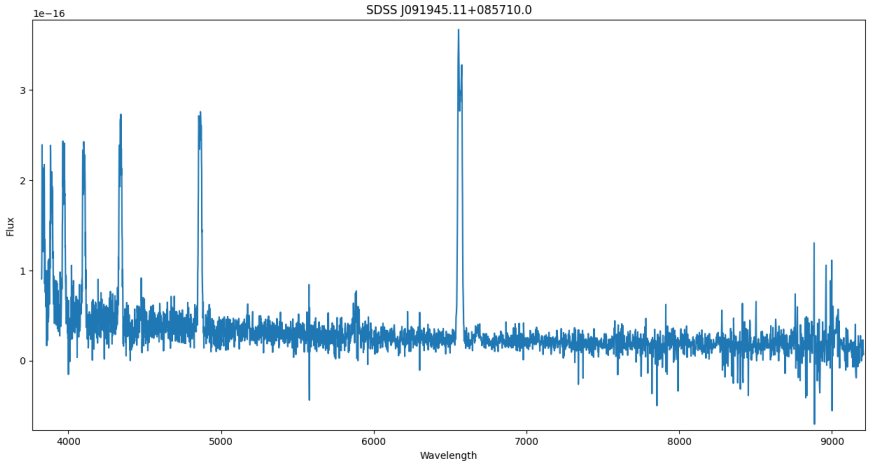

(A) The obtained accretion disc spectrum of SDSS J091945.11+085710.0.

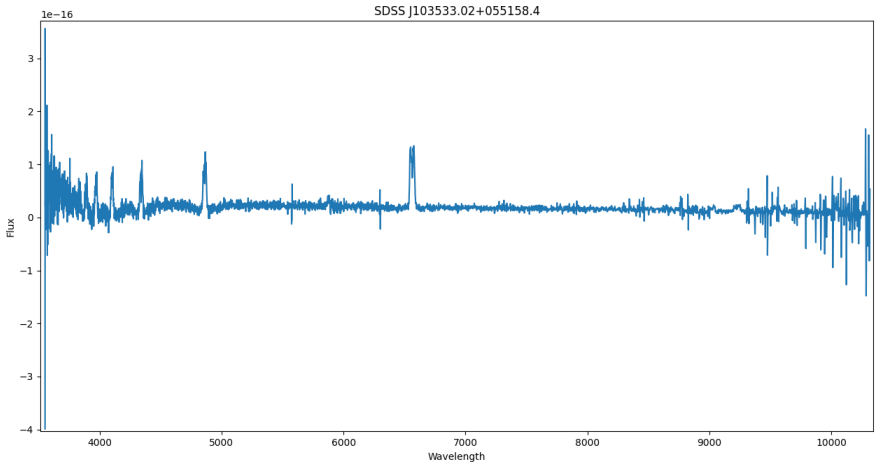

(B) The obtained accretion disc spectrum of SDSS J103533.02+055158.4

FIGURE 4.5: Accretion disc spectra obtained from the spectra of SDSS J091945.11+085710.0 and SDSS J103533.02+055158.4.

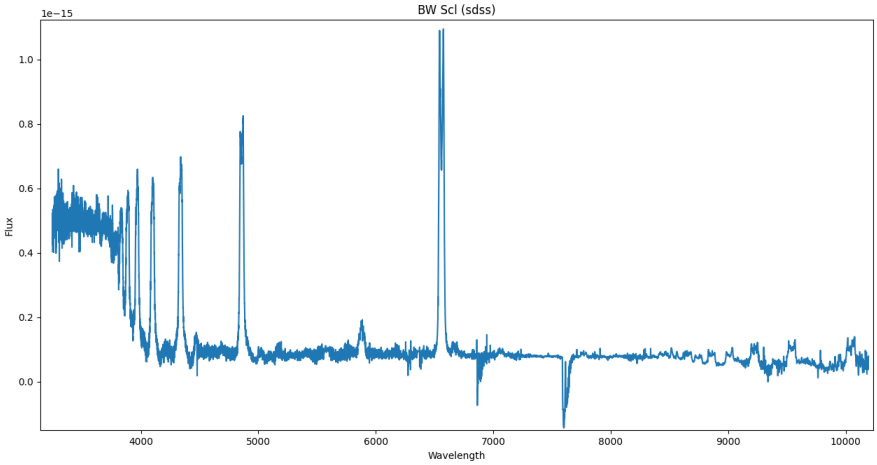

(A) The obtained accretion disc spectrum of BW Scl (SDSS).

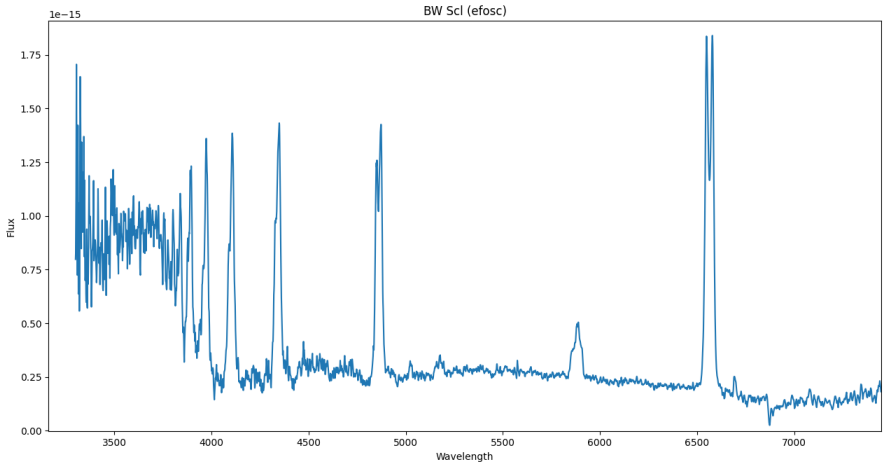

(B) The obtained accretion disc spectrum of BW Scl (efosc).

FIGURE 4.6: Accretion disc spectra obtained from two different spectra of BW Scl.

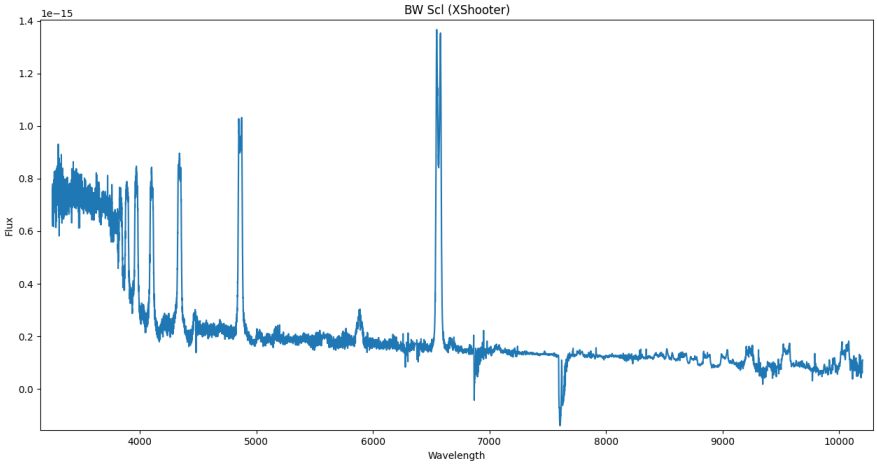

(A) The obtained accretion disc spectrum of BW Scl (XShooter).

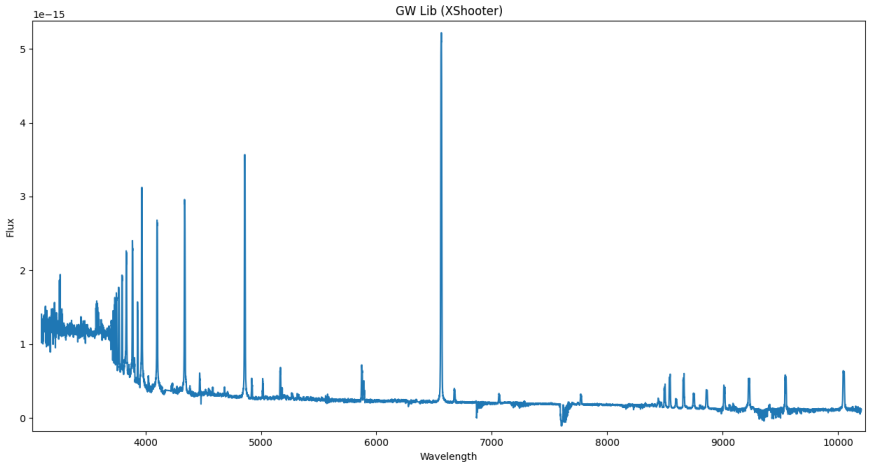

(B) The obtained accretion disc spectrum of GW Lib (XShooter).

FIGURE 4.7: Accretion disc spectra obtained from the spectra of BW Scl and GW Lib (both XShooter).

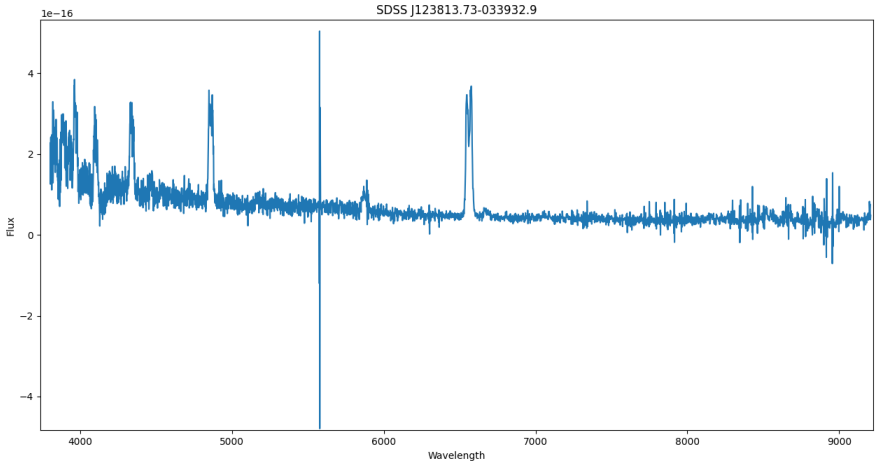

(A) The obtained accretion disc spectrum of SDSS J123813.73-033932.9.

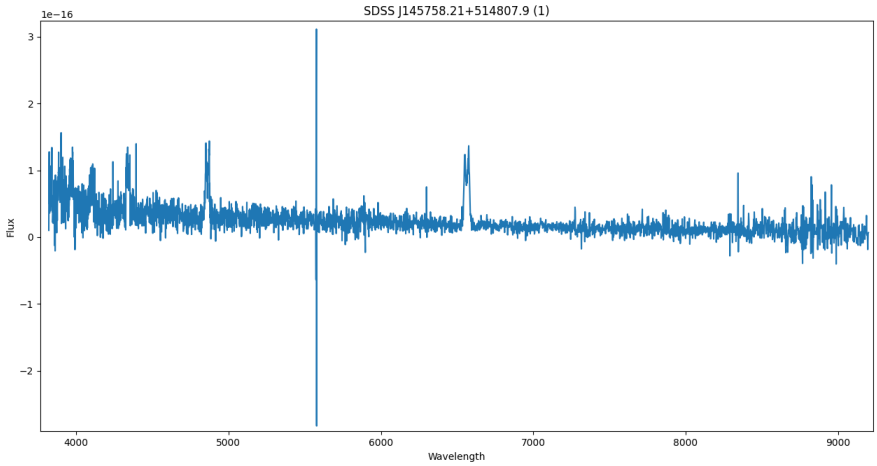

(B) The obtained accretion disc spectrum of SDSS J145758.21+514807.9 (1).

FIGURE 4.8: Accretion disc spectra obtained from the spectra of SDSS J123813.73-033932.9 and SDSS J145758.21+514807.9 (1).

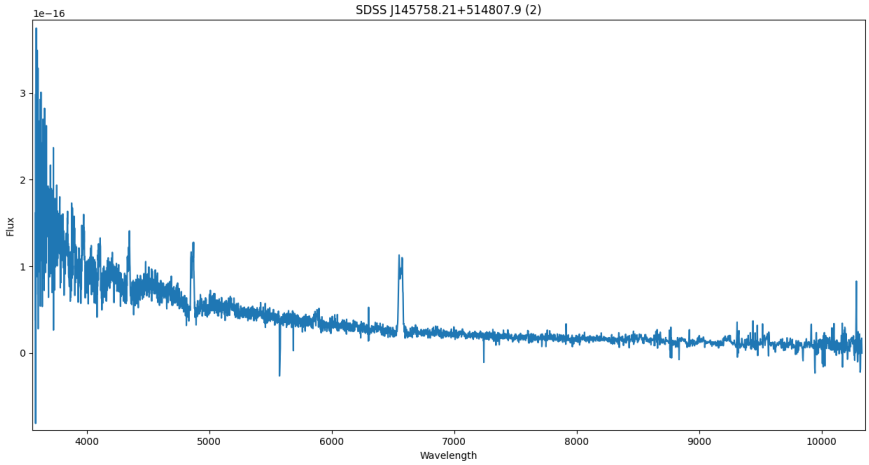

(A) The obtained accretion disc spectrum of SDSS J145758.21+514807.9 (2).

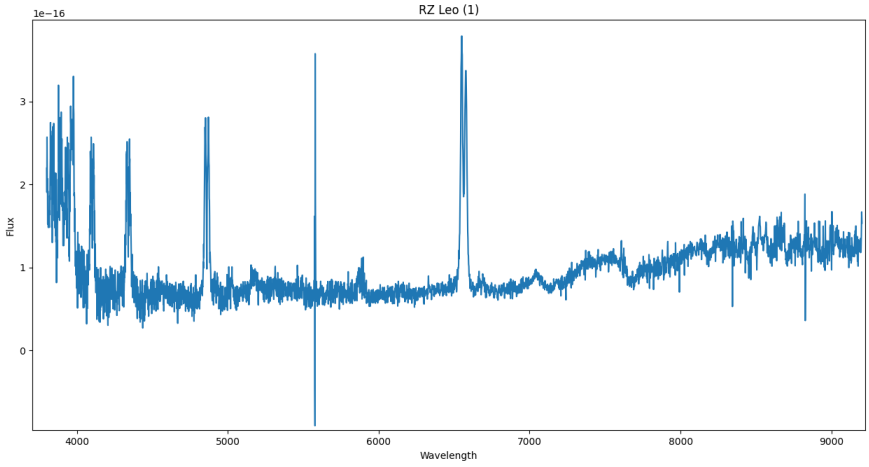

(B) The obtained accretion disc spectrum of RZ Leo (1, SDSS).

FIGURE 4.9: Accretion disc spectra obtained from the spectra of SDSS J145758.21+514807.9 (2) and RZ Leo (1, SDSS).

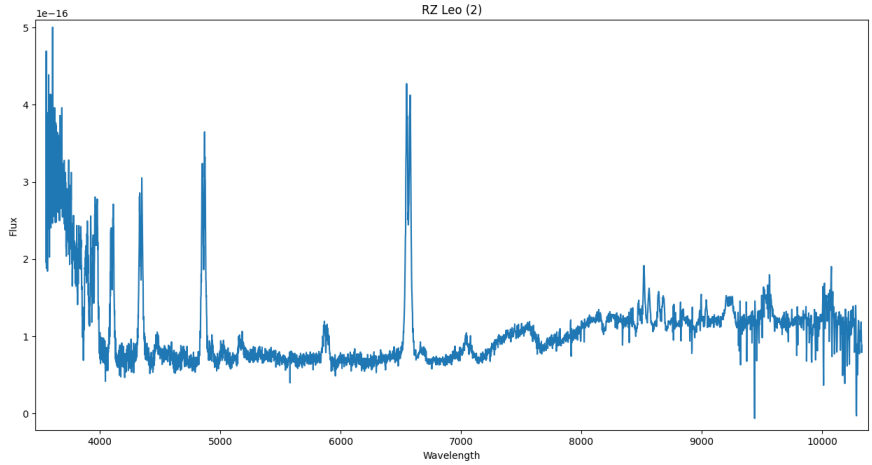

(A) The obtained accretion disc spectrum of RZ Leo (1, SDSS).

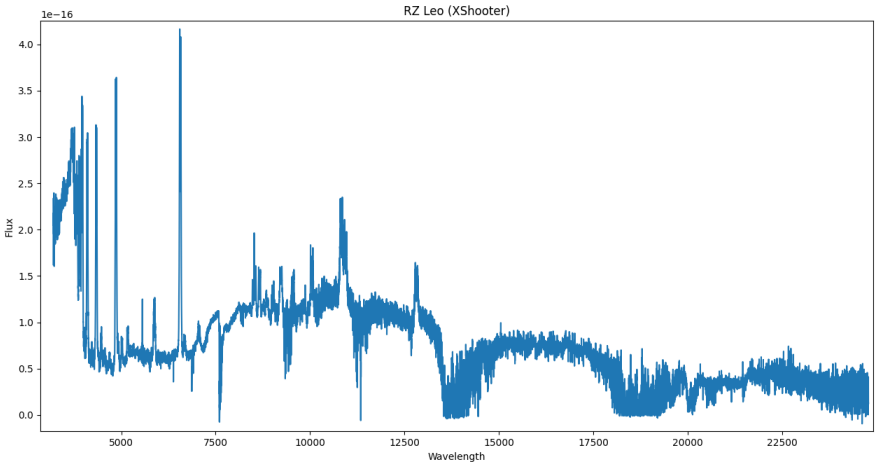

(B) The obtained accretion disc spectrum of RZ Leo (X-shooter).

FIGURE 4.10: Accretion disc spectra obtained from two different spectra of RZ Leo.

TABLE 4.1: Obtained values of disc luminosities, total luminosities, contributions of disc luminosities relative to total luminosities, and apparent and absolute magnitudes of accretion discs.

Object name	**Disc luminosity[erg s^{-1}]**	**Total luminosity[erg s^{-1}]**	**Contribution[%]**	m_V**[mag]**	M_V**[mag]**
EZ Lyn (1)	1.553e30	8.763e30	18	20.182	14.360
EZ Lyn (2)	3.252e30	1.256e31	26	19.427	13.605
EZ Lyn (3)	2.241e30	1.141e31	20	19.333	13.511
EZ Lyn (4)	2.023e30	1.149e31	18	20.975	15.153
EZ Lyn (5)	1.408e30	1.105e31	13	20.831	15.010
MT Com	5.449e30	1.315e31	42	20.437	12.780
SDSS J1435+23	5.580e30	1.420e31	39	19.503	12.913
SDSS J0904+44	2.627e30	1.152e31	23	21.370	13.751
SDSS J0919+08	2.629e30	1.147e31	23	20.170	13.698
SDSS J0353+05	1.439e30	6.028e30	24	20.530	14.080
BW Scl (SDSS)	2.108e30	9.360e30	23	18.984	14.117
BW Scl (efosc)	4.344e30	1.572e31	28	17.787	12.921
BW Scl (X-shooter)	3.478e30	1.140e31	31	18.180	13.314
GW Lib	7.384e30	1.662e31	44	17.826	12.561
SDSS J1238-03	4.095e30	1.280e31	32	19.273	13.121
SDSS J1457+51 (1)	1.569e31	2.653e31	59	20.344	11.557
SDSS J1457+51 (2)	2.465e31	3.366e31	73	19.822	11.035
RZ Leo (1, SDSS)	1.576e31	2.952e31	53	19.231	11.987
RZ Leo (2, SDSS)	1.732e31	2.530e31	69	19.199	11.955
RZ Leo (X-shooter)	2.885e31	3.686e31	78	19.309	12.065

Chapter 5

Final conclusion

Using optical spectroscopy we were able to model single WDs and obtain $T_{\rm eff}$ with reasonable accuracy ($\Delta T_{\rm eff} < 1200\,{\rm K}$, $\Delta \log g \leq 0.50$). We were also able to recover the correct parameters ($T_{\rm eff}$ and $\log g$) of modified theorized white dwarf spectra, with an accuracy of $\Delta T_{\rm eff} \leq 1250\,{\rm K}$, $\Delta \log g \leq 0.50$. We showed that rotational broadening ($v_c \ll 1000\,{\rm km/s}$) and zeeman-effect ($B_{\rm s} < 0.5\,{\rm MG}$) have negligible to zero effect on the modelling procedure. We compared our obtained results from modelling CVs to those obtained by others (e.g Pala et al. [13]) to show that we are able to produce similar results. Lastly, we modelled seven additional objects without reference $T_{\rm eff}$, assuming average WD surface gravity $\log g = 8.35$. We measured the total luminosity of each system, the luminosity of the accretion disc in each system, and the apparent magnitude and absolute magnitude of each accretion disc in the V-band. Contribution of the accretion disc to the total luminosity of the system, for each system, ranges between 13%-78%.

Appendix A

Model spectrum with noise and linecores cut

Here the results are shown for the model with noise added according to S/N of 20, 50 and 100, and with cuts made to the linecores with rotational velocity of 1000 km/s, 2000 km/s and 3000 km/s.

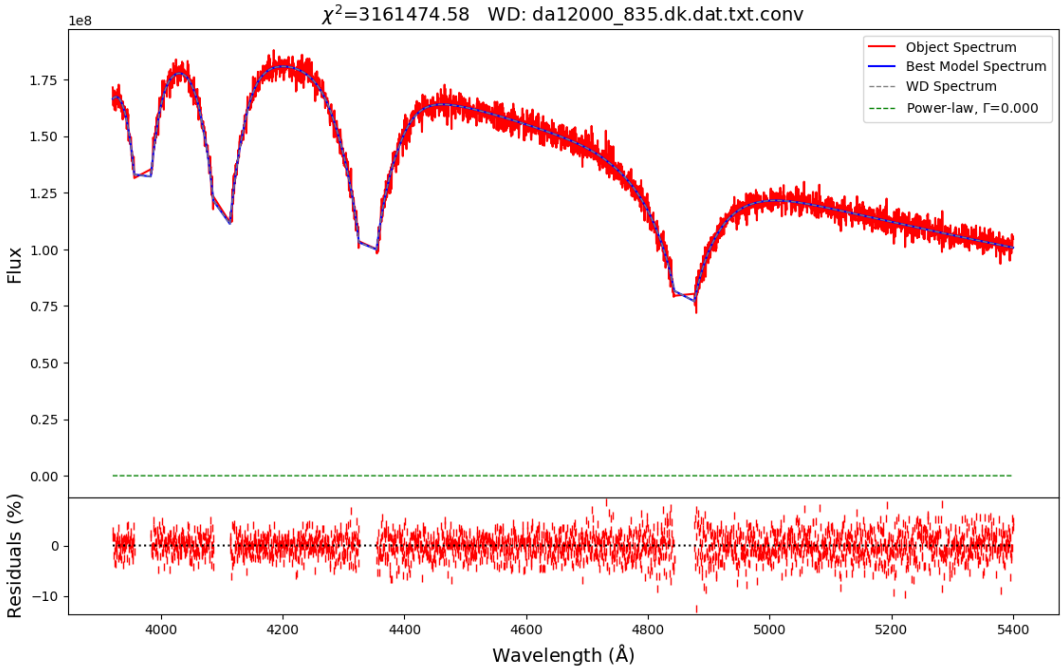

FIGURE A.1: Spectrum with S/N=50 and $v = 1000\,\mathrm{km/s}$.

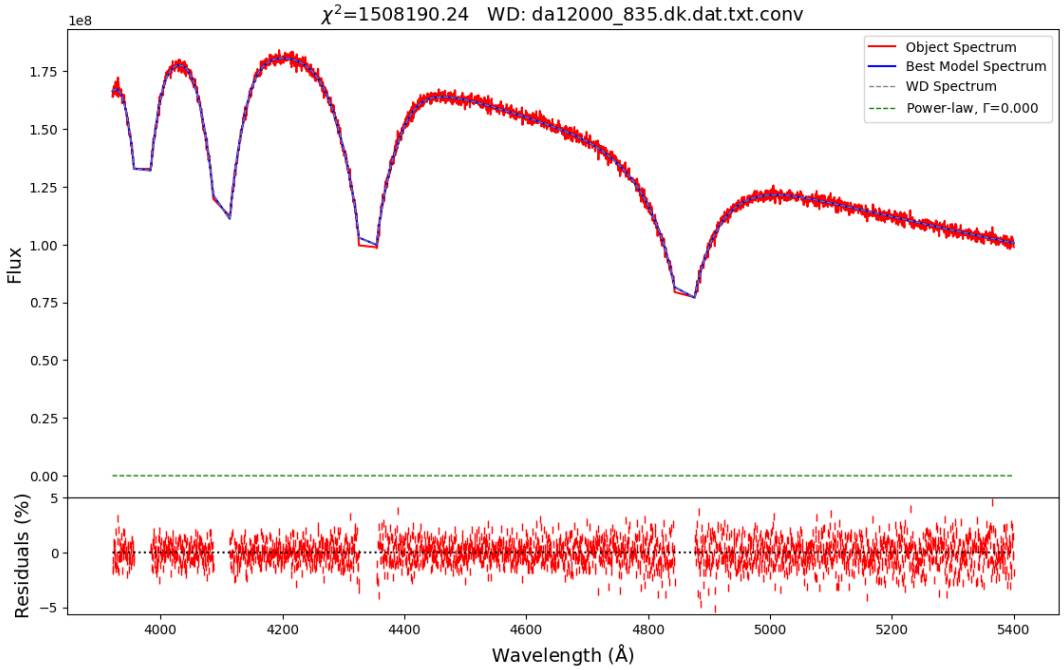

FIGURE A.2: Spectrum with S/N=100 and $v = 1000\,\mathrm{km/s}$.

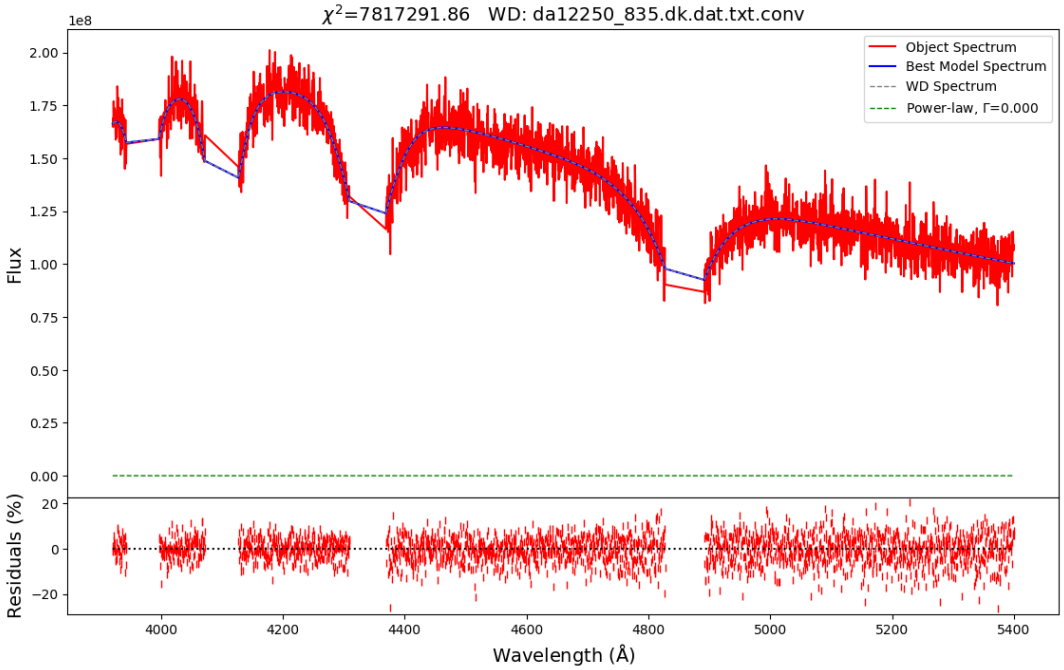

FIGURE A.3: Spectrum with S/N=20 and $v = 2000\,\mathrm{km/s}$.

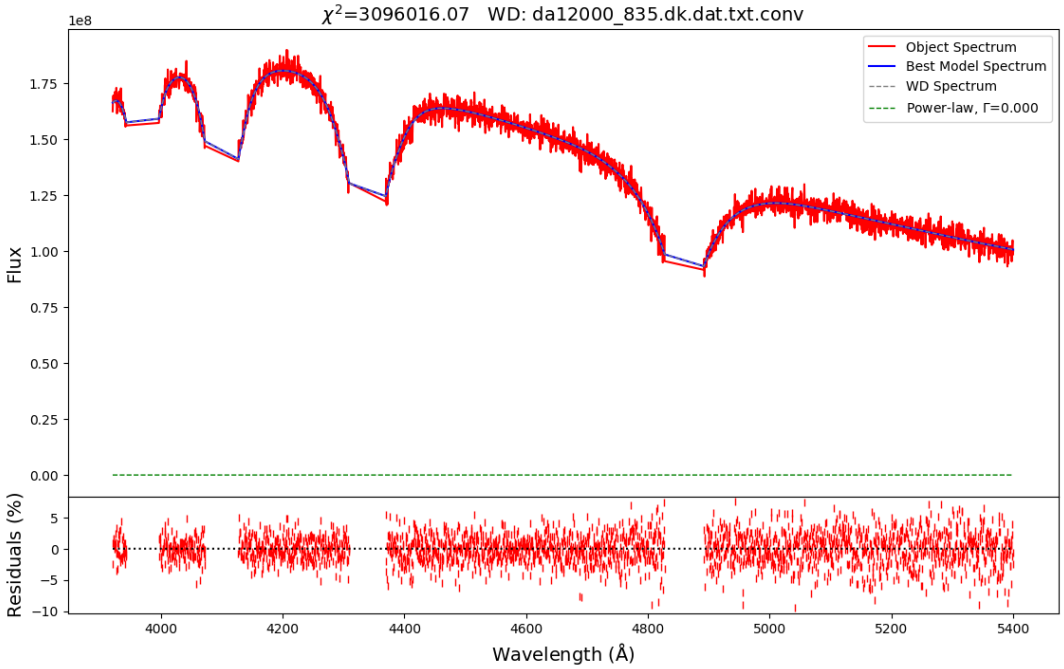

FIGURE A.4: Spectrum with S/N=50 and $v = 2000\,\mathrm{km/s}$.

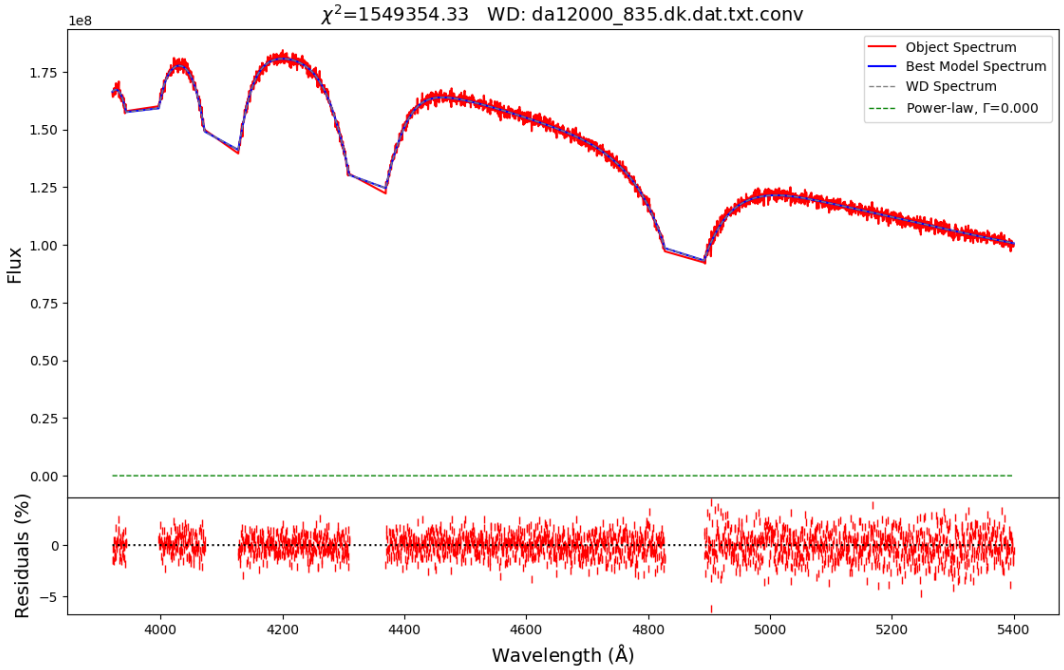

FIGURE A.5: Spectrum with S/N=100 and $v = 2000\,\mathrm{km/s}$.

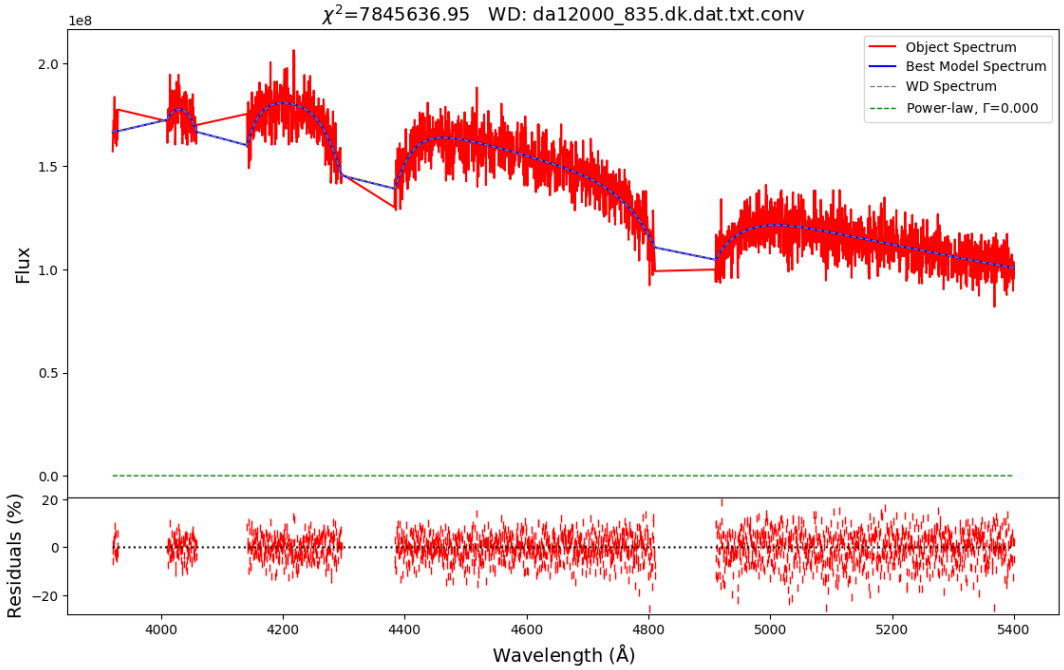

FIGURE A.6: Spectrum with S/N=20 and $v = 3000\,\mathrm{km/s}$.

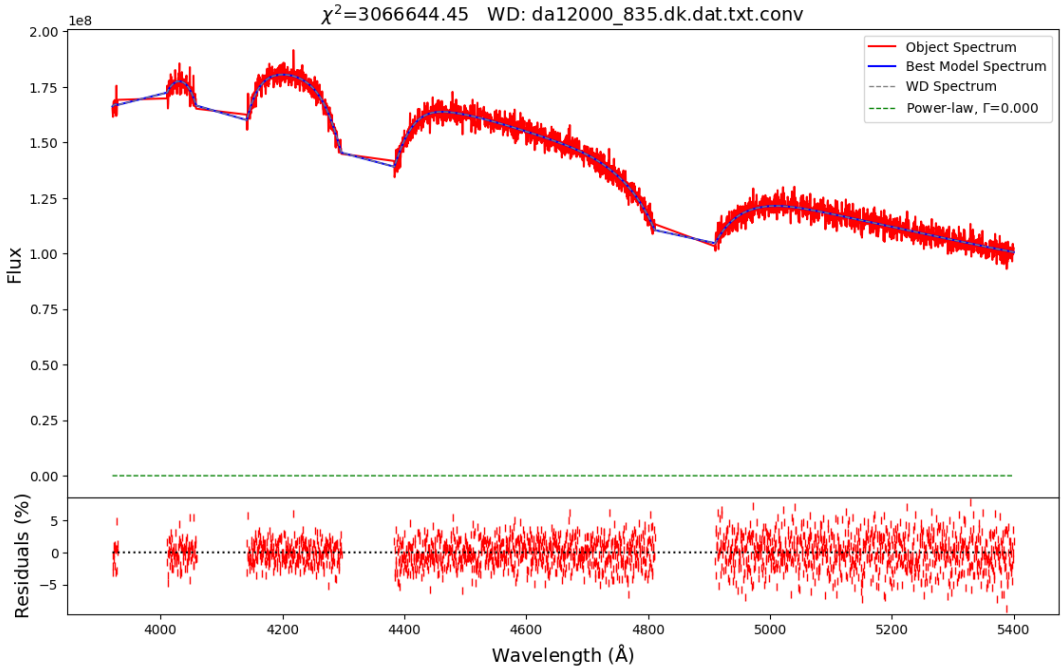

FIGURE A.7: Spectrum with S/N=50 and $v = 3000\,\mathrm{km/s}$.

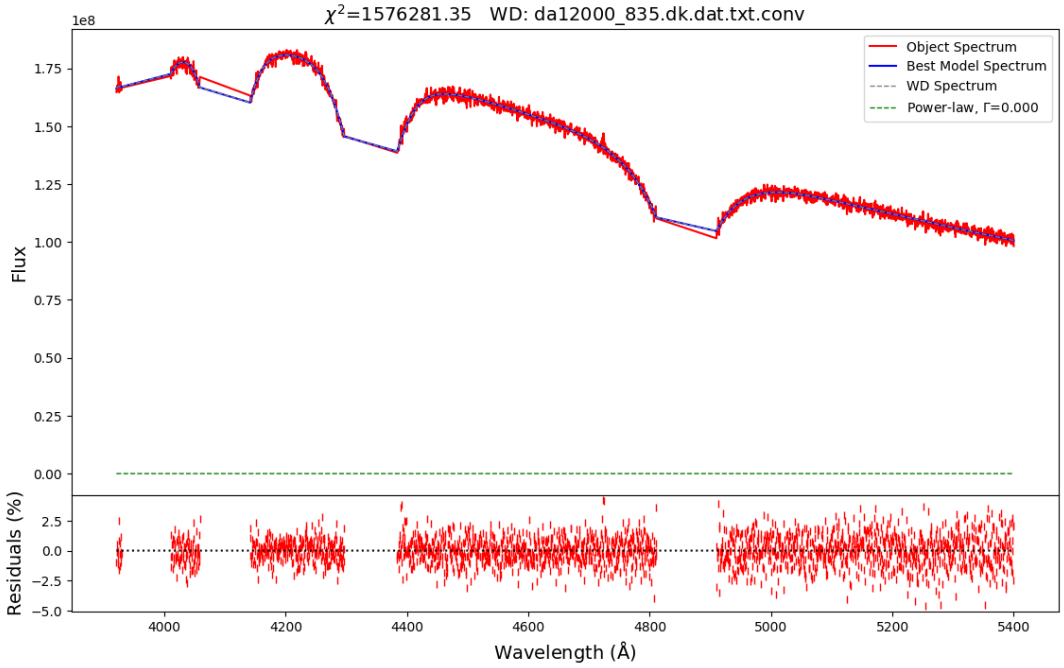

FIGURE A.8: Spectrum with S/N=100 and $v = 3000\,\mathrm{km/s}$.

Appendix B

Model spectrum with noise and linecores cut, power-law coefficient introduced

Here the results for modelling theoretical single WD spectrum with a power-law flux contribution are shown. In addition, noise is added to the spectrum and linecores are cut out.

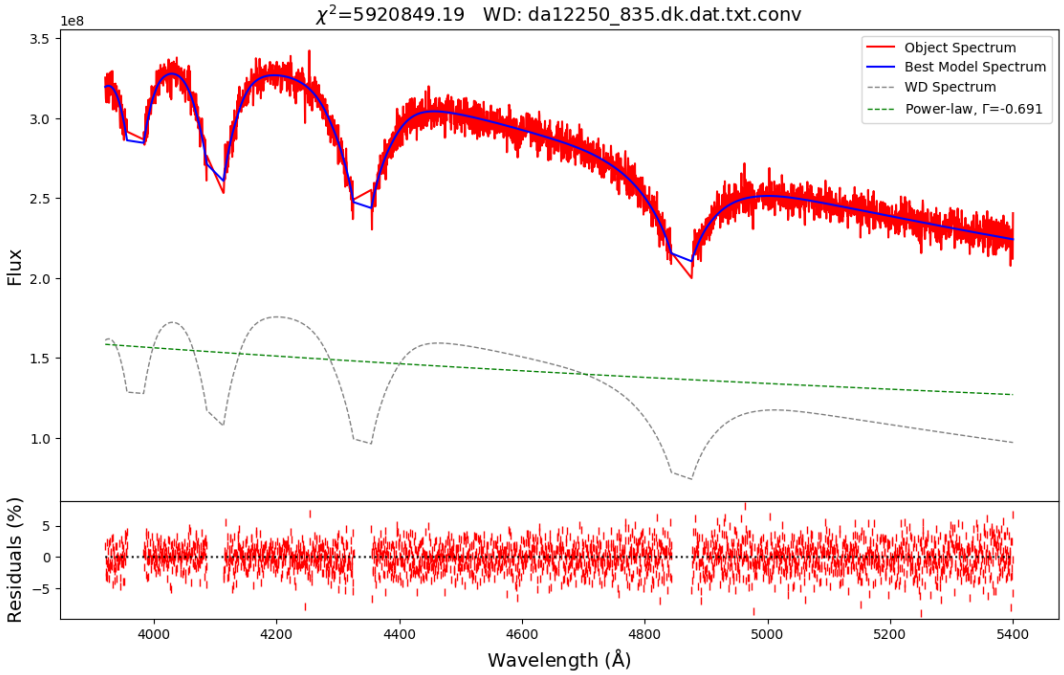

FIGURE B.1: Spectrum with S/N=50, $v = 1000\,\mathrm{km/s}$ and power-law flux contribution of 100%.

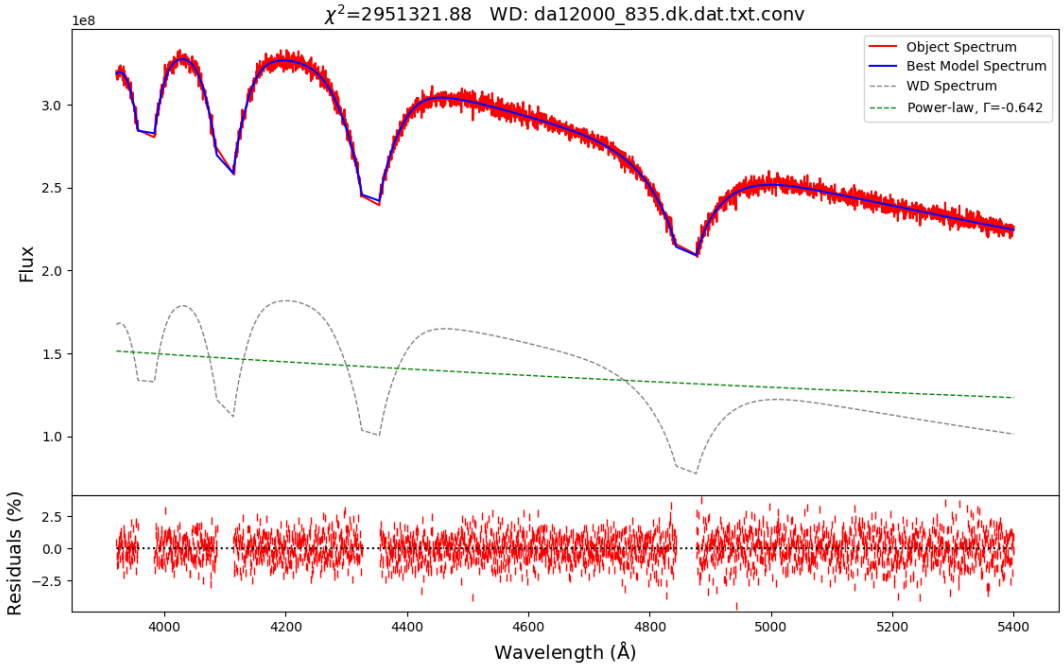

FIGURE B.2: Spectrum with S/N=100, $v = 1000\,\mathrm{km/s}$ and power-law flux contribution of 100%.

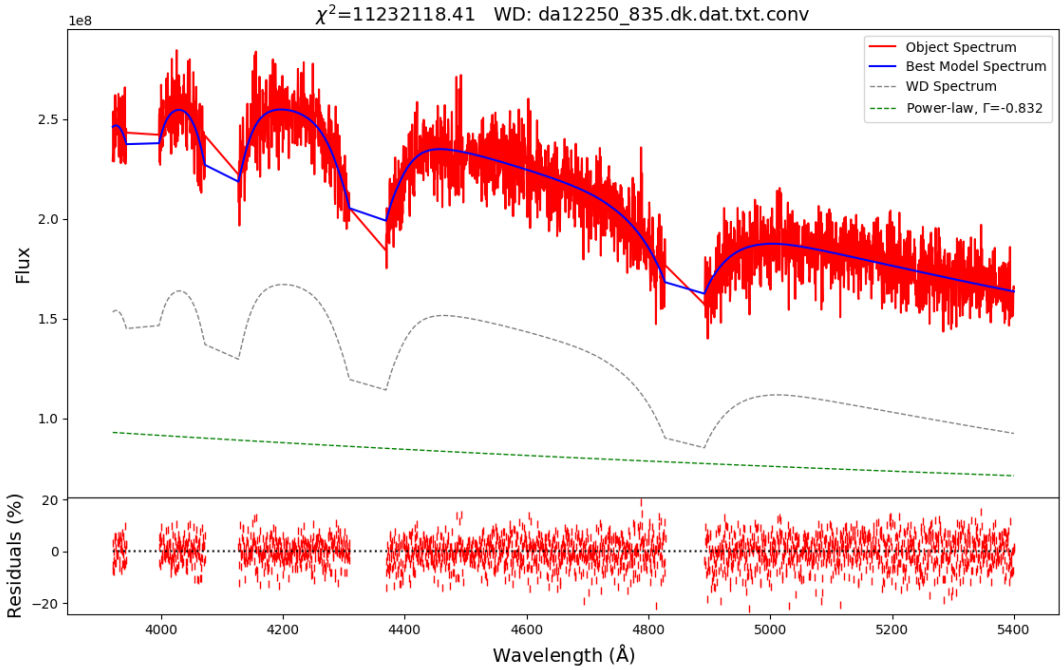

FIGURE B.3: Spectrum with S/N=20, $v = 2000\,\mathrm{km/s}$ and power-law flux contribution of 50%.

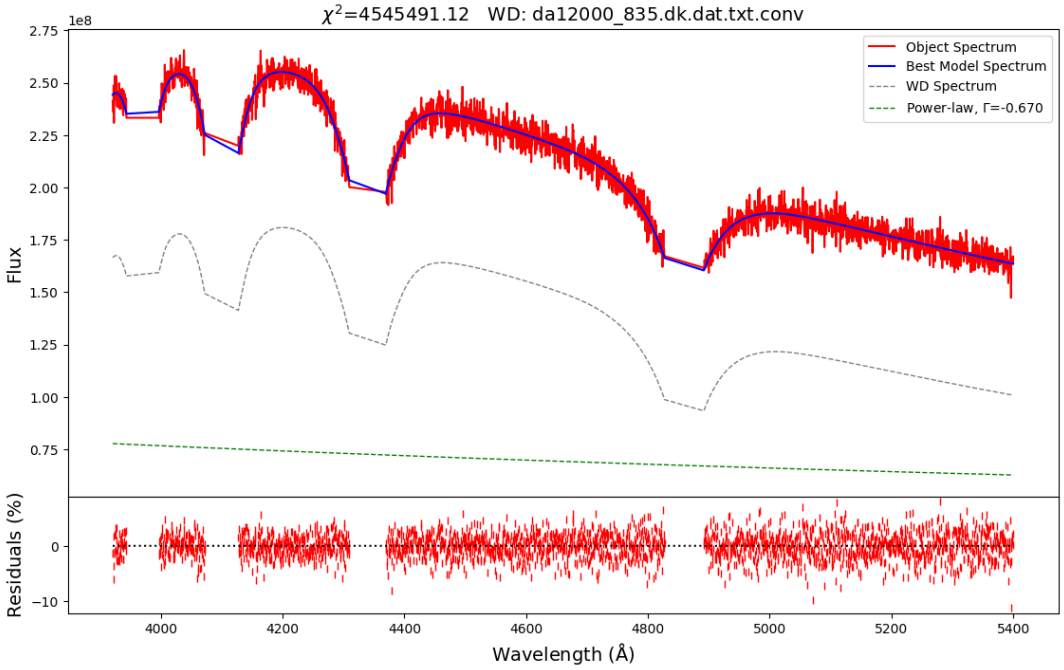

FIGURE B.4: Spectrum with S/N=50, $v = 2000\,\mathrm{km/s}$ and power-law flux contribution of 50%.

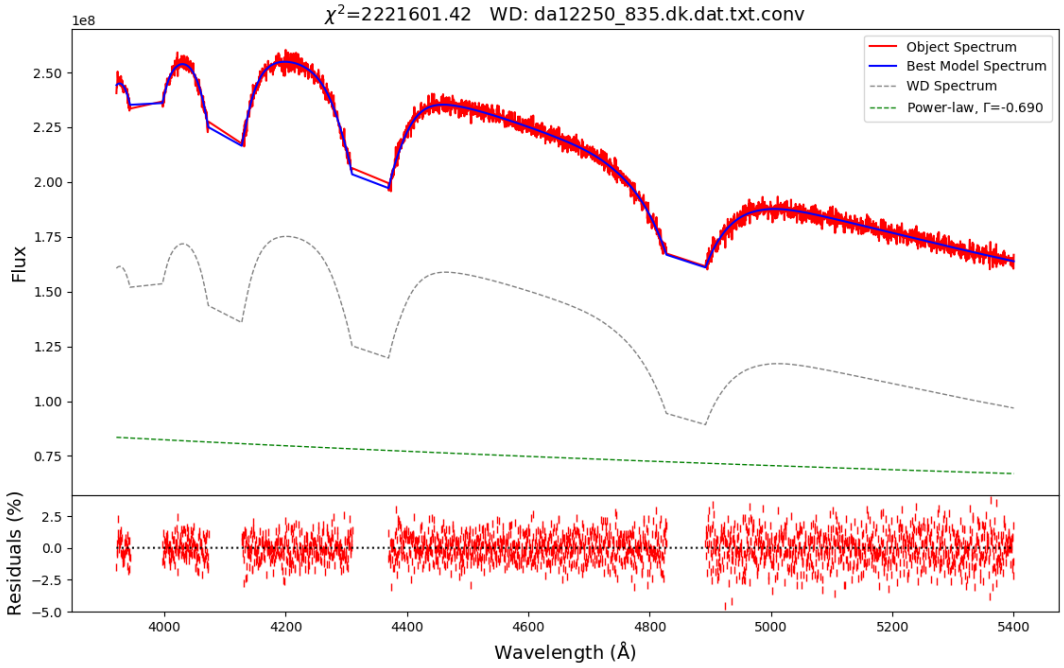

FIGURE B.5: Spectrum with S/N=100, $v = 2000\,\mathrm{km/s}$ and power-law flux contribution of 50%.

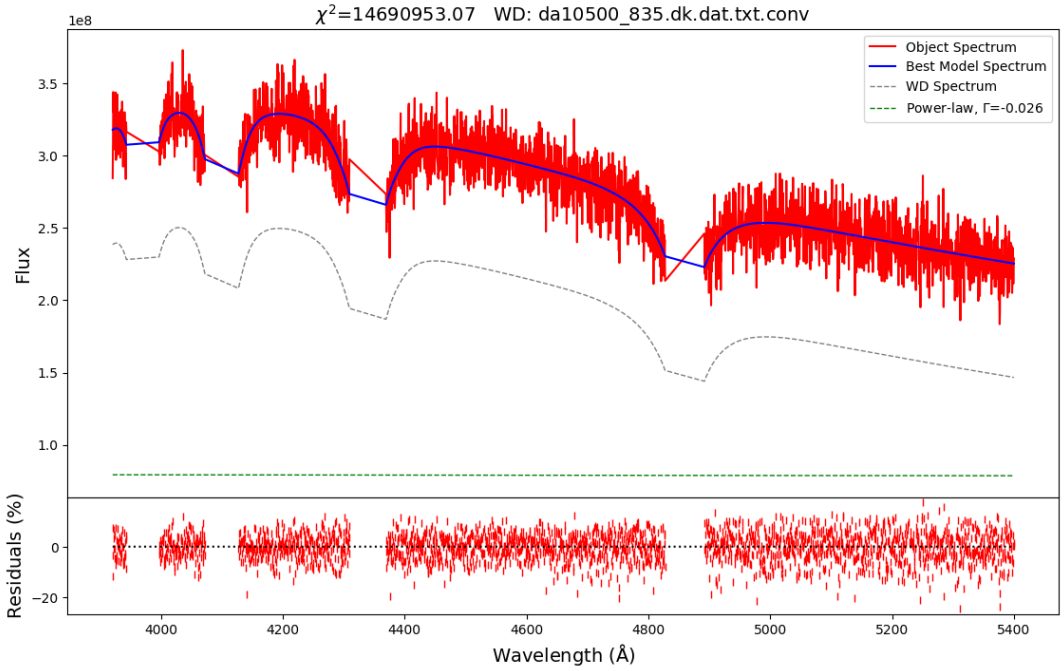

FIGURE B.6: Spectrum with S/N=20, $v = 2000\,\mathrm{km/s}$ and power-law flux contribution of 100%.

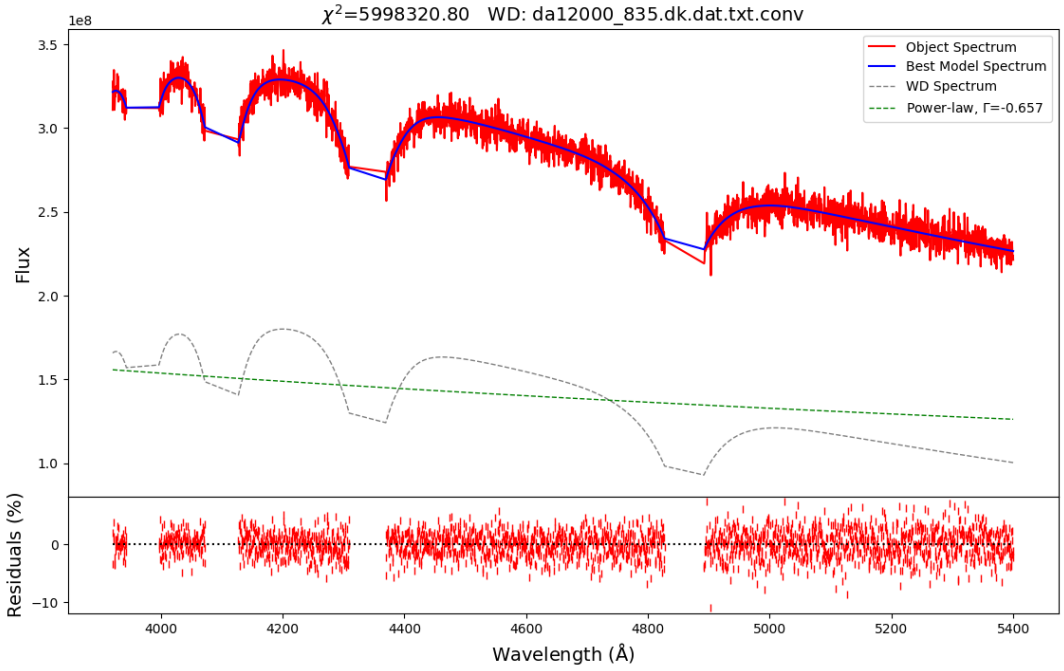

FIGURE B.7: Spectrum with S/N=50, $v = 2000\,\mathrm{km/s}$ and power-law flux contribution of 100%.

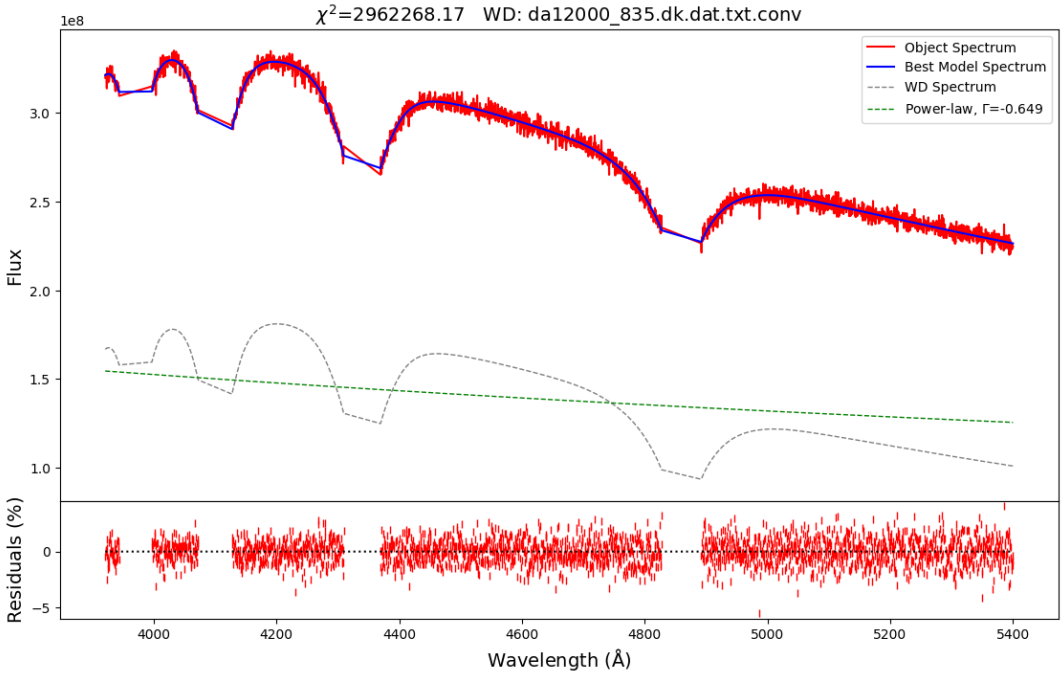

FIGURE B.8: Spectrum with S/N=100, $v = 2000\,\mathrm{km/s}$ and power-law flux contribution of 100%.

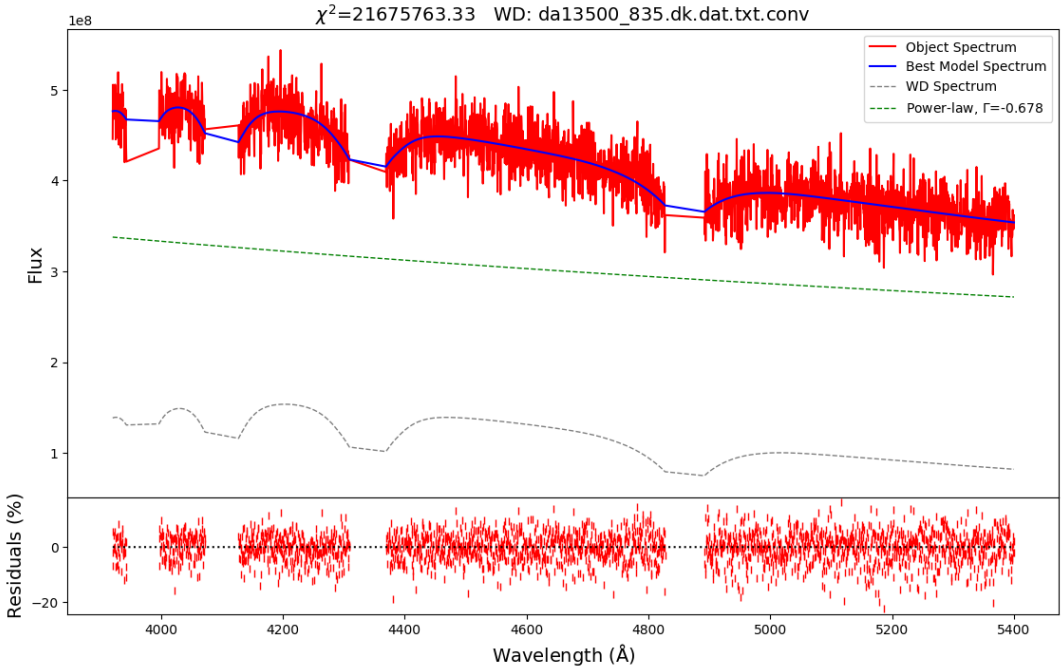

FIGURE B.9: Spectrum with S/N=20, $v = 2000\,\mathrm{km/s}$ and power-law flux contribution of 200%.

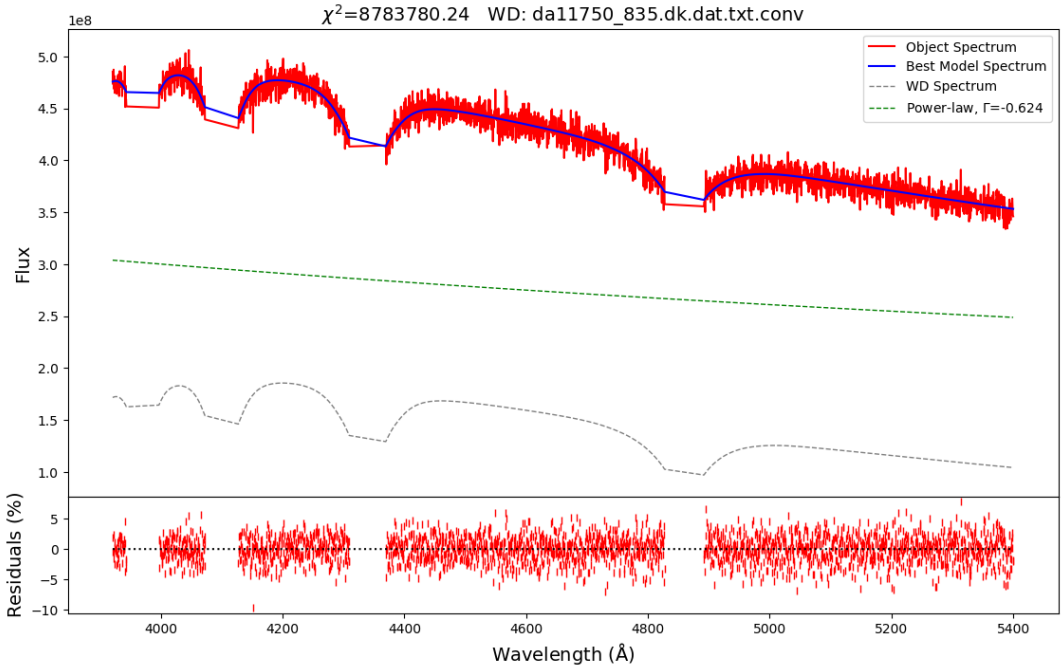

FIGURE B.10: Spectrum with S/N=50, $v = 2000\,\mathrm{km/s}$ and power-law flux contribution of 200%.

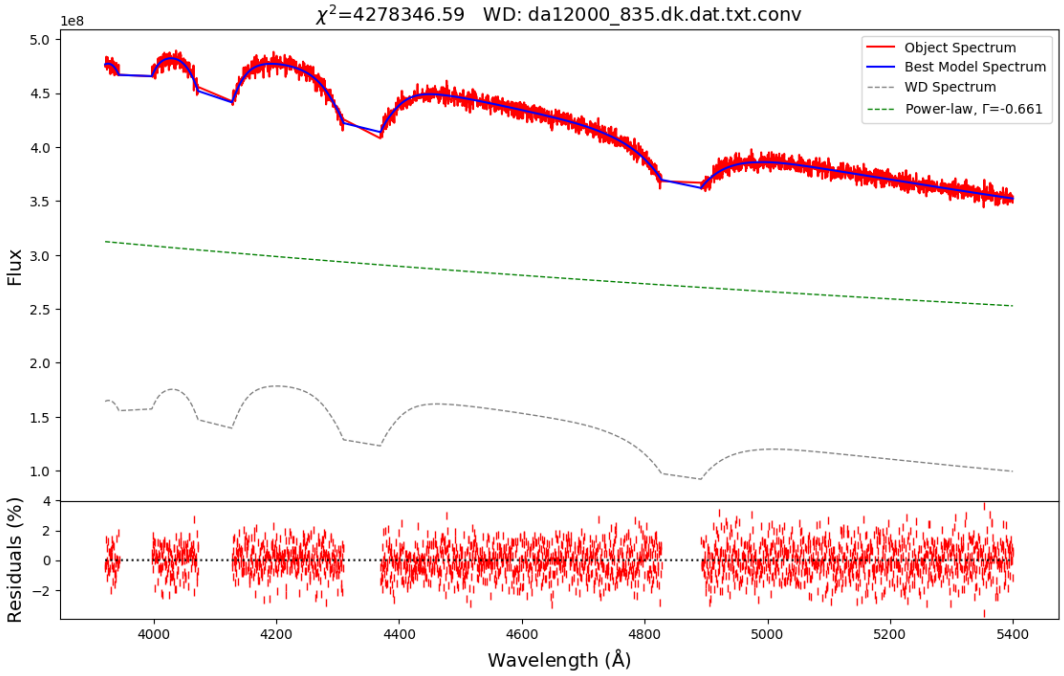

FIGURE B.11: Spectrum with S/N=100, $v = 2000\,\mathrm{km/s}$ and power-law flux contribution of 200%.

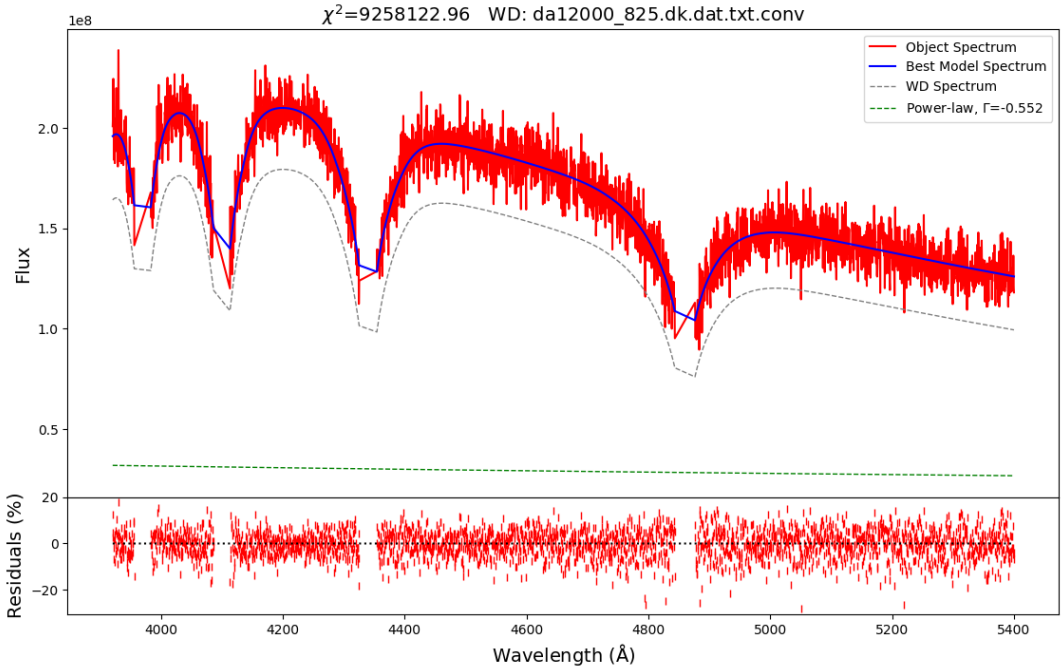

FIGURE B.12: Spectrum with S/N=20, $v = 1000\,\mathrm{km/s}$ and power-law flux contribution of 20%.

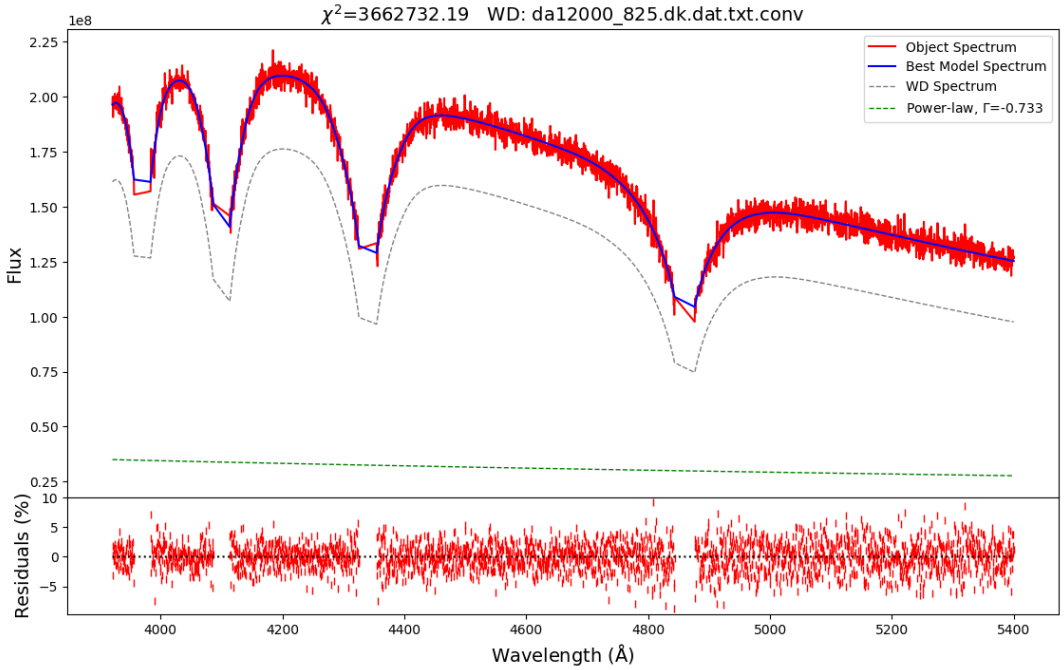

FIGURE B.13: Spectrum with S/N=50, $v = 1000\,\mathrm{km/s}$ and power-law flux contribution of 20%.

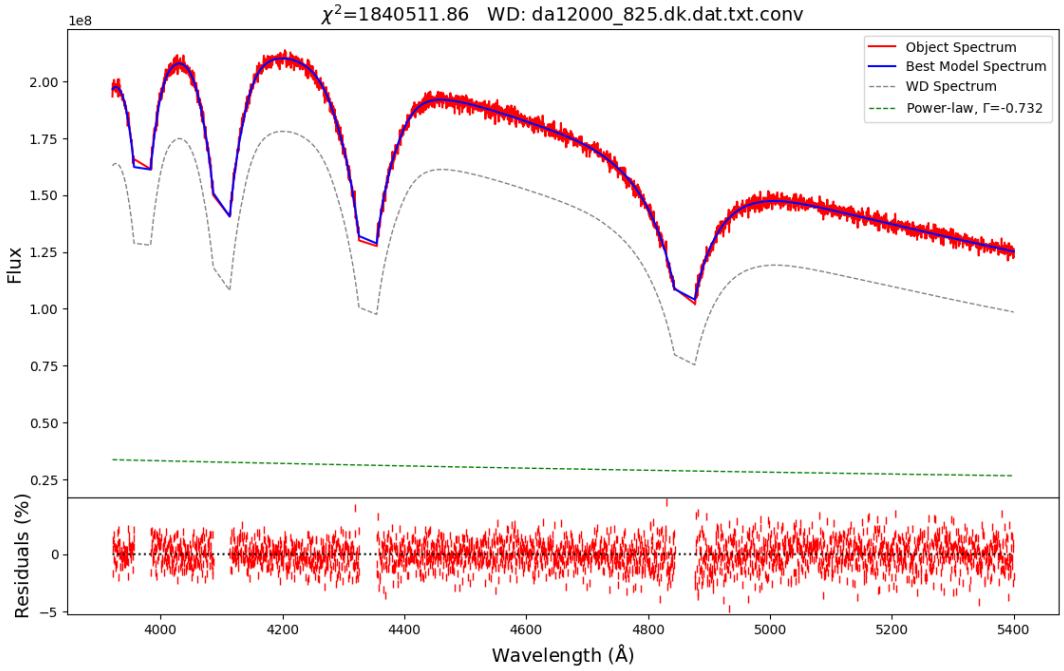

FIGURE B.14: Spectrum with S/N=100, $v = 1000\,\mathrm{km/s}$ and power-law flux contribution of 20%.

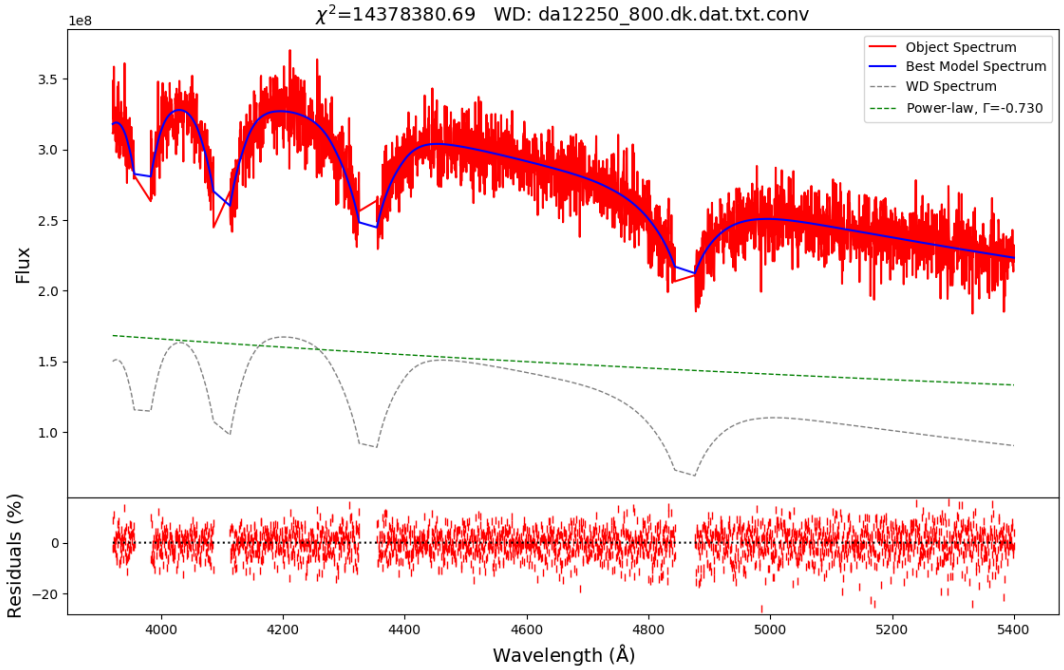

FIGURE B.15: Spectrum with S/N=20, $v = 1000\,\mathrm{km/s}$ and power-law flux contribution of 100%.

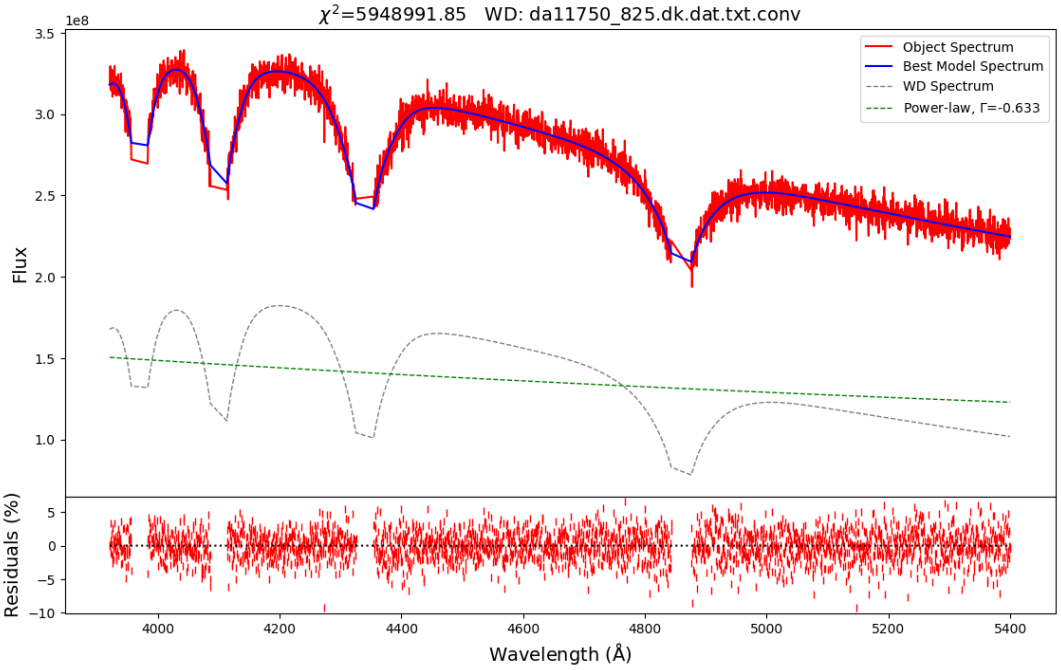

FIGURE B.16: Spectrum with S/N=50, $v = 1000\,\mathrm{km/s}$ and power-law flux contribution of 100%.

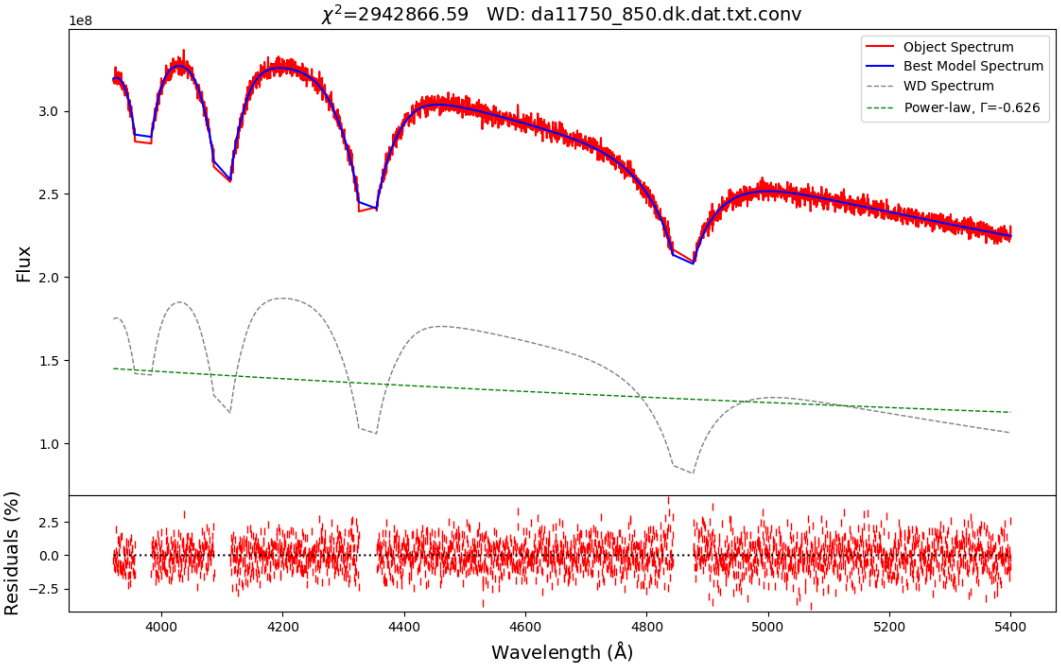

FIGURE B.17: Spectrum with S/N=100, $v = 1000\,\mathrm{km/s}$ and power-law flux contribution of 100%.

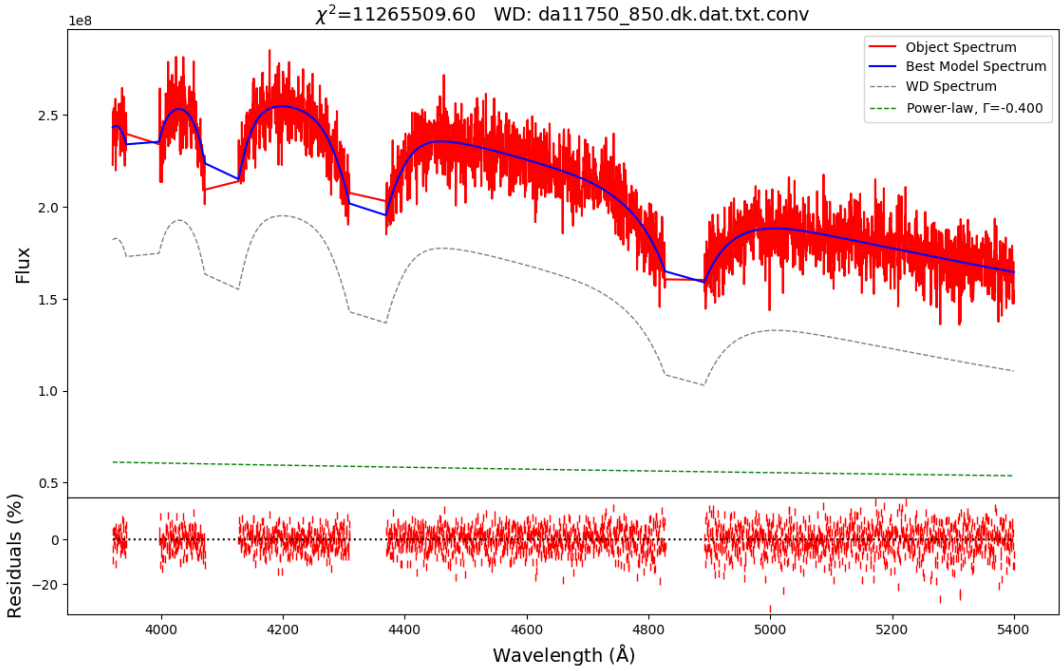

FIGURE B.18: Spectrum with S/N=20, $v = 2000\,\mathrm{km/s}$ and power-law flux contribution of 50%.

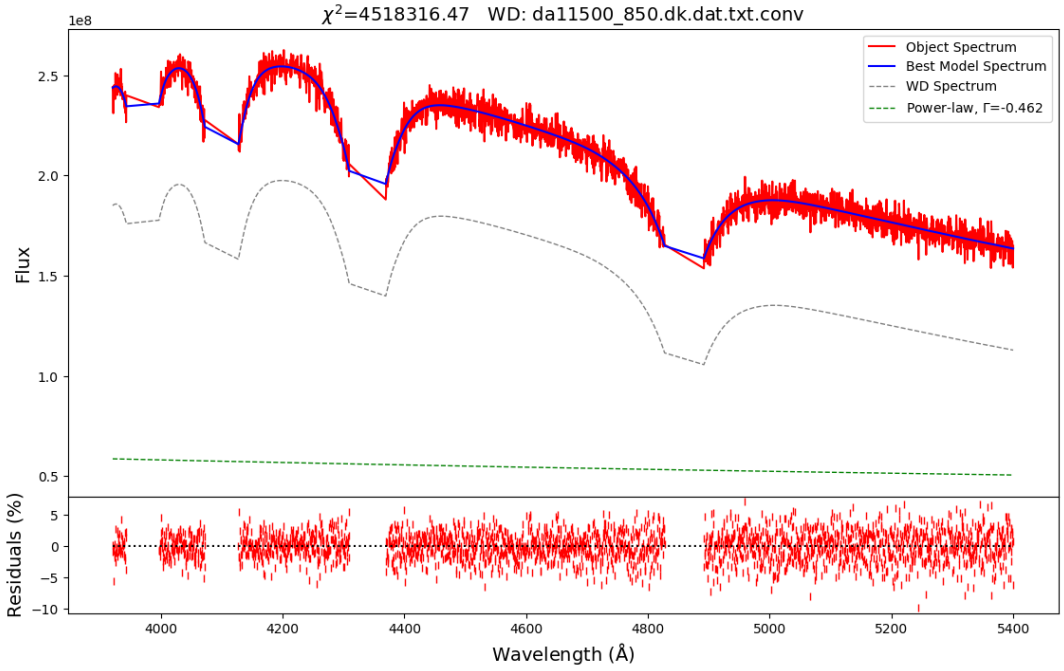

FIGURE B.19: Spectrum with S/N=50, $v = 2000\,\mathrm{km/s}$ and power-law flux contribution of 50%.

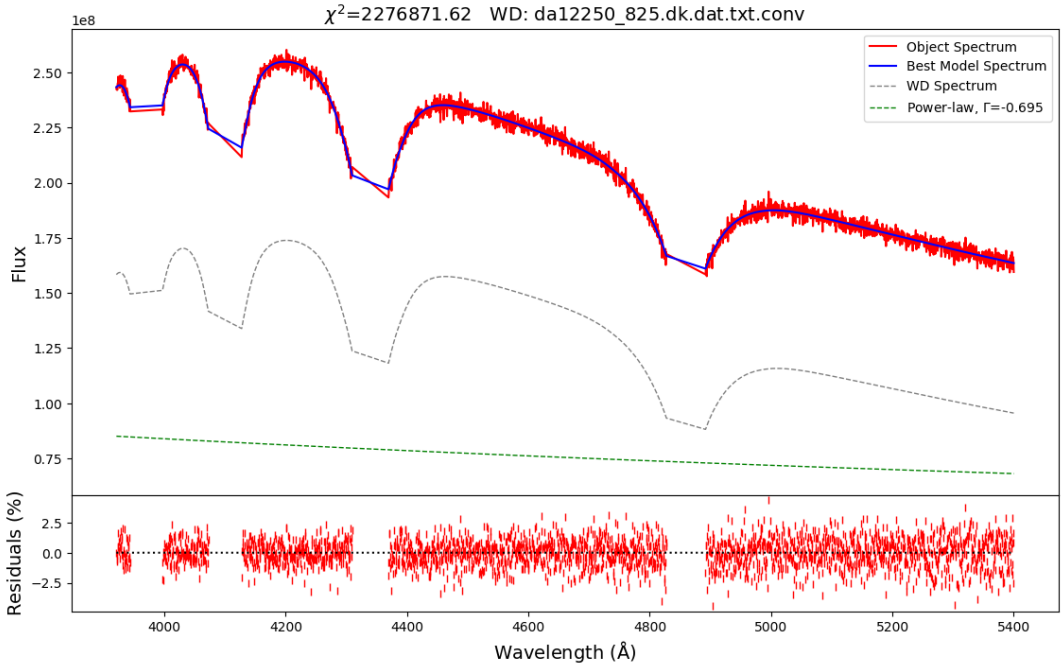

FIGURE B.20: Spectrum with S/N=100, $v = 2000\,\mathrm{km/s}$ and power-law flux contribution of 50%.

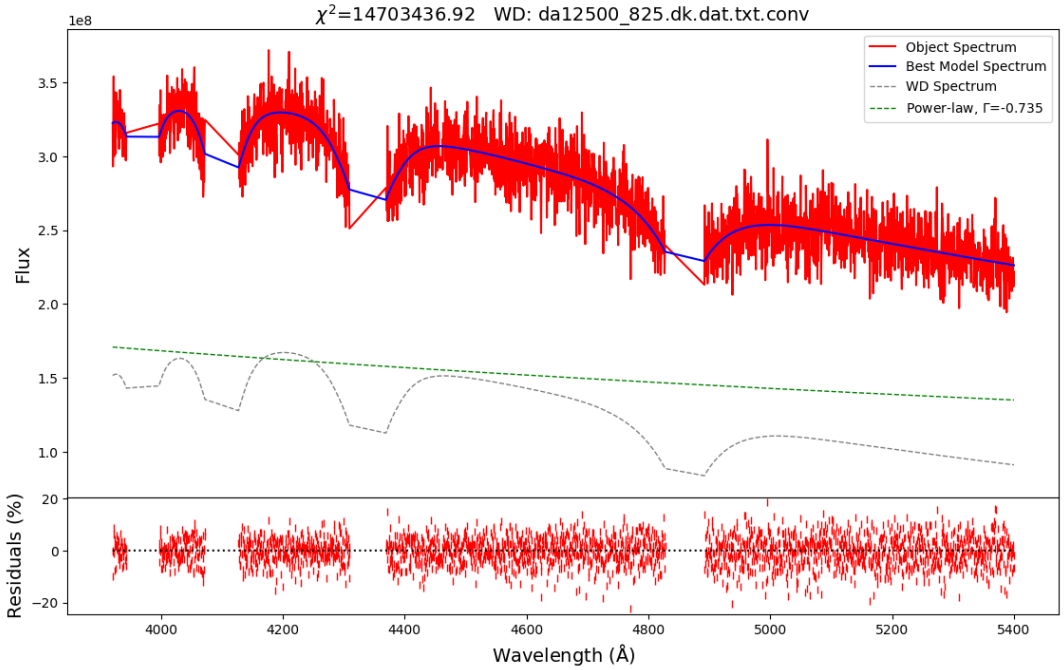

FIGURE B.21: Spectrum with S/N=20, $v = 2000\,\mathrm{km/s}$ and power-law flux contribution of 100%.

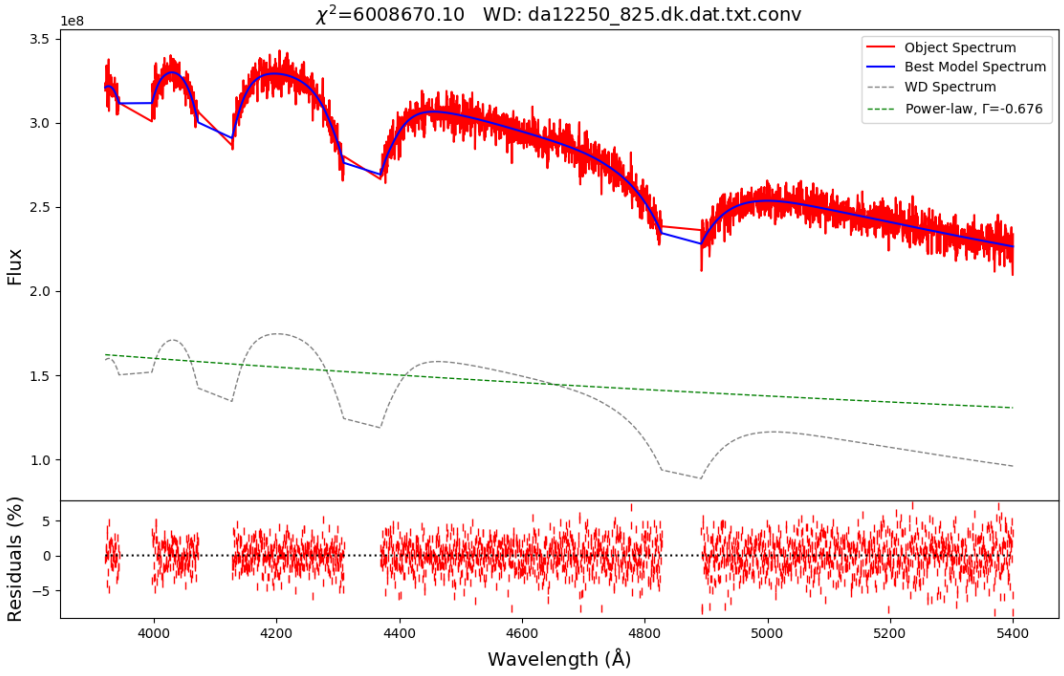

FIGURE B.22: Spectrum with S/N=100, $v = 2000\,\mathrm{km/s}$ and power-law flux contribution of 100%.

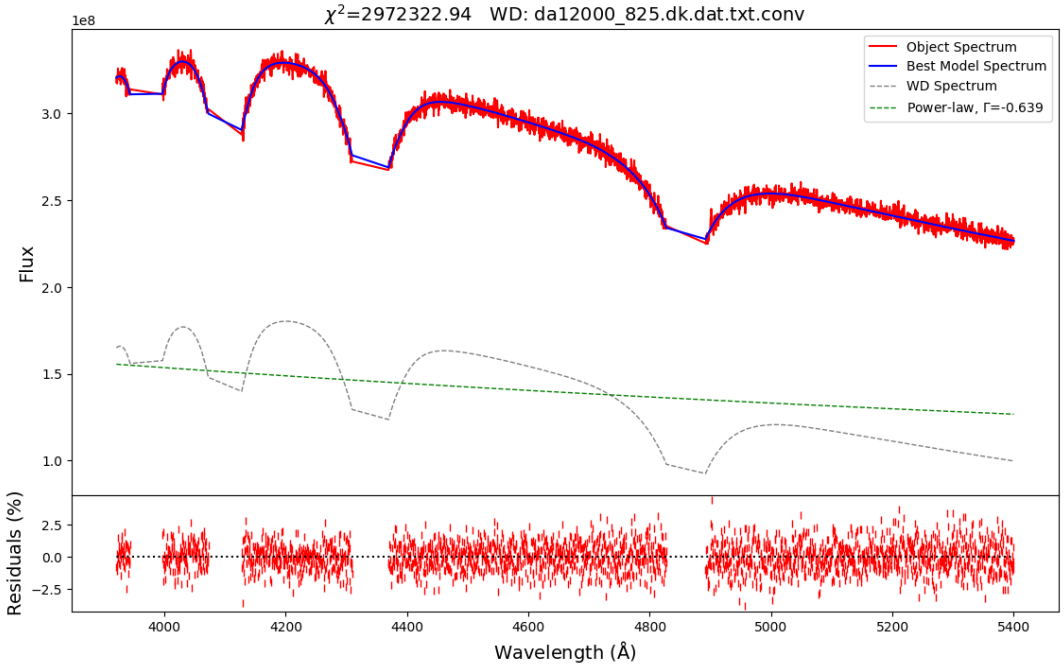

FIGURE B.23: Spectrum with S/N=100, $v = 2000\,\mathrm{km/s}$ and power-law flux contribution of 100%.

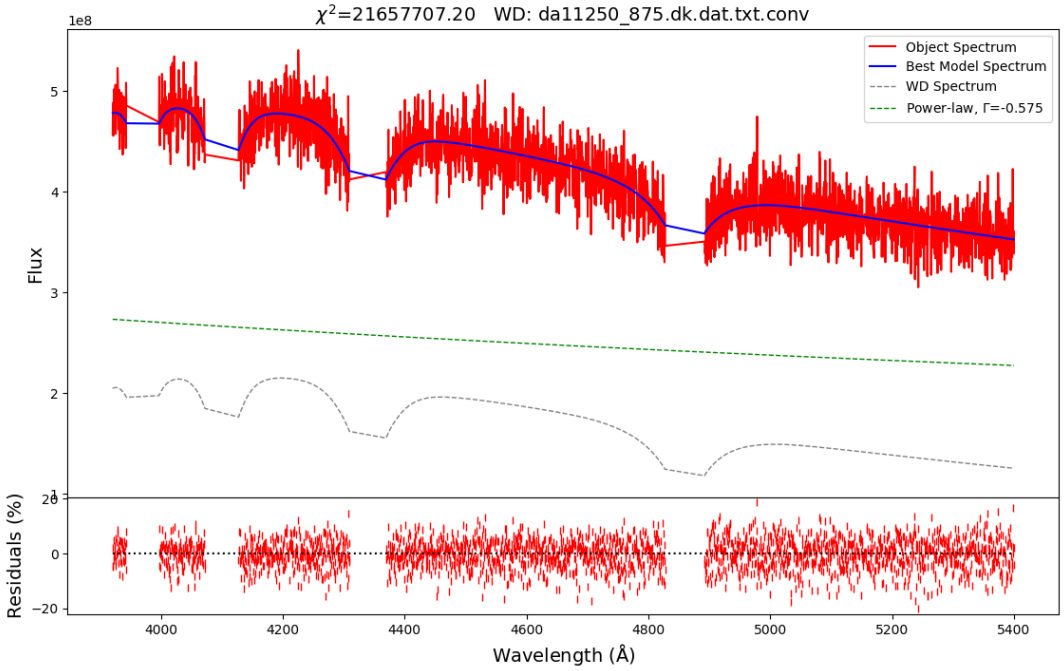

FIGURE B.24: Spectrum with S/N=20, $v = 2000\,\mathrm{km/s}$ and power-law flux contribution of 200%.

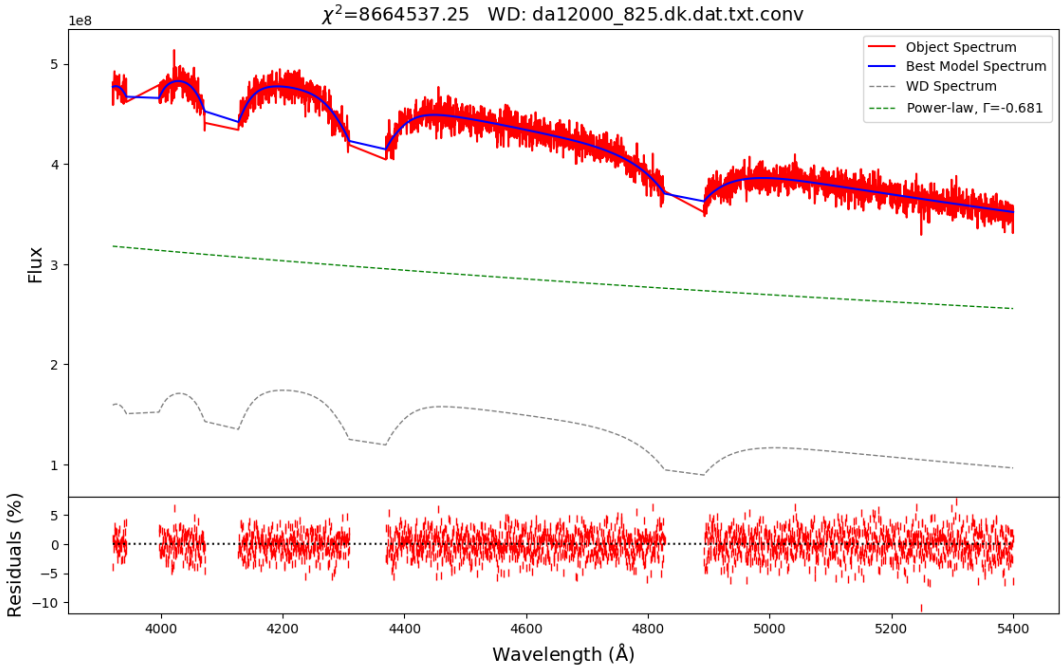

FIGURE B.25: Spectrum with S/N=50, $v = 2000\,\mathrm{km/s}$ and power-law flux contribution of 200%.

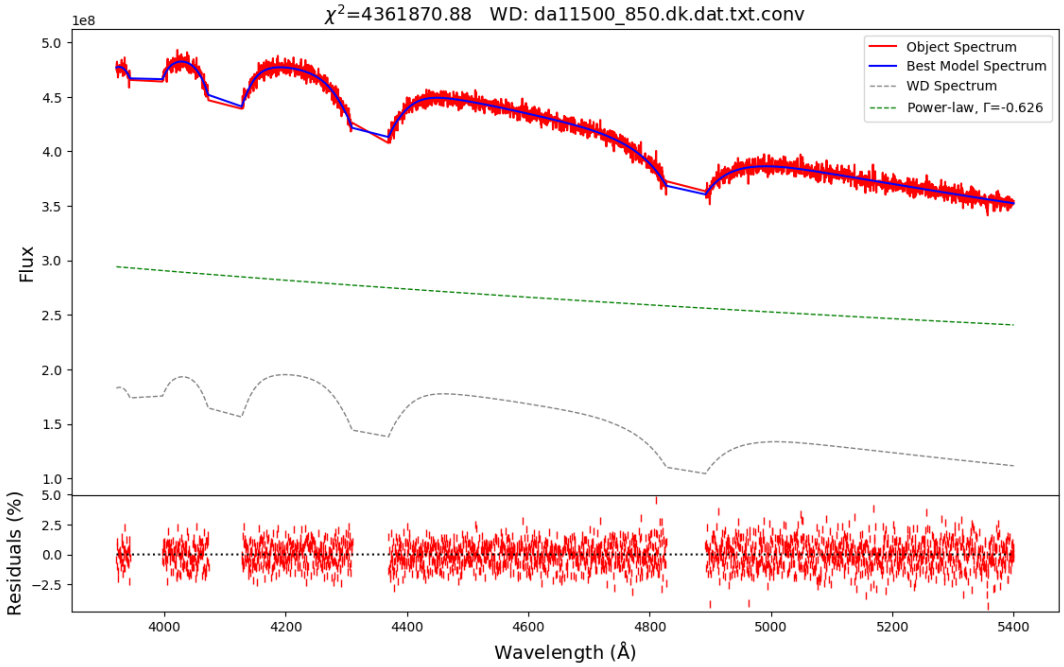

FIGURE B.26: Spectrum with S/N=100, $v = 2000\,\mathrm{km/s}$ and power-law flux contribution of 200%.

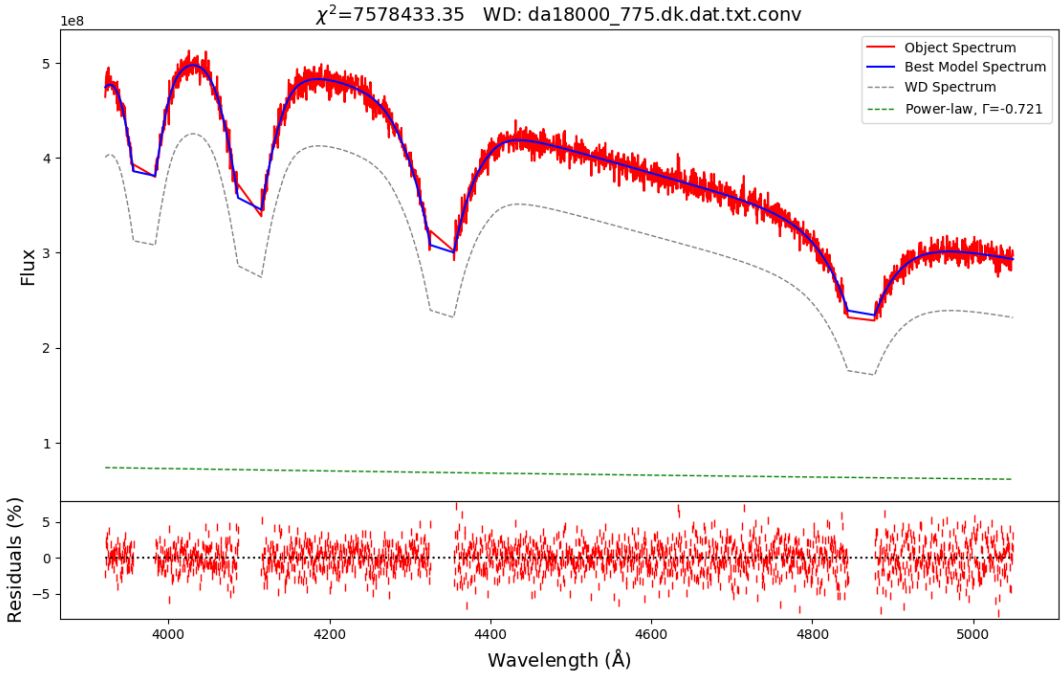

FIGURE B.27: Spectrum with S/N=50, $v = 1000\,\mathrm{km/s}$ and power-law flux contribution of 20%.

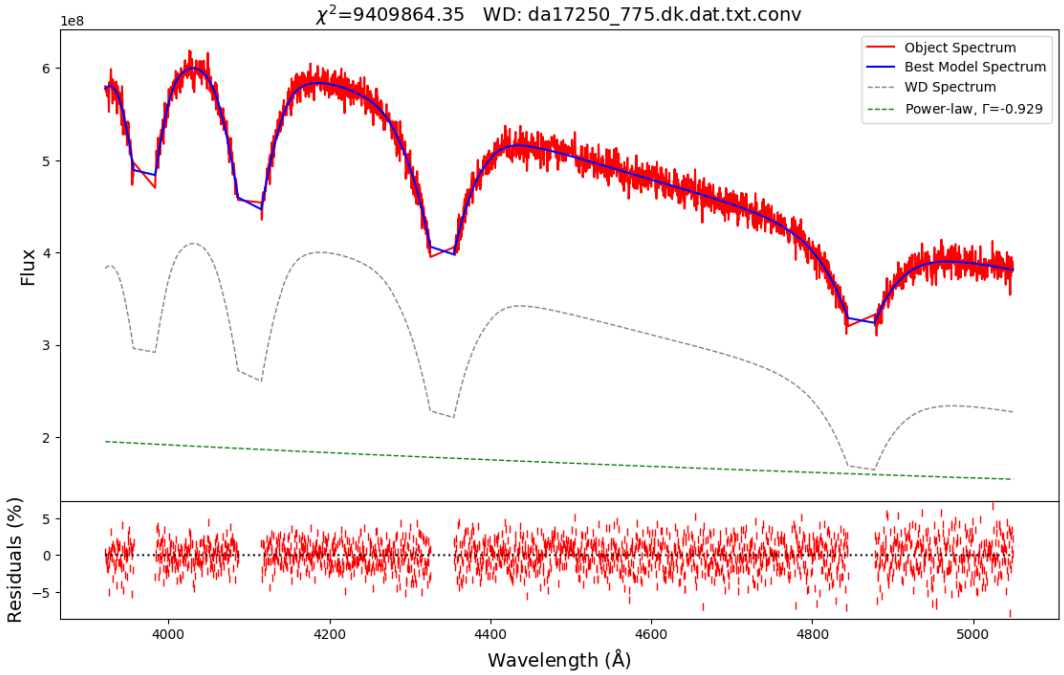

FIGURE B.28: Spectrum with S/N=50, $v = 1000\,\mathrm{km/s}$ and power-law flux contribution of 50%.

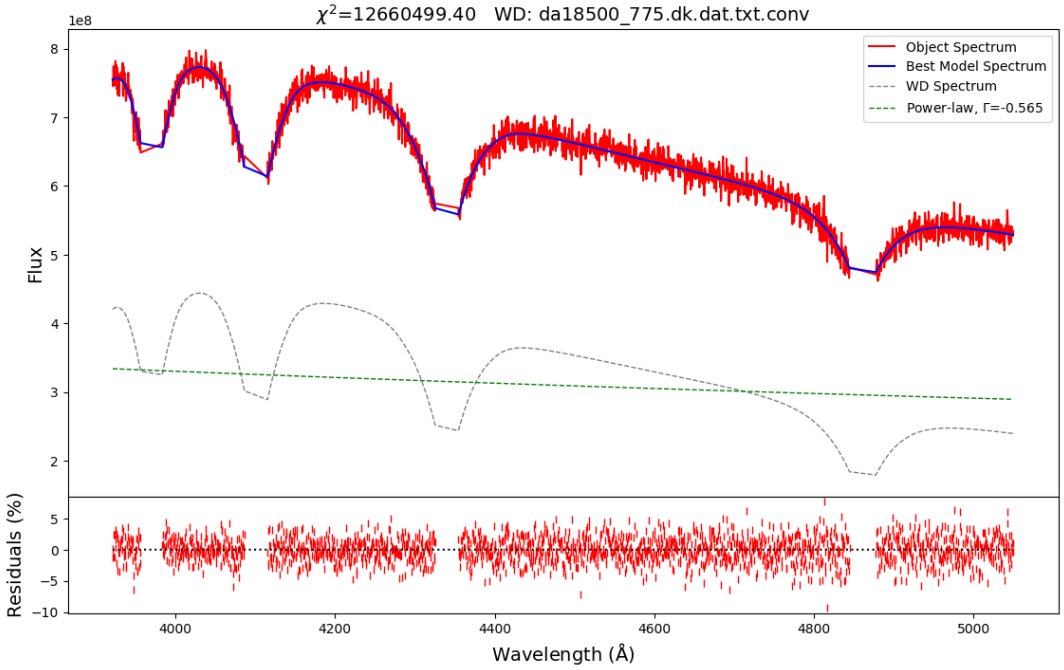

FIGURE B.29: Spectrum with S/N=50, $v = 1000\,\mathrm{km/s}$ and power-law flux contribution of 1000%.

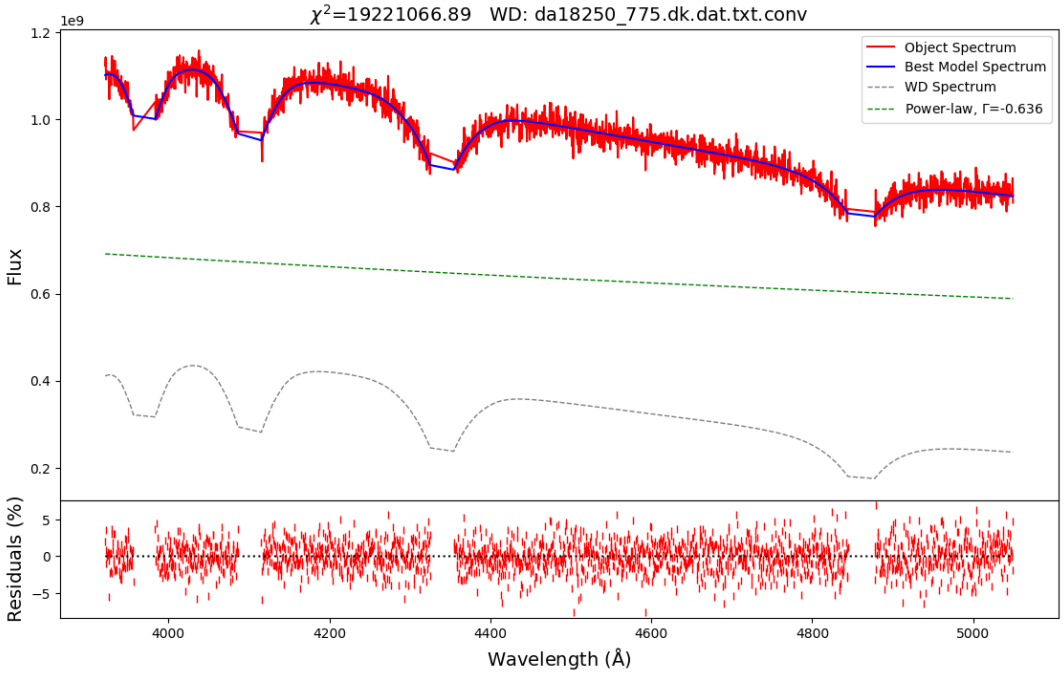

FIGURE B.30: Spectrum with S/N=50, $v = 1000\,\mathrm{km/s}$ and power-law flux contribution of 200%.

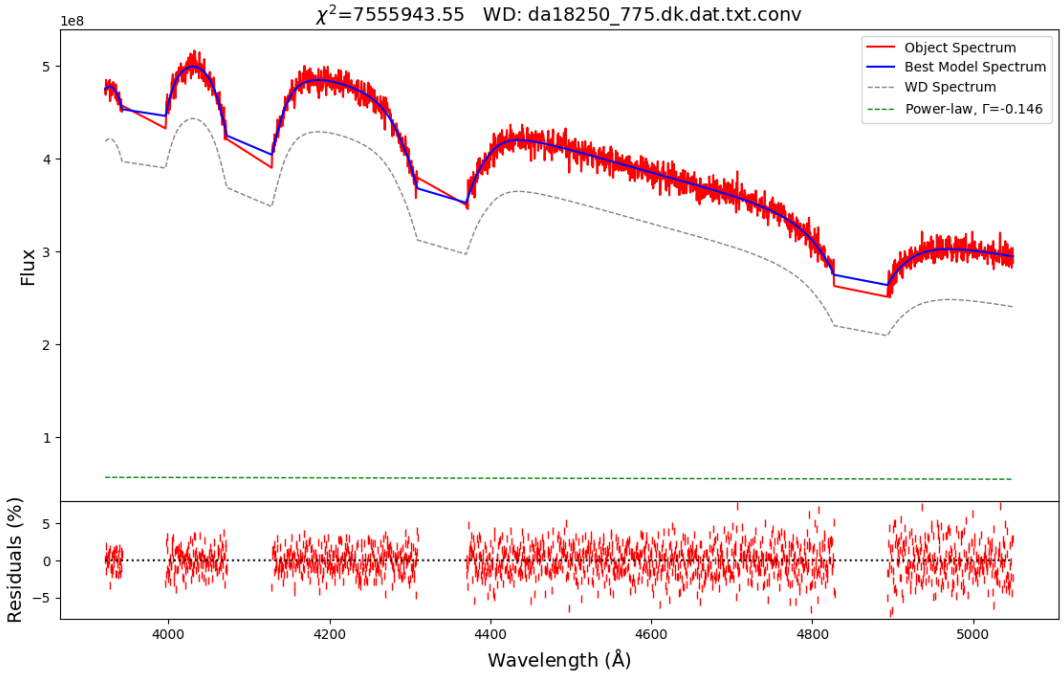

FIGURE B.31: Spectrum with S/N=50, $v = 2000\,\mathrm{km/s}$ and power-law flux contribution of 20%.

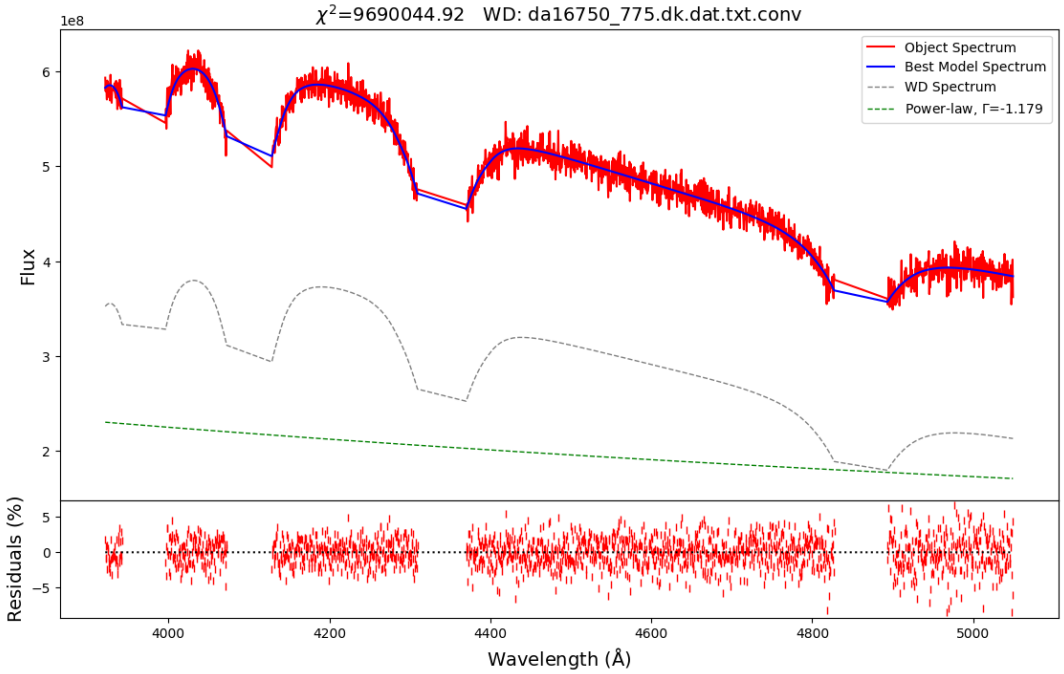

FIGURE B.32: Spectrum with S/N=50, $v = 2000\,\mathrm{km/s}$ and power-law flux contribution of 50%.

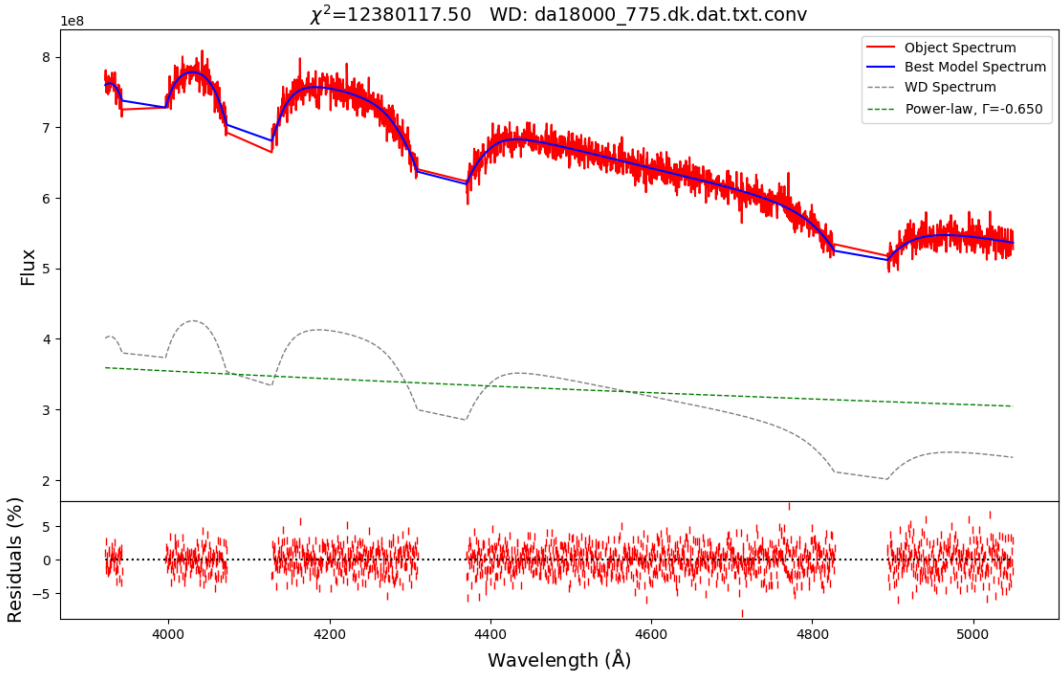

FIGURE B.33: Spectrum with S/N=50, $v = 2000\,\mathrm{km/s}$ and power-law flux contribution of 100%.

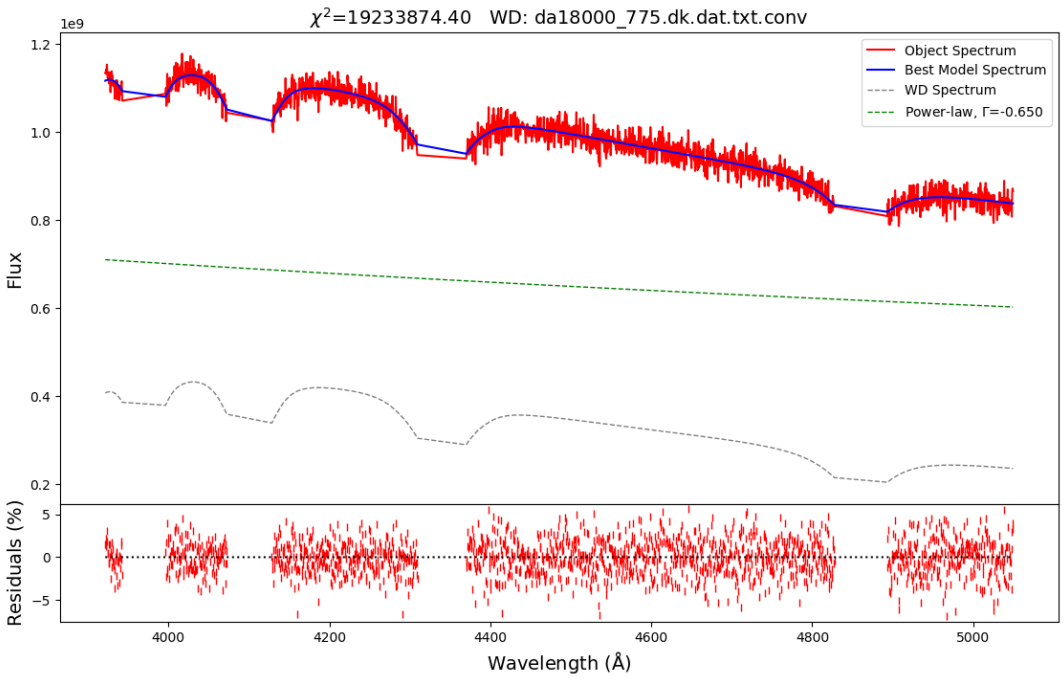

FIGURE B.34: Spectrum with S/N=50, $v = 1000\,\mathrm{km/s}$ and power-law flux contribution of 200%.

Bibliography

[1]D. Prialnik, *An Introduction to the Theory of Stellar Structure and Evolution* (2009).

[2]J. Frank, A. King, and D. J. Raine, *Accretion Power in Astrophysics: Third Edition* (2002).

[3]B. Warner, *Cataclysmic variable stars*, Cambridge Astrophysics (Cambridge University Press, 1995).

[4]J. E. Pringle and R. A. Wade, *Interacting binary stars* (1985).

[5]P. P. Eggleton, "Aproximations to the radii of Roche lobes.", **268**, 368–369 (1983).

[6]J. Patterson, "The evolution of cataclysmic and low-mass x-ray binaries", The Astrophysical Journal Supplement Series **54**, 443–493 (1984).

[7]H. C. Spruit and H. Ritter, "Stellar activity and the period gap in cataclysmic variables", **124**, 267–272 (1983).

[8]C. Knigge, "The donor stars of cataclysmic variables", Monthly Notices of the Royal Astronomical Society **373**, 484–502 (2006).

[9]C. Knigge, I. Baraffe, and J. Patterson, "The evolution of cataclysmic variables as revealed by their donor stars", The Astrophysical Journal Supplement Series **194**, 28 (2011).

[10]E. M. Sion, "Accretion physics; rotation rates; and chemical abundances of cataclysmic variable white dwarfs from HST spectroscopy", in 1997 pacific rim conference on stellar astrophysics, Vol. 138, edited by K. L. Chan, K. S. Cheng, and H. P. Singh, Astronomical Society of the Pacific Conference Series (Jan. 1998), p. 317.

[11]D. M. Townsley and L. Bildsten, "Theoretical modeling of the thermal state of accreting white dwarfs undergoing classical nova cycles", The Astrophysical Journal **600**, 390 (2004).

[12]B. T. Gänsicke, K. S. Long, M. A. Barstow, and I. Hubeny, "FUSE and HST STIS Far-Ultraviolet Observations of AM Herculis in an Extended Low State", **639**, 1039–1052 (2006).

[13]A. F. Pala, B. T. Gänsicke, D. Townsley, D. Boyd, M. J. Cook, D. De Martino, P. Godon, J. B. Haislip, A. A. Henden, I. Hubeny, K. M. Ivarsen, S. Kafka, C. Knigge, A. P. LaCluyze, K. S. Long, T. R. Marsh, B. Monard, J. P. Moore, G. Myers, P. Nelson, D. Nogami, A. Oksanen, R. Pickard, G. Poyner, D. E. Reichart, D. Rodriguez Perez, M. R. Schreiber, J. Shears, E. M. Sion, R. Stubbings, P. Szkody, and M. Zorotovic, "Effective temperatures of cataclysmic-variable white dwarfs as a probe of their evolution", **466**, 2855–2878 (2017).

[14]D. M. Townsley and B. T. Gänsicke, "Cataclysmic variable primary effective temperatures: constraints on binary angular momentum loss", The Astrophysical Journal **693**, 1007 (2009).

[15]D. F. Gray, *The observation and analysis of stellar photospheres*, 3rd ed. (Cambridge University Press, 2005).

[16]D. S. Finley, D. Koester, and G. Basri, "The temperature scale and mass distribution of hot DA white dwarfs", The Astrophysical Journal **488**, 375–396 (1997).

[17]P. Bergeron, J. Liebert, and M. S. Fulbright, "Masses of DA White Dwarfs with Gravitational Redshift Determinations", **444**, 810 (1995).

[18]B. Voß, "White dwarfs in the spy and hqs surveys : an analysis of a large set of white dwarf spectra and a search for variable zz ceti white dwarfs", in (2006).

[19]T. P. G. Wijnen, M. Zorotovic, and M. R. Schreiber, "White dwarf masses in cataclysmic variables", Astronomy Astrophysics **577**, A143 (2015).

[20]C. Moran, T. R. Marsh, and V. S. Dhillon, "A new magnetic white dwarf: pg 2329+267", Monthly Notices of the Royal Astronomical Society **299**, 218–222 (1998).

[21]A. F. Pala, B. T. Gänsicke, T. R. Marsh, E. Breedt, J. J. Hermes, J. D. Landstreet, M. R. Schreiber, D. M. Townsley, L. Wang, A. Aungwerojwit, F. .-J. Hambsch, B. Monard, G. Myers, P. Nelson, R. Pickard, G. Poyner, D. E. Reichart, R. Stubbings, P. Godon, P. Szkody, D. De Martino, V. S. Dhillon, C. Knigge, and S. G. Parsons, "Evidence for mass accretion driven by spiral shocks onto the white dwarf in SDSS J123813.73-033933.0", **483**, 1080–1103 (2019).

[22]R. Ishioka, T. Kato, M. Uemura, H. Iwamatsu, K. Matsumoto, R. Stubbings, R. Mennickent, G. Billings, S. Kiyota, G. Masi, J. Pietz, R. Novak, B. Martin, A. Oksanen, M. Moilanen, K. Torii, K. Kimugasa, and H. Kawakita, "The 2000-2001 superoutburst of the wz sge-type star rz leonis: a clue to understanding the origin of viscosity in quiescent dwarf nova disks", Publications of the Astronomical Society of Japan **53**, 905–913 (2001).